INVESTIGATION OF THE MECHANICAL BEHAVIOR OF FREESTANDING

POLYCRYSTALLINE GOLD FILMS DEPOSITED BY EVAPORATION

AND SPUTTERING METHODS

Except where reference is made to the work of others, the work described in this dissertation is my own or was done in collaboration with my advisory committee. This dissertation does not include proprietary or classified information.

_____
Liwei Wang

Certificate of Approval:

_____   _____
Bryan A. Chin   Barton C. Prorok, Chair
Professor   Assistant Professor
Materials Engineering   Materials Engineering

_____   _____
Zhongyang Cheng   Dong-Joo Kim
Assistant Professor   Assistant Professor
Materials Engineering   Materials Engineering

_____   _____
Jeffrey Suhling   Joe F. Pittman
Professor   Interim Dean
Mechanical Engineering   Graduate School

INVESTIGATION OF THE MECHANICAL BEHAVIOR OF FREESTANDING

POLYCRYSTALLINE GOLD FILMS DEPOSITED BY EVAPORATION

AND SPUTTERING METHODS

Liwei Wang

A Dissertation

Submitted to

the Graduate Faculty of

Auburn University

in Partial Fulfillment of the

Requirements for the

Degree of

Doctor of Philosophy

Auburn, Alabama
August 04, 2007

INVESTIGATION OF THE MECHANICAL BEHAVIOR OF FREESTANDING

POLYCRYSTALLINE GOLD FILMS DEPOSITED BY EVAPORATION

AND SPUTTERING METHODS

Liwei Wang

_____
Signature of Author

_____
Date of Graduation

VITA

Liwei Wang, daughter of Xianjin Wang and Yurong Bao, was born on March 4, 1980, in the city of Tianjin, P.R. China. She entered East China University of Science and Technology in August 1997 and graduated with a Bachelor degree in Materials Science and Engineering in June 2001. She joined the graduate program in Materials Engineering at Auburn University in August 2001 to pursue her Ph.D. degree.

DISSERTATION ABSTRACT

INVESTIGATION OF THE MECHANICAL BEHAVIOR OF FREESTANDING

POLYCRYSTALLINE GOLD FILMS DEPOSITED BY EVAPORATION

AND SPUTTERING METHODS

Liwei Wang

Doctor of Philosophy, August 4, 2007
(B.S., East China University of Science and Technology, 2001)

195 Typed Pages

Directed by Barton C. Prorok

The Membrane Deflection Experiment was employed to perform the micro-tensile testing on freestanding polycrystalline gold thin films. Films with varying thickness of 0.25 μm, 0.50 μm and 1.00 μm were deposited on Si substrates by both EBeam evaporation and sputtering techniques. High-resolution scanning electron microscope, including electron-backscattered diffraction, was employed to provide a morphology and crystallographic analysis. The Young's modulus of gold deposited by EBeam evaporation was measured consistently in the range of 53-62 GPa while 68-72 GPa was measured for the sputtered films. An analysis of film texture is employed to explain this difference. Plastic yielding of the evaporated and sputtered films was

compared due to the varying microstructure of each deposition technique. The differences in their microstructures appear to assert a measure of control on the deformation mechanics.

Low applied strain rates have been one of the least studied conditions and considering that engineered components are often subjected to them, garnering a more fundamental understanding of their influence on deformation of nanostructured metals is important to their design. This work studied the strain rate dependence of freestanding, gold films systematically by the membrane deflection experiment technique with applied strain rates on the order of 10^{-4} s^{-1} to 10^{-6} s^{-1}. The plastic properties were found to be particularly sensitive to strain rate, as well as film thickness and grain size, while the elastic property remained relatively unchanged. The thinner films exhibited significant strain rate sensitivity while the thicker films exhibited only marginal changes. Hall-Petch boundary hardening was observed and dominated plastic flow at larger strain rates while diffusion controlled deformation mechanisms appeared to be activated with increasing influence as strain rate decreased. Analysis of dislocation-based and grain boundary diffusion related creep suggested that the films were likely experiencing a mixture of grain boundary diffusion and sliding as the dominant deformation mechanisms at lower strain rates. Furthermore, the data from the evaporated nanocrystalline films suggested that the critical grain size for inverse Hall-Petch behavior was sensitive to strain rate. These results represent an important experimental confirmation of how nanostructured materials behave at very low strain rates.

ACKNOWLEDGEMENTS

Style manual or journal used: <u>IEEE</u>

Computer software used: <u>Microsoft Word, Excel, PowerPoint, KaleidaGrap</u>

TABLE OF CONTENTS

LIST OF FIGURES

xv

LIST OF TABLES

CHAPTER 1

INTRODUCTION

1.1 Thin Film Applications

For decades, the persistent interest for thin film materials and technologies has continued to grow at an ever increasing pace as the number of applications for micro and nanoscale increases, including the progressive trend towards the further miniaturization of those device systems in the field of microelectronics, optics, magnetic, and micro electromechanical system (MEMS) etc [1-3].

Thin films are structures with geometry such that the dimension in one direction is orders of magnitude smaller than in the others. The thickness of thin films ranges from a few nanometers to a few micrometers, above this thickness, structures are usually referred to as thick films or possibly foils, and most of them exhibit many of the characteristics belongs to bulk materials. Depending on the application, thin films can be made of a variety of different materials: polymers, semiconductors, ceramics, glasses or metals etc. However, of all of these, thin films of metal are the most commonly found and practically used in modern society and industry today.

The most prevalent application for thin films is being the building blocks in the construction of microfabricated structures. From the integrated circuit composed microprocessors to the micro system referred as the Microelectromechanical system (MEMS). Many essential components of these microfabricated structures are thin films

ranging in thickness from a few nanometers to a few micrometers. Microfabrication processes involve many steps in which thin films of various materials are deposited on the surface of a substrate. Deposition methods including evaporation, chemical vapor deposition and sputtering are used to place layers of metals, silicon, polysilicon, dielectrics such as silicon dioxide and silicon nitride on top of one another. The patterning and transfer is done by means of photolithography and etching. Wet chemical etching and dry plasma etching are employed to remove materials from the deposited films or the structures.

Compared to the first success of Integrated circuit (IC) fabricated in the early 1960s with only several transistors and resistors on a few square millimeters of silicon die, over 100 million transistors on a few square centimeters of silicon die can be achieved nowadays. The manufacturing techniques of microelectronic devices have grown so rapidly that make the practical application spread out so widely to change our modern society dramatically. Microelectronic devices are made more powerful primarily by reducing the size of their features in accordance with Moore's law: the number of transistors that can be fabricated on a silicon integrated circuit, therefore the computing speed of such a circuit is doubling every 18 to 24 months.

With the increased sophistication and success in the semiconductor manufacturing industry, a new exciting area was raised during the past 10 years: the manufacturing of micro system which in particular, referred as Microelectromechanical systems (MEMS) or Nanoelectromechanical system (NEMS) [4]. The MEMS device is defined as a tiny structure with a size on the order of microns and is the integration of mechanical elements, sensors, actuators, and electronics on a common substrate through

microfabrication technology. They are mainly batch-fabricated by the similar processing technique used for microelectronic production and can be arranged in arrays inside a suitable package.

Many types of existing MEMS have been interacted with our daily life. The area of the applied MEMS reached extensively from the medical equipment to the automotive parts. For example, a modern micro-sensor for airbag compares the detected acceleration history with pre-programmed acceleration data corresponding to a real car crash, to avoid unnecessary deployments; Microfabricated flow sensors can measure a stream or even count infected cells in a solution. In the fields of Medicine and Chemistry, micro-valves and micro-pumps are used to mix fluids, separate solutions (micro-fluidic chemical separation systems), create flows and deliver drugs inside our body when needed [5].

The significance of the thin film application in this exciting area leads to the promising achievements which are built on the constant process experience of trial and error. Material and structural properties information are the roots for practical designs. As macro scale structures, these small devices are often subjected to complex stress-states during application, and the mechanical demands placed on each individual layer of thin films employed in these devices can lead to various failures which are attributed to the plastic deformation, fracture, stress-induced cracking, etc., which can have a significant effect on the overall performance [6]. Therefore, it is desirable to be able to predict the mechanical response of these small bodies to loading in order to design and fabricate reliable devices. However, compared to the enormous amount of experimental and theoretical work have been done regarding to the macroscopic reaction of material over large length scales, the study for the microscale structures is far from comprehensive.

Nonetheless, experimental evidence suggests that the mechanical behavior of these small structures differ form the behavior observed in their bulk form to a great extent [1, 7].

1.2 Thin Film Mechanics

It has been well known for quite some time that classical continuum mechanics theories fail to describe the mechanical behavior for sample dimensions are of a few microns or submicron under elastic and plastic loading conditions. Therefore, higher-order micro mechanics concepts are required to obtain an appropriate prediction of the mechanical behavior of miniaturized structures.

1.2.1 Overview

The diverse mechanical response of thin films are attributed to many intrinsic factors: as thin film dimensions begin to approach the scale of the material microstructure features, for example, thin films may have only one or several grains through the thickness, the film properties or behavior begin to exhibit a dependence on the thickness [7]. Furthermore, because of the film thickness does not exceed some small multiple of the characteristic atomic or molecular spacing, the surface or external interface effects become very important, and therefore the averaging concept in all directions may break down. Moreover, oxide layers on the surface of thin metal films may act as barriers to the plastic deformation experienced by the material. For most polycrystalline metal thin films, the outcome of this effect translates to a so called size strengthening phenomena or size effect alternatively [1, 8]. In this section a brief introduction on the dependence of the mechanical material behavior on the sample size is given including an overview of the literature related to this field.

4

In Figure 1-1, an overview of material length scales from the atomic level up to macro scale is given. A broad classification of applications and theories about how to describe their mechanical behavior is shown as a function of size. On the left are four categories of structures and the regime where their dimensional size fits on the length scale. On the right are the theories used to predict their mechanical behavior and the length scale where they are applicable. The fact that elastic properties are dependent substantially on the bonding nature of the material makes it seems intuitive that there is no size effect on elastic properties of metals unless the dimensions of the structure are at the atomic scale. Therefore, only plasticity theories are listed in Figure 1-1.
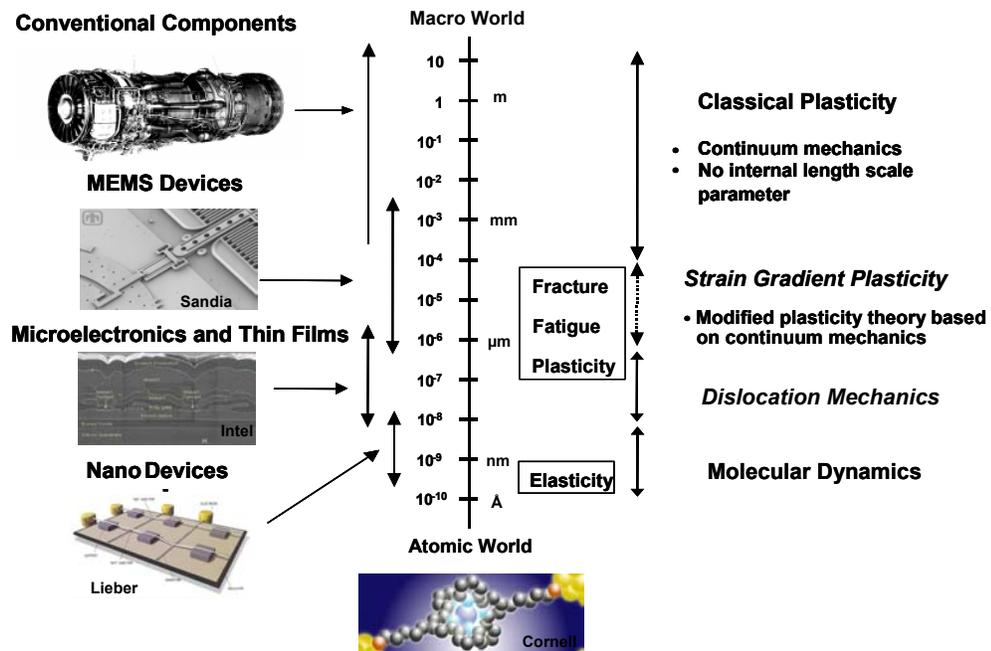
Figure 1-1 Illustration of Length-scale effects on the mechanical properties of materials [9].

The classical continuum plasticity can successfully describe and predict the materials mechanical behavior with structure dimensions greater than 100 μm. On the

5

other end, the molecular dynamics (MD) is only applicable to the systems with dimensions less than 100 nm in size due to the current limited computation power since this method is based on the large scale numerical simulation. And the intermediate gap left between the continuum mechanics and quantum mechanics is generally considered to be bridged by micromechanics, where thin film mechanics falls into. The past decade has been marked by a substantial progress in the proper understanding and modeling of the mechanics of materials at small length scales based on the enormous amount of work that has been done worldwide.

1.2.2 Size Effect Phenomena

Several pioneering studies have experimentally identified the existence of size effects on the plasticity of polycrystalline metals. One of them is micro-torsion test, reported by Fleck et al. on the strengthening effect resulted from decreasing the diameter of the tested thin copper wires [10]. As shown in Figure 1-2, in this test, a torque was applied on the copper wires with varying diameters in the range of 12 - 170 μm. And an increase in strength by a factor of two or three for the smallest wire over the largest was observed. Direct tensile tests were also performed on the same copper wires and there was no size effect was observed. This was explained by an increase in the density of geometrically necessary dislocations in torsion; as in torsion there exists a macroscopic strain gradient responsible for the storage of geometrically necessary dislocations in contrast to tension.

6
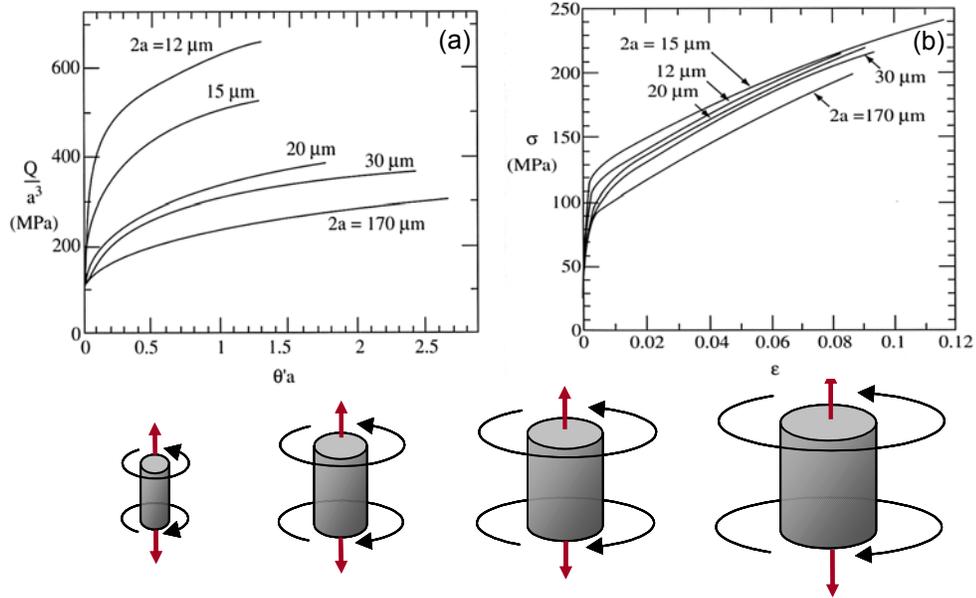
Figure 1-2 Plots of (a) applied torque vs. twist for copper rods of varying diameter and (b) stress-strain of identical rods subject to direct tension [10].
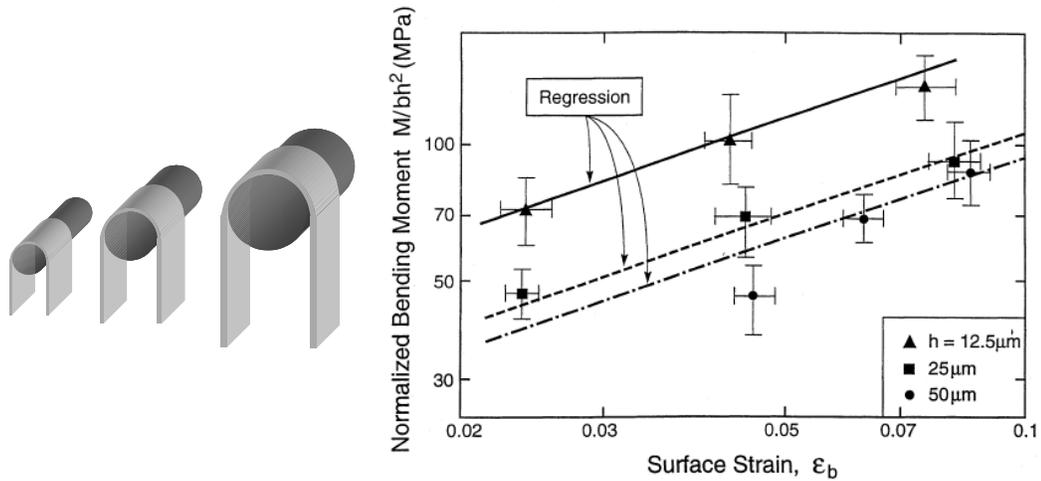
Figure 1-3 Plot of normalized bending moment vs. surface strain illustrating how the thinner films require more bending moment for the same state of strain [11].

Similar micro-bending tests were performed by Stolken and Evans [11]. The thin nickel foils of different thicknesses varying from 12, 25, and 50 μm were bent around rigid rods whose diameters scaled with each film thickness respectively to ensure

7

identical states of strain developed in each strip, as seen in Figure 1-3. The result shows that thinner foils required a larger equivalent moment for producing a certain amount of surface strain.

Moreover, various micro- and nano-indentation tests have been done and confirmed the existence of a strong size effect by usually showing the material hardness decreases as indentation depth increases by a factor of two to three [12-14]. Figure 1-4 shows the plot of hardness vs. plastic depth illustrating how hardness increases with smaller plastic depth. In addition, an increase of the yield strength with decreasing the penetration depth in copper films was also found by Hommel and Kraft [15] and others [16]. These findings were explained by hardening due to the strain gradient in the vicinity of the indenter tip. It must be stressed that due to the complexity of the stress field in indentation, size effect studies using this technique are difficult to interpret.
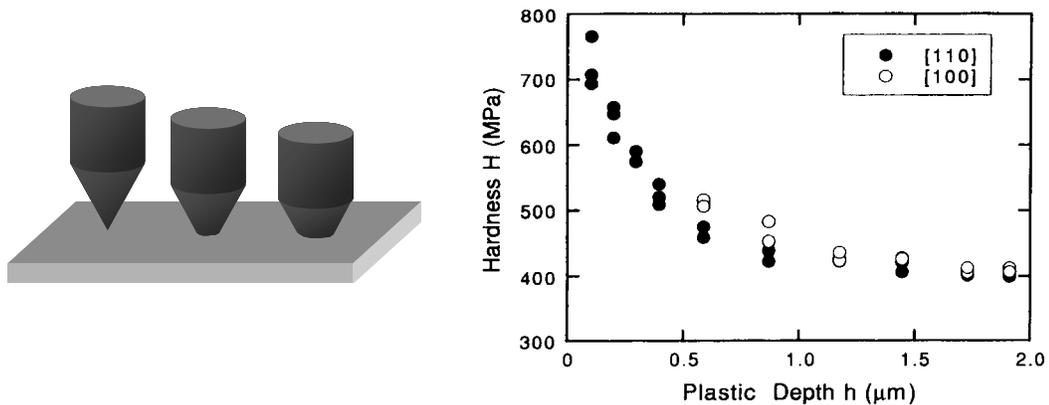
Figure 1-4 Plot of hardness vs. plastic depth illustrating how hardness increases with smaller plastic depth [13].

Besides the size effect observed in plastic properties like hardness and yield strength, size effects in failure properties were also found by a number of studies.

Hommel [17] and Keller [18] reported a size effect in the fracture strength for FCC metals such as copper. Similarly, a decrease of fracture toughness with increasing thickness was found by Irwin [19] in tensile testing of sheets. Also in tensile testing, a decrease in the strain at fracture with decreasing thickness was found for thin copper foils by Hadrbolets [20] and Klein [21], alike findings for thin gold and aluminum films by Espinosa [22].

Different kinds of size effects are reported in the literature. The mechanical properties, whereas for standard crystalline materials there are no substantial indications for size effects of the elastic properties, plastic and failure properties seem to be size dependent to a certain extent whether in simple tension, torsion, bending, or indentation testing. All of these experiments have generally shown the trend that a smaller structure has higher strength and lower ductility than a larger one.

1.2.3 Developments in Size Effect Mechanisms

Size effect has been recognized as the most intrinsic characteristic for thin film mechanical behaviors. Therefore, to achieve a better understanding for the thin film mechanics, a plausible explanation for size effect has to be clarified.

From the pioneering experimental studies, the mechanical properties size dependence phenomenon was considered generally to be a result of nonuniform straining. The deformation process in metals enhances the dislocation formation, the dislocation motion, and the dislocation storage. The storage of dislocation is the root cause for material hardening. Generally, two types of dislocations are involved in the case of nonuniform straining: the dislocations generated by trapping each other in randomly are referred as statistically stored dislocations; while some extra dislocations accumulate in

addition to statistically stored dislocations to accommodate the strain gradient are named as geometrically necessary dislocations. Statistically stored dislocations are believed to be dependent on the effective plastic strain, while the density of geometrically necessary dislocations is proportional to the gradient of the effective plastic strain [23-26]. During the last 10 years, many scientists have argued that the size dependence of the material mechanical properties is a consequence of an increased intensity of strain gradients inherent in small localized zones which lead to geometrically necessary dislocations that are responsible for the additional strengthening [26-29]. Therefore, several gradient induced strengthening theories have been proposed based upon the experimental size effect studies mentioned above, in an effort to explain and predict the size dependence behavior of materials at the micron and submicron regime. And it has to be addressed that the key for the validity of these strain gradient theories is relied on the proper incorporation of an intrinsic material length parameter into the theory modeling [14, 30, 31]. However, the difficulties of determining the intrinsic material length precisely from both experiments and analytics limited the fully utility and understanding of the plasticity gradient strengthening mechanisms. Therefore, other possible explanations are needed to be explored.

In the aforementioned work performed by Fleck, beside the micro-torsion tests, direct micro-tensile tests were also carried out on the same copper wires. The author concluded that there was no size effects presented in the tension test result [10]. However, it should be noticed that the smallest rod diameter investigated in this study was 12 μm. The homogeneous manner in which the uniaxial tests were conducted seemed to have hindered strain gradients in plasticity from occurring. Then the question

comes to that whether size effect can exist in the absence of strain gradients or not. Recent work on tensile testing of thin gold films of submicron thickness has shown that size effects do indeed exist without the presence of strain gradients. In these studies, grain size was held constant at approximately 250 nm while specimen thickness and width were varied systematically. Experimental results show that the yield strength more than doubled when film thickness was decreased, with the thinner specimens, a brittle-like failure exhibited and a strain softening behavior for the thicker ones [32, 33]. It is believed that these size effects stem from the limited number of grains through the thickness, which limits the number of dislocation sources and active slip systems; hence, other deformation modes such as grain rotation and grain boundary shearing accompanied by diffusion seemed to become dominant.

Several theoretical models have been proposed to explain these kinds of effects but still there is no common agreement on the "right" one. This disagreement can be explained to a certain extent through the fact that most size effect studies did not include a thorough and systematic characterization of the microstructure of the materials tested. Therefore, it is not always clear whether a certain effect is due to the microstructure, the size of a structure or the interaction of both factors. In order to interpret the occurrence of size effects from a more clarifying perspective, it is important to categorize the known size effects based on their engineering practice, experimental analysis and connection to the intrinsic microstructures. A rough classification adapted from the one proposed by Geers [34] is given as follows

Microstructural size effects This category is also known as 'intrinsic' size effects, reflecting the intrinsic role of the dimensions of phases and particles in the microstructure

of a heterogeneous or multi-phase metal [35]. Microstructural size effects originate from the elementary physical processes producing deformation on the sub-micro and nano-scale level and are the result of interacting unit deformation processes in all phases, in which many microstructural length scales play an important role (Burgers vector length, grain size, obstacle size, obstacle spacing, grain boundary width, etc.). Their effects may both lead to strengthening (e.g. Hall-Petch effect) [36, 37] or weakening (e.g. inverse Hall-Petch effect) [8, 38].

Strain gradients induced size effect As discussed earlier, size effect that responsible for the strengthening of many metals at small length scales was considered generally a consequence of an increased intensity of strain gradients inherent in small localized zones [10, 11, 13, 14]. The increase of the gradient can be naturally resulted from scaling down of a component to a much smaller scale while keeping all geometrical proportions identical. This category of size effects is commonly called 'gradient effects'. The only physical manner to accommodate these gradients is by the introduction of extra dislocations in the lattice, commonly denoted as geometrically necessary dislocations which contribute to the additional hardening as a pronounced effect on the mechanical response.

Dimensional constraints induced size effects This special category of size effects are originated from the interaction of the plastic slip carriers with either the external boundary or interfaces between layers of different materials [39, 40]. For small dimension structures, the number of grains in one of the spatial directions may become very small, which triggered the orientation dependence and additionally grain boundary dependence problem. In the case of thin films or multi-layered structures, all material is

relatively close to a physical boundary or interface. Plastic slip is carried by dislocations which can either be blocked at the boundary or glide out of it depending on the physical properties of the external boundary or interface. Hard coatings or oxide barrier layers are typical examples that may obstruct plastic slip up to a certain level: the influence of the boundary layer generally covers a certain volume, which explains the importance of the surface-to-volume ratio as found in experimental analyses [41]. Surface or interfacial constraints may induce strengthening or weakening depending on the physical boundary conditions and the deformation mechanisms involved. Hard boundary layers generally lead to strengthening while unconstrained or free boundaries generally contribute in the opposite sense. Furthermore, this category of size effects seem very practically important from the engineering perspective since the external boundary conditions and material interfaces can be influenced during or after the processing of the material.

At this point, an extensive amount of theoretical and experimental work has been done trying to understand the size dependency behavior of materials; nonetheless, this research area is still in its critical state with numerous controversies. Future investigations are more than necessary to address the insight of the fundamental deformation mechanisms about materials at this scale.

1.3 Thin Film Mechanical Testing

The greatest challenge in investigating thin film mechanics is to perform mechanical tests on such a small scale with the specimens' physical dimensions ranging from a few hundred of micrometers down to a few hundred of nanometers. The difficulties stemmed from the sample fabrication, sample handling during the test and

complexity of data interpretation procedure have called for novel mechanical testing methods to be developed. The thin film mechanical testing techniques can be generally classified as two groups based on the film configuration: methods for thin film attached to a substrate or methods for free-standing thin films.

1.3.1 Testing Methods for Films on Substrate

The advantages of studying a film/substrate system include the fact that it is the most common type of system found in microelectronics; the easiness of preparation and handling of the thin film specimens. The testing methods described below have facilitated the production of much useful data on a large variety of thin film materials.

Nanoindentation Method

The most commonly and widely used experimental method for studying a film/substrate system is the depth sensing indentation method, more known as the nanoindentation method for estimating the mechanical properties of materials [42-44]. As illustrated in Figure 1-5, it employs high-resolution instrumentation to continuously control and monitor the loads and displacements of an indenter as it is driven into and withdrawn from a material. The result is a load-displacement signature with loading and unloading segments that describe material response. Hardness and elastic modulus are the properties most frequently measured by this technique, other mechanical properties such as fracture toughness and internal friction may also be evaluated from the same depth sensing indentation data with the incorporation of other tools [45, 46]. However, the fact that nanoindentation imposes complex, non-uniform deformations to the specimen makes the interpretation of the experimental results difficult, and also the large inhomogeneous

strain induced by the sharp indenters make the test is not sensitive enough identify the subtle differences in mechanical properties [47-51].
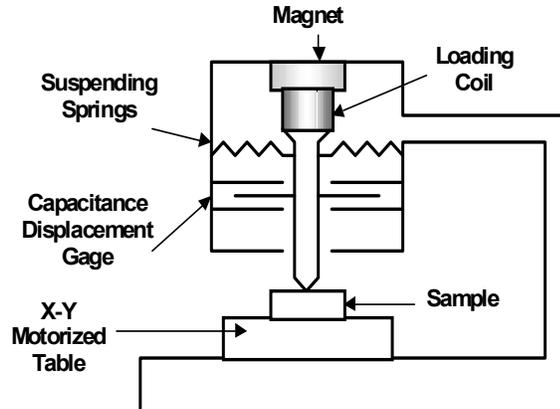
Figure 1-5 Schematic view of the Nanoindenter XP instrumentation [14].

Substrate curvature method

Another commonly employed method is the substrate curvature method, also called the wafer curvature test, as shown in Figure 1-6. The principle of this method is based on the difference between the thermal expansion coefficient of the film and substrate, which will induce a stress when a temperature variation is given to the system. The strain caused by this stress can only be accommodated by introducing a curvature into the structure system. Whether this curvature is convex or concave is determined by which material has the greater thermal expansion coefficient and therefore interpreted as whether the film has tensile or compressive residual stress. This technique determines film properties by taking advantage of the fact that stress in the film are proportional to the radius of curvature of the substrate [52]. Elastic and plastic properties can also be examined by varying the temperature. However, there are some complexities rooted in the nature of this test method, such as the nonuniformity of substrate-material adhesion

15

and temperature; the interaction and confusion between the other possible temperature dependent processes with plasticity, hindered the accurate property measurement [53].
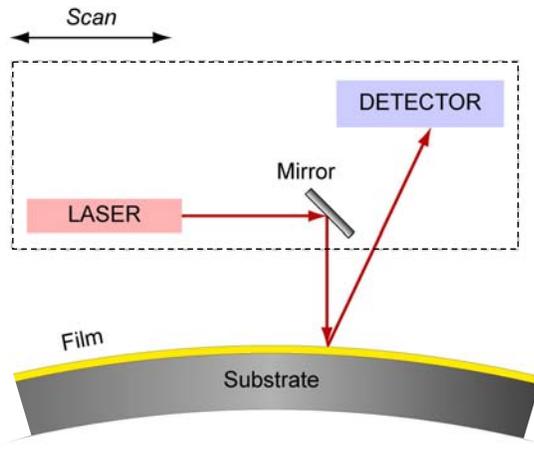
Figure 1-6 Schematic view of substrate curvature testing.

The most challenging problem encountered by both of the above methods is the difficulty to decouple the behavior of the film itself from the effects of the presence of the substrate. Numerous theories have arisen over the years explain the behavior of this kind of films, many of which focus on the interaction of the film with its substrate [28, 47, 48, 50, 54-56]. These theories provide valuable insight into the mechanics of the thin films themselves. However, there is still no straightforward way to determine how thin films would behave without the substrate by these methods. Another limitation shared by both of the above methods is the incapability to portray the material stress-strain behavior from their experiment data, which in a way is the incapability to provide any yield and post yield properties.

Microbeam Deflection Method

An alternative to the substrate curvature and nanoindentation method for mechanical testing a film substrate system is the microbeam deflection method which

was first performed by Weihs [57] and later repeated and improved by others [58-63]. Basically, this method involves deflecting a cantilever-like beam with one end attached to the substrate. The beam is a bi-layered structure, usually composed of the tested film and silicon substrate. Producing such structures is achieved with standard microfabrication procedures. Dimensions are on the order of a few micrometers to submicrometer thickness, tens of micrometers wide and hundreds of micrometers in length. Structures of this size have an extremely low stiffness and therefore high-resolution load cells are required to perceive the response of the beam. Nanoindenters have been shown to provide such load resolution and are routinely used in this method. A schematic of a typical microcantilever structure being deflected by a nanoindenter is shown in Figure 1-7. By this method, the measured force-displacement curve can be used, in conjunction with elementary beam theory to proved estimates of the elastic and plastic properties. However, the technique exhibits some unique features. For example, the analytical solution is very sensitive to the measure thickness where its influence is to the third power warranting that extra care must be taken to accurately measure the specimen thickness. Undercutting during the release step introduces uncertainties in the measurement of the cantilever length. The technique also confronts with boundary bending effects and inhomogeneous distribution of the strain since the bending moment is not constant along the length of the beam. Recently, Florando [63] has proposed a solution to this issue by using a triangular beam, which was acclaimed to have the advantage that the entire film on the top surface of the beam is subjected to a uniform state of plane strain as the beam is deflected, unlike the standard rectangular geometry

17

where the bending is concentrated at the support [63]. Stress-strain behavior for the material can then be more accurately obtained.
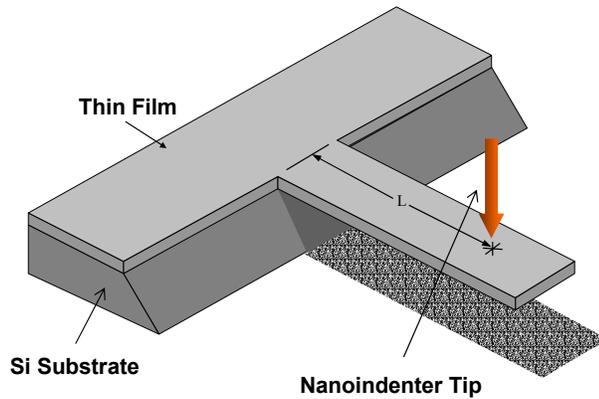
Figure 1-7 Schematic three-dimensional (3D) view of a freestanding microcantilever structure deflected by a nanoindenter tip.

1.3.2 Testing Methods for Free Standing Films

In an effort to make some fundamental statements about the mechanical behavior intrinsic to the material itself, the most obvious option leads to the examination of free-standing thin films. Although a free standing structure is a less frequently encountered case in practical applications currently, it provides the intrinsic properties on mechanical behavior. Various methods have been developed to investigate the mechanical properties on such films and a few of the most popular ones will be addressed here.

Bulge Test

One of the methods for freestanding film test is called bulge test, developed by Beams in 1959 [64], and further improved by others [65, 66]. This method is designed to determine the in-plane mechanical properties of the film by eliminating specimen edge effects as well as avoiding the complexities from substrate material. In the bulge test, a freestanding film is deflected by applying pressure with compressed gas or liquid. The

suspended film is fixed onto a supporting substrate, by imposing a pressure on one side of the film, the film is forced to bow out. The resulting "bulge" height can then be measured by interferometry or other techniques. The apparatus required to perform the bulge test is simple and the method is an easy way to examine both elastic and plastic properties. However, sample preparation is restricted to thin films with tensile residual stresses. Films with compressive residual stresses can buckle, which might cause the underestimation of material properties [67, 68].
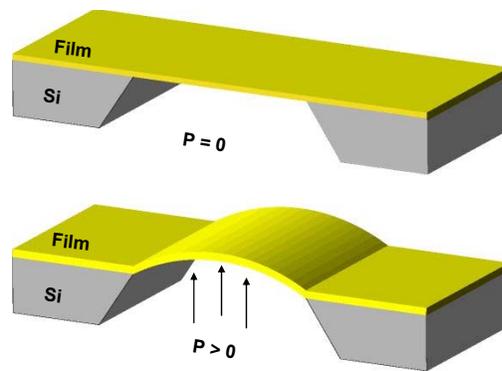
Figure 1-8 Schematic three-dimensional (3D) view of a freestanding film structure deflected by an applied pressure in bulge test.

Microtensile Testing

Most of the mechanical properties we learned for bulk materials were obtained by performing tensile tests. Thus, the equivalent of a tensile test, customarily to tone with the samples in a much smaller scale, is desirable. All of the aforementioned techniques have provided useful data for the mechanical properties of thin films. However, tensile testing does possess several advantages over the other methods. These are: a) comparison of results to those for bulk materials is straight forward; b) deformation and stress state are uniform; c) internal stresses in the films due to processing can be eliminated before testing.

19

Several innovative microtensile testing methods have been developed and proposed to study the stress–strain response of free-standing films [69-76], and a few of which will be introduced briefly here. One is developed by Sharpe et al [77]. In this test, the specimen was prepared in a unique fashion such that the tested film was framed onto a micromachined window. The finished tensile specimen is then mounted in the testing rig and grips are attached at either end. The two narrow sides are then cut to free the specimen from the frame support to some extent. A piezoelectric actuator is employed to displace the specimen and subject it to uniaxial tension. Load is measured with a load cell possessing a resolution of 0.001 g, and strain was quantified with an interferometric strain displacement gauge. The typical width of a specimen is 600 μm and the gauge length is 400 mm. two sets of orthogonal strips are patterned on the surface of the specimen to reflect the laser beam used in the interferometric strain displacement gauge setup.

Another innovative microscale tensile test was designed by Tsuchiya et al [78, 79]. Schematic of the test architecture is shown in Figure 1-9. The specimen is designed as a freestanding thin film with one end attached to the substrate and another large pad end gripped by an electrostatic force. This attractive force is rather large compared to the required tensile force applied to the grip; therefore, the two remain rigidly fixed together as long as the voltage is applied. Tensile testing is then achieved through loading by the piezoelectric actuation of the probe along the axis of the specimen while displacements measured by a strain gauge at the probe. The gauged region of the test specimen dimensions are on the order of: length 30-300 μm; width 2-5 μm; and thickness 0.1-2.0 μm [79].
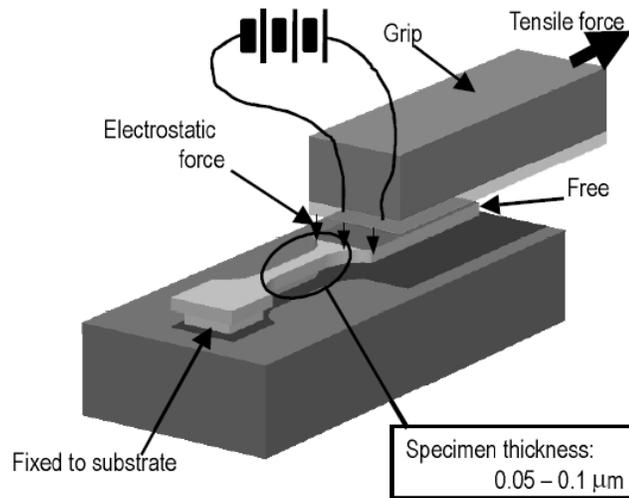
Figure 1-9 Schematics showing the architecture of the electrostatic grip system [78].

Microbridge Deflection Method

Although the most direct way to obtain mechanical properties of thin films is by uniaxial tensile testing of freestanding films, the fragility of thin films because of their size and configuration makes the uniaxial tensile testing a very difficult task. As we can noticed from the above mentioned microtensile testing methods, the tensile load is always applied on the grip part, which was attached to the film in some way, instead of on the film directly. Therefore, even the stress-strain relation of thin films in tension can be obtained; the accuracy of the result might be degraded to some extent due to the complex boundary state involved with the interaction between film, grip and load cell. On the other hand, in the microbridge deflection method, the load is designed to be applied directly onto the film in a vertical fashion. The result is direct tension, with negligible amount of bending and absent of strain gradient. Basically, but not strictly, microbridge deflection method can be accounted as a special group of microtensile testing.

21

The microbridge testing was first proposed by Tong-Yi Zhang [80]. In this test, the specimen was micromachined and suspended on a silicon window. And again the load is applied on the frame instead of on the film directly. The structure of the specimen is shown in Figure 1-10. The microbridge samples can have a thickness less than 1.0μm, a width of about 16.0 μm and length range from 55 to 80 μm. The test was conducted by a load and displacement sensing nanoindenter system, in which the microbeam was deflected by a wedge indenter. The load was applied to the center of the suspended bridge. The schematic depiction of the microbridge test was given in Figure 1-10. The resulting load-displacement behavior of the microbeam can be used to determine both the in-plane elastic modulus and the yield strength from fitting the experimental load-deflection curve with the theoretical solution by the least square technique.
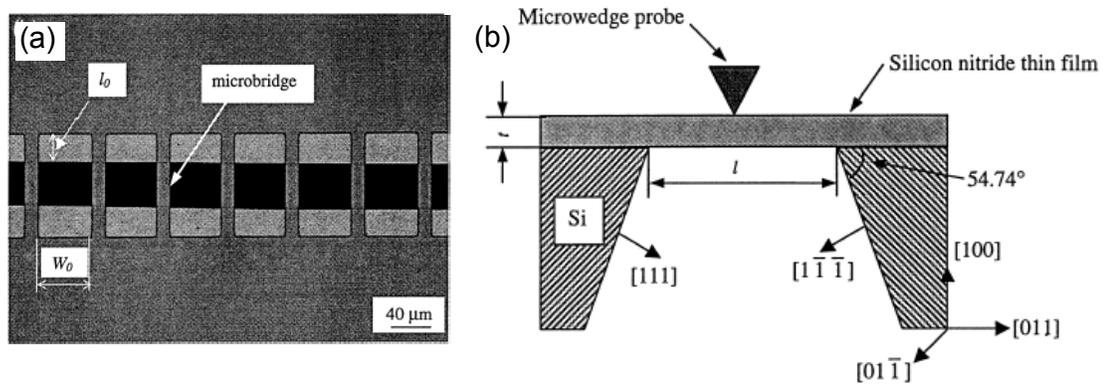
Figure 1-10 Schematics showing the architecture of the microbridge system [80].

Another microbridge deflection method was designed by Espinosa et al [81, 82], more specifically, was called as Membrane Deflection Experiment (MDE). It involves the stretching of freestanding, dog bone shaped thin-film membranes in a fixed-fixed configuration with submicrometer thickness. In this technique, a Nanoindenter applies a line-load at the center of the span to achieve deflection while an interferometer focused

on the bottom side of the membrane to record the deflection simultaneously [32, 33, 83]. There are certain advantages to this test that are worth addressing here: a) the loading procedure is straightforward and accomplished in a highly sensitive manner; b) independent measurement of stress and strain; c) the simplicity of the data interpretation procedure.

The mechanical testing method used in this study was basically adapted from the MDE. Detailed description about the methodology of this technique is given in the Experimental chapter.

1.4 Objective and Outline of This Work

From the size effect studies reviewed in section 1.2.2, most attention on size effects has been given to the pronounced strengthening found when decreasing specimen scale. Less attention was given to the intrinsic role of the microstructure in each of these experimental set-ups, whereby the precise granular structure such as grain size, grain orientations and grain boundaries were not provided and considered as an important factor. However, a comparable grain size was mostly accepted as a sufficient condition for analyzing the occurring size effect. If the number of grains gets small, clear microstructural effects will contribute and all of these effects can not be separated trivially in the experimental results. To this end, only a few studies seem to deal with this microstructural contribution, and mostly in a different context. The present work concentrates on this important aspect and tries to overcome this problem by the testing of samples of different sizes and microstructures which were systematically analyzed by means of modern material characterization methods.

The goal of this work is to develop a realistic and fundamental model that can be used to predict the mechanical behavior of most FCC metallic thin films. Much of our research has been focused on the mechanical property investigation for gold thin films. The choice of gold was made based on the following considerations: a) from the engineering perspective, gold has its extensive application in the electronics industry owing to its excellent electrical conductivity, good thermal conductivity, the excellent corrosion and oxidization resistance, the ease of fabrication, good strength and fatigue resistance; b) from the mechanics perspective, due to the significantly larger linear elastic anisotropy and low stacking fault energy gold exhibits, its plastic deformation is more sensitive to deformation twinning; c) from the practical point of view, gold was chosen because its inert nature facilitated specimen fabrication and prevented oxide formation on the test specimen.

The stacking fault energy is an important parameter in determining how a material deforms. Gold is characterized as a low energy material, which enables deformation twinning to play an increased role, in addition to crystallographic slip, in plastic deformation. The elastic modulus of gold exhibits a large degree of elastic anisotropy with modulus varying from 43 to 117 GPa [84]. Thus, depending on the film's texture the elastic deformation of gold will vary significantly. The anisotropy ratio is basically a measure of the ratio of resistance to shearing on {010} planes in <110> directions to resistance in shearing in {100} planes in <100> directions. Gold has an anisotropy ratio of 0.35. The low value for gold reflects its ability to deform by deformation twinning in addition to crystallographic slip [85].

The Membrane Deflection Experiment (MDE) technique is used to perform the microscale mechanical testing on thin films to identify the thin film mechanical behavior for gold thin films with systematically varied thickness. High-resolution SEM including electron backscattered diffraction (EBSD) is employed to provide the detailed characterizations, which assist the identification of how thin film deformation mechanisms are related to the effects of film thickness, microstructure and anisotropic elastic behavior.

The organization of this work is outlined here for the purpose of reading. Chapter 1 serves as an introduction. In Chapter 1, a brief introduction on the application and mechanics of thin film; dependence of the mechanical material behavior on the sample size is given, including an overview of the literature in this field. Chapter 2 provides much of the background theory referred to in the subsequent chapters. Next, the detailed experimental procedures are discussed in Chapter 3, which is mainly composed of sample preparation and micromechanical testing. Since this study investigated the relationship between microstructure and materials mechanical properties, microstructure characterization is very important to this study and therefore, they are carefully and extensively studied and presented in Chapter 4. Chapter 5 provides all the collected MDE data. It is then followed by the discussion and interpretation of these data presented in Chapter 6. Chapter 7 concludes all the remarks and findings of this work. This chapter will also include some possible improvements for the future studies of thin film mechanics.

1.5 References

[1]   W. D. Nix, "Mechanical-Properties of Thin-Films," *Metallurgical Transactions a-Physical Metallurgy and Materials Science*, vol. 20, pp. 2217-2245, 1989.

[2]   S. Stadler and P. K. Ajmera, "Stress control in thin sputtered films towards potential application in micromachined structures," *Materials Letters*, vol. 35, pp. 18, 1998.

[3]   I. Chasiotis, "Mechanics of thin films and microdevices," *Interface Reliability II; IEEE Transactions on Device and Materials Reliability*, vol. 4, pp. 176-188, 2004.

[4]   E. J. Garcia and J. J. Sniegowski, "Surface micromachined microengine," *Sensors and Actuators A: Physical*, vol. 48, pp. 203, 1995.

[5]   M. Gad-el-Hak, "The MEMS Handbook," 2 ed: CRC, 2005.

[6]   S. M. Spearing, "Materials issues in microelectromechanical systems (MEMS)," *Acta Materialia*, vol. 48, pp. 179, 2000.

[7]   C. A. Neugebauer, J. B. Newkirk, and D. A. Vermilyea, "Structure and Properties of Thin Films." New York, New York: John Wiley and Sons, 1959.

[8]   E. Arzt, "Size effects in materials due to microstructural and dimensional constraints: A comparative review," *Acta Materialia*, vol. 46, pp. 5611-5626, 1998.

[9]   B. C. Prorok, Y. Zhu, H. D. Espinosa, Z. Guo, and Z. P. Bazant, "Micro- and Nanomechanics," in *Encyclopedia of Nanoscience and Nanotechnology*, vol. 5: American Scientific Publishers, 2004, pp. 555-600.

[10]   N. A. Fleck, G. M. Muller, M. F. Ashby, and J. W. Hutchinson, "Strain Gradient Plasticity - Theory and Experiment," *Acta Metallurgica Et Materialia*, vol. 42, pp. 475-487, 1994.

[11]   J. S. Stolken and A. G. Evans, "A microbend test method for measuring the plasticity length scale," *Acta Materialia*, vol. 46, pp. 5109-5115, 1998.

[12]   W. J. Poole, M. F. Ashby, and N. A. Fleck, "Micro-hardness of annealed and work-hardened copper polycrystals," *Scripta Materialia*, vol. 34, pp. 559-564, 1996.

[13]   Q. Ma and D. R. Clarke, "Size-Dependent Hardness of Silver Single-Crystals," *Journal of Materials Research*, vol. 10, pp. 853-863, 1995.

[14]   K. W. McElhaney, J. J. Vlassak, and W. D. Nix, "Determination of indenter tip geometry and indentation contact area for depth-sensing indentation experiments," *Journal of Materials Research*, vol. 13, pp. 1300-1306, 1998.

[15]   M. Hommel and O. Kraft, "Deformation behavior of thin copper films on deformable substrates," *Acta Materialia*, vol. 49, pp. 3935-3947, 2001.

[16]   N. Huber, W. D. Nix, and H. Gao, "Identification of elastic-plastic material parameters from pyramidal indentation of thin films," *Proceedings of the Royal Society of London Series a- Mathematical Physical and Engineering Sciences*, vol. 458, pp. 1593-1620, 2002.

[17]   M. Hommel, O. Kraft, S. P. Baker, and E. Arzt, "Micro-tensile and fatigue testing of copper thin films on substrates," presented at Materials Science of Microelectromechanical Systems (MEMS) Devices, Boston, MA, USA, 1999.

[18]   R. R. Keller, J. M. Phelps, and D. T. Read, "Tensile and fracture behavior of free-standing copper films," *Materials Science and Engineering a-Structural Materials Properties Microstructure and Processing*, vol. 214, pp. 42-52, 1996.

[19]   G. R. Irwin, "Fracture mode transition for a crack traversing a plate," *Journal of Basic Engineering - Transactions of the ASME*, vol. 82, pp. 417-425, 1960.

[20]   A. Hadrboletz, B. Weiss, and G. Khatibi, "Fatigue and fracture properties of thin metallic foils," *International Journal Of Fracture*, vol. 109, pp. 69, 2001.

[21]   M. Klein, A. Hadrboletz, B. Weiss, and G. Khatibi, "The 'size effect' on the stress-strain, fatigue and fracture properties of thin metallic foils," *Materials Science And Engineering A-Structural Materials Properties Microstructure And Processing*, vol. 319, pp. 924, 2001.

[22]   H. D. Espinosa, B. C. Prorok, and B. Peng, "Plasticity size effects in free-standing submicron polycrystalline FCC films subjected to pure tension," *Journal of the Mechanics and Physics of Solids*, vol. 52, pp. 667-689, 2004.

[23]   E. Kroner, "Dislocations and continuum mechanics," *Appl. Mech. Rev*, vol. 15, pp. 599–606, 1962.

[24]   N. A. Fleck and J. W. Hutchinson, "Strain gradient plasticity," in *Advances in Applied Mechanics, Vol 33*, vol. 33, *Advances in Applied Mechanics*, 1997, pp. 295-361.

[25]   M. F. Ashby, "The deformation of plastically non-homogeneous materials," *Philosophical Magazine*, vol. 21, pp. 399-424, 1970.

[26]   A. Arsenlis and D. M. Parks, "Crystallographic aspects of geometrically-necessary and statistically-stored dislocation density," *Acta Materialia*, vol. 47, pp. 1597-1611, 1999.

[27]   N. A. Stelmashenko, M. G. Walls, L. M. Brown, and Y. V. Milman, "Microindentations on W and Mo Oriented Single-Crystals - an Stm Study," *Acta Metallurgica Et Materialia*, vol. 41, pp. 2855-2865, 1993.

[28]   M. S. De Guzman, G. Neubauer, P. Flinn, and W. D. Nix, "The Role of Indentation Depth of the Measured Hardness of Materials," presented at Mater. Res. Soc. Symp., 1993.

[29]   E. P. Busso, F. T. Meissonnier, and N. P. O'Dowd, "Gradient-dependent deformation of two-phase single crystals," *Journal of the Mechanics and Physics of Solids*, vol. 48, pp. 2333-2361, 2000.

[30]   M. R. Begley and J. W. Hutchinson, "The mechanics of size-dependent indentation," *Journal of the Mechanics and Physics of Solids*, vol. 46, pp. 2049-2068, 1998.

[31]   W. D. Nix and H. J. Gao, "Indentation size effects in crystalline materials: A law for strain gradient plasticity," *Journal of the Mechanics and Physics of Solids*, vol. 46, pp. 411-425, 1998.

[32]   H. D. Espinosa and B. C. Prorok, "Size effects of the mechanical behavior of this gold films," presented at Proceedings of the Symposium on Mechanical Properties of MEMS Structures, International Mechanical Engineering Congress, New York, New York, 2001.

[33]   H. D. Espinosa, B. C. Prorok, and B. Peng, "Size effects in submicron gold films subjected to uniaxial tension," *submitted, Journal of the Mechanics and Physics of Solids*, 2003.

[34]   M. G. D. Geers, W. A. M. Brekelmans, and P. J. M. Janssen, "Size effects in miniaturized polycrystalline FCC samples: Strengthening versus weakening," *International Journal Of Solids And Structures*, vol. 43, pp. 7304, 2006.

[35]   J. G. Sevillano, I. O. Arizcorreta, and L. P. Kubin, "Intrinsic size effects in plasticity by dislocation glide," *Materials Science And Engineering A-Structural Materials Properties Microstructure And Processing*, vol. 309, pp. 393, 2001.

[36]   E. O. Hall, "The Deformation And Ageing Of Mild Steel.3. Discussion Of Results," *Proceedings Of The Physical Society Of London Section B*, vol. 64, pp. 747, 1951.

[37]   N. J. Petch, "The Cleavage Strength Of Polycrystals," *Journal Of The Iron And Steel Institute*, vol. 174, pp. 25, 1953.

[38]   A. H. Chokshi, A. Rosen, J. Karch, and H. Gleiter, "On The Validity Of The Hall-Petch Relationship In Nanocrystalline Materials," *Scripta Metallurgica*, vol. 23, pp. 1679, 1989.

[39]   D. Hull and D. J. Bacon, "Introduction to dislocations," 3rd ed. Oxford: Pergamon, 1984.

[40]   J. Weertman and J. R. Weertman, "Elementary Dislocation Theory," 2nd ed. Oxford: Oxford University Press, 1992.

[41]   T. A. Kals and R. Eckstein, "Miniaturization in sheet metal working," *Journal Of Materials Processing Technology*, vol. 103, pp. 95, 2000.

[42]   M. E. Ohern, R. H. Parrish, and W. C. Oliver, "Evaluation Of Mechanical-Properties Of Tin Films By Ultralow Load Indentation," *Thin Solid Films*, vol. 181, pp. 357, 1989.

[43]   W. C. Oliver and G. M. Pharr, "An Improved Technique for Determining Hardness and Elastic- Modulus Using Load and Displacement Sensing Indentation Experiments," *Journal of Materials Research*, vol. 7, pp. 1564-1583, 1992.

[44]   G. M. Pharr and W. C. Oliver, "Measurement Of Thin-Film Mechanical-Properties Using Nanoindentation," *Mrs Bulletin*, vol. 17, pp. 28, 1992.

[45]   G. M. Pharr, "Instrumented Indentation Testing," in *ASM Handbook*, vol. 8, 10 ed, 2000, pp. 232-243.

[46]   R. D. R. C. B. Ponton, "Study of the Effect of the Indentation Time and Load on Fracture Toughness and Crack Morphologies in WC-17Co Thermally Sprayed HVOF Coating," *Mater. Sci. Technol.*, vol. 5, pp. 865, 1989.

[47]   W. D. Nix, "Elastic and plastic properties of thin films on substrates: nanoindentation techniques," *Materials Science and Engineering a-Structural Materials Properties Microstructure and Processing*, vol. 234, pp. 37-44, 1997.

[48]   W. C. Oliver and G. M. Pharr, "Measurement of hardness and elastic modulus by instrumented indentation: Advances in understanding and refinements to methodology," *Journal Of Materials Research*, vol. 19, pp. 3, 2004.

[49]   R. Saha and W. D. Nix, "Soft films on hard substrates -- nanoindentation of tungsten films on sapphire substrates," *Materials Science and Engineering A*, vol. 319-321, pp. 898-901, 2001.

[50]   R. Saha and W. D. Nix, "Effects of the substrate on the determination of thin film mechanical properties by nanoindentation," *Acta Materialia*, vol. 50, pp. 23-38, 2002.

[51]   R. Saha, Z. Xue, Y. Huang, and W. D. Nix, "Indentation of a soft metal film on a hard substrate: strain gradient hardening effects," *Journal of the Mechanics and Physics of Solids*, vol. 49, pp. 1997-2014, 2001.

[52]   G. G. Stoney, "The Tension of Metallic Films Deposited by Electrolysis," *Proceedings of the Royal Society of London A*, vol. 82, pp. 172-175, 1909.

[53]   F. J. von Preissig, "Applicability of the classical curvature-stress relation for thin films on plate substrates," *Journal of Applied Physics*, vol. 66, pp. 4262, 1989.

[54]   A. K. Bhattacharya and W. D. Nix, "Analysis of Elastic and Plastic-Deformation Associated with Indentation Testing of Thin-Films on Substrates," *International Journal of Solids and Structures*, vol. 24, pp. 1287-1298, 1988.

[55]   D. L. Joslin and W. C. Oliver, "A New Method For Analyzing Data From Continuous Depth-Sensing Microindentation Tests," *Journal Of Materials Research*, vol. 5, pp. 123, 1990.

[56]   G. M. Pharr, "Measurement of mechanical properties by ultra-low load indentation," *Materials Science and Engineering A*, vol. 253, pp. 151-159, 1998.

[57]   T. P. Weihs, S. Hong, J. C. Bravman, and W. D. Nix, "Mechanical Deflection of Cantilever Microbeams - a New Technique for Testing the Mechanical-Properties of Thin-Films," *Journal of Materials Research*, vol. 3, pp. 931-942, 1988.

[58]   J. A. Schweitz, "Mechanical Characterization of Thin-Films by Micromechanical Techniques," *Mrs Bulletin*, vol. 17, pp. 34-45, 1992.

[59]   S. P. Baker and W. D. Nix, "Mechanical-Properties of Compositionally Modulated Au-Ni Thin- Films - Nanoindentation and Microcantilever Deflection Experiments," *Journal of Materials Research*, vol. 9, pp. 3131-3145, 1994.

[60]   O. Kraft, R. Schwaiger, and W. D. Nix, "Measurement of Mechanical Properties in Small Dimensions by Microbeam Deflection," *Materials Research Society Symposium Proceedings*, vol. 518, pp. 39-44, 1998.

[61] J. N. Florando, H. Fujimoto, Q. Ma, O. Kraft, R. Schwaiger, and W. D. Nix, "Measurement of thin film mechanical properties by microbeam bending," *Mater. Res. Soc. Symp. Proc.*, vol. 353, pp. 231–236, 1999.

[62] H. D. Espinosa, B. C. Prorok, B. Peng, K. H. Kim, N. Moldovan, O. Auciello, J. A. Carlisle, D. M. Gruen, and D. C. Mancini, "Mechanical properties of ultrananocrystalline diamond thin films relevant to MEMS/NEMS devices," *Experimental Mechanics*, vol. 43, pp. 256, 2003.

[63] J. N. Florando and W. D. Nix, "A microbeam bending method for studying stress-strain relations for metal thin films on silicon substrates," *Journal of the Mechanics and Physics of Solids*, vol. 53, pp. 619-638, 2005.

[64] J. W. Beams, *Structure and properties of thin films*: Wiley, 1959.

[65] J. J. Vlassak and W. D. Nix, "A New Bulge Test Technique for the Determination of Young Modulus and Poisson Ratio of Thin-Films," *Journal of Materials Research*, vol. 7, pp. 3242-3249, 1992.

[66] M. K. Small and W. D. Nix, "Analysis of the Accuracy of the Bulge Test in Determining the Mechanical-Properties of Thin-Films," *Journal of Materials Research*, vol. 7, pp. 1553-1563, 1992.

[67] F. R. Brotzen, "Mechanical Testing of Thin-Films," *International Materials Reviews*, vol. 39, pp. 24-45, 1994.

[68] O. Kraft and C. A. Volkert, "Mechanical testing of thin films and small structures," *Advanced Engineering Materials*, vol. 3, pp. 99-110, 2001.

[69] D. T. Read and J. W. Dally, "A New Method For Measuring The Strength And Ductility Of Thin-Films," *Journal Of Materials Research*, vol. 8, pp. 1542, 1993.

[70] D. T. Read, "Piezo-actuated microtensile test apparatus," *Journal Of Testing And Evaluation*, vol. 26, pp. 255, 1998.

[71] I. Chasiotis and W. G. Knauss, "Microtensile tests with the aid of probe microscopy for the study of MEMS materials," *Proceedings SPIE*, vol. 4175, pp. 96-103, 2000.

[72] I. Chasiotis and W. G. Knauss, "A new microtensile tester for the study of MEMS materials with the aid of atomic force microscopy," *Experimental Mechanics*, vol. 42, pp. 51-57, 2002.

[73]   Y. W. Cheng, D. T. Read, J. D. McColskey, and J. E. Wright, "A tensile-testing technique for micrometer-sized free-standing thin films," *Thin Solid Films*, vol. 484, pp. 426, 2005.

[74]   S. Greek, F. Ericson, S. Johansson, M. Furtsch, and A. Rump, "Mechanical characterization of thick polysilicon films: Young's modulus and fracture strength evaluated with microstructures," *Journal Of Micromechanics And Microengineering*, vol. 9, pp. 245, 1999.

[75]   S. Greek, F. Ericson, S. Johansson, and J. A. Schweitz, "In situ tensile strength measurement and Weibull analysis of thick film and thin film micromachined polysilicon structures," *Thin Solid Films*, vol. 292, pp. 247, 1997.

[76]   J. A. Ruud, D. Josell, F. Spaepen, and A. L. Greer, "A New Method For Tensile Testing Of Thin-Films," *Journal Of Materials Research*, vol. 8, pp. 112, 1993.

[77]   W. N. Sharpe, B. Yuan, and R. L. Edwards, "A new technique for measuring the mechanical properties of thin films," *Journal of Microelectromechanical Systems*, vol. 6, pp. 193-199, 1997.

[78]   T. Tsuchiya, J. Sakata, M. Shikida, and K. Sato, "Tensile Test of Bulk- and Surface-Micromachined 0.1-µm Thick Silicon Film Using Electrostatic Force Grip System," *Mater. Res. Soc. Sym. Proc.*, vol. 687, pp. B5.45, 2002.

[79]   T. Tsuchiya, O. Tabata, J. Sakata, and Y. Taga, "Specimen size effect of tensile strength of surface- micromachined polycrystalline silicon thin films," *Journal of Microelectromechanical Systems*, vol. 7, pp. 106-113, 1998.

[80]   T. Y. Zhang, Y. J. Su, C. F. Qian, M. H. Zhao, and L. Q. Chen, "Microbridge testing of silicon nitride thin films deposited on silicon wafers," *Acta Materialia*, vol. 48, pp. 2843, 2000.

[81]   A. Acharya, J. L. Bassani, and A. Beaudoin, "Geometrically necessary dislocations, hardening, and a simple gradient theory of crystal plasticity," *Scripta Materialia*, vol. 48, pp. 167-172, 2003.

[82]   B. C. Prorok and H. D. Espinosa, "Effects of nanometer-thick passivation layers on the mechanical response of thin gold films," *Journal of Nanoscience and Nanotechnology*, vol. 2, pp. 427-433, 2002.

[83]   H. D. Espinosa, B. C. Prorok, and M. Fischer, "A methodology for determining mechanical properties of freestanding thin films and MEMS materials," *Journal of the Mechanics and Physics of Solids*, vol. 51, pp. 47-67, 2003.

[84]   T. H. Coutrney, *Mechanical Behavior of Materials*. New York: McGraw Hill, 1990.

[85]   J. A. Venables, "Nucleation + Propagation of Deformation Twins," *Journal of Physics and Chemistry of Solids*, vol. 25, pp. 693-&, 1964.

CHAPTER 2

THEORETICAL FOUNDATIONS

This chapter is aimed at giving a broad yet specific review of some established theoretical framework that has been developed to provide a better explanation of the mechanical behavior of polycrystalline metals. These theories are chosen because of their promising potential of being incorporated into the thin film mechanics with appropriate modifications accounting for the unique geometry associated with thin films.

2.1 Elasticity

Elastic deformation is characterized as being instantly reversible, meaning that a deformed structure recovers its original size and shape when all the applied loads are removed. In the elastic region, these deformations can often be modeled as being linearly dependent on the applied load and are described by the generalized Hooke law [1] which defines a constitutive relation between stresses and strains.

$$\sigma = C\varepsilon \ \text{ or } \ \varepsilon = S\sigma \tag{2-1}$$

The strains are uniquely determined by the stress tensor. Tensile loading in one direction (assume the x-direction) produces a proportional elongation on the sample. The ratio of the stress to the strain is called as Young's modulus or modulus of elasticity. The elongation simultaneously produces a contraction in the other directions (y and z

directions) proportional to the longitudinal elongation, the ratio of which is Poisson's ratio.

2.1.1 Elastic Anisotropy

In equation (2-1), the stress tensor σ and the strain tensor ε are second order tensors while the elastic stiffness tensor C and elastic compliance S tensor are fourth order tensors with up to 21 independent matrix elements in general. However, as a result of symmetry considerations, for a face-centered cubic (FCC) crystal like gold, there are only 3 independent elastic constant needed: C_{11}, C_{12} and C_{44} or S_{11}, S_{12} and S_{44}. In general, most crystalline materials have anisotropic elastic properties, and the degree of anisotropy of different materials can be expressed by the elastic anisotropic ratio ρ_{EA} or the relative degree of anisotropy value [2]:

$$\rho_{EA} = \frac{C_{11} - C_{12}}{2C_{44}} \text{ or } \rho_{RDA} = \frac{2(S_{11} - S_{12})}{S_{44}} \tag{2-2}$$

If ρ_{EA} or ρ_{RDA} equals to 1, the material behavior is isotropic meaning that the modulus of elasticity is independent of the crystal orientation, an example material is tungsten. However, single crystal gold, on the other hand, is clearly not the case, as can be seen in Table 2.1 and 2.2, which list all the elastic constants and the elastic anisotropy for gold. Therefore, Young's modulus $E_{[hkl]}$, i.e. the stiffness which relates the stress applied in a direction [hkl] to the strain generated in the same direction, depends on the crystal orientation. This dependence has a convenient form in terms of compliances [3]:

$$\frac{1}{E_{[hkl]}} = S_{11} - 2(S_{11} - S_{12} - \frac{1}{2}S_{44})(\alpha^2\beta^2 + \alpha^2\gamma^2 + \beta^2\gamma^2) \tag{2-3}$$

where α, β and γ are the direction cosines of the [hkl] direction and the cubic axis [100], [010] and [001], respectively. $E_{[hkl]}$ can be also expressed in terms of $E_{[100]}$ and $E_{[111]}$:

$$\frac{1}{E_{[hkl]}} = \frac{1}{E_{[100]}} - 3(\frac{1}{E_{[100]}} - \frac{1}{E_{[111]}})(\alpha^2\beta^2 + \alpha^2\gamma^2 + \beta^2\gamma^2) \qquad (2\text{-}4)$$

Table 2.1: Elastic stiffness and compliance constants for Au single crystal [4].

C_{11}	C_{12}	C_{44}	S_{11}	S_{12}	S_{44}
(10^{10} Pa)			(10^{-11} Pa^{-1})		
18.60	15.70	4.20	2.33	-1.07	2.38

Table 2.2: Elastic anisotropy for Au at room temperature

$E_{[100]}$	$E_{[110]}$	$E_{[111]}$	E_{Poly}	ρ_{EA}	ρ_{RDA}
(GPa)					
43	82	117	78	0.345	2.857

Most polycrystalline metals are often assumed to behave uniformly in their bulk form, exhibiting equal strength in all directions because the anisotropy of individual crystals is presumed to be smoothed out in the presence of a large number of grains having a random distribution of orientations. Actually, a macroscopic anisotropy usually remains to a certain extent due to the existence of preferred orientations and its magnitude depends upon the statistical distribution of grain orientations, i.e. the "crystallographic texture", more simply called the texture [5, 6]. And this preferred texture is more manifest in the case of polycrystalline thin films, which generally show textures that may by very strong. For elastically anisotropic polycrystalline materials, both the degree of texture (grain orientation distribution) and the elastic anisotropy of the crystalline that compose the polycrystalline thin films play a role in deciding the amplitude of the texture induced elastic anisotropy [7].

36

The calculation of upper and lower bounds of the elastic modulus for elastically anisotropic polycrystalline thin films is rather simple; whereas, the calculation of a rigorous average could be quite difficult, as strain compatibility and stress equilibrium for all the grains have to be satisfied. Several elastic grain interaction models have been proposed in an effort to assist the appropriate estimation of the elastic modulus for elastically anisotropic polycrystalline thin films. The most well known ones are Ruess [8], Voigt [9] and Neerfeld-Hill [10] models. In the Ruess approximation, uniform stresses are assumed in contrast to the Voigt approximation where uniform strains are assumed. The Ruess approximation gives a lower bound for Young's modulus while the Voigt approximation yields an upper bound. The texture effect on elastic properties of studied thin films will be discussed in detail in chapter 6.

2.1.2 Anelasticity

Elastic deformation is generally acclaimed as a time independent behavior, an applied stress produces an instantaneous elastic strain that remains constant over the period of time the stress is maintained. It has also been assumed that upon release of the load the strain is immediately and totally recovered. However, in most engineering materials, there also exists a time-dependent elastic strain component. That is, elastic deformation will continue after the stress application. And upon load release some finite time is required for complete recovery. This time-dependent elastic behavior is known as anelasticity, and it is due to time-dependent microscopic and atomistic processes that are attendant to the deformation. For metals in their bulk form, the anelastic component is normally small and is often neglected. However, when the materials structure and their

microstructures shrink down to the micro or even nano scale, the anelasticity component may become noticeable in the overall elastic deformation.

2.1.3 Nanocrystalline Elasticity

Nanocrystalline materials have been the subject of widespread research over the past couple of decades. Yet the theoretical understandings in their distinctive properties are still in its early stage. As the name suggests, they are single or multi-phase polycrystals with nanoscale grain size (1 nm – 100 nm) [11, 12]. Nanocrystalline materials are structurally characterized by a large volume faction of grain boundaries, which may significantly alter their physical, mechanical, and chemical properties in comparison with conventional coarse-grained polycrystalline materials. As the grain size is decreased, an increasing fraction of atoms can be ascribed to the grain boundaries. Nanocrystalline materials may exhibit increased strength/hardness, improved toughness, reduced elastic modulus and ductility etc. At this point, our attention will be focused on the reduced elastic modulus.

The reduced Young's moduli for polycrystalline thin gold films were reported by several groups [13-16], along with some plausible explanations were proposed. In kalkman's study of free standing thin metal films, their measured elastic modulus for polycrystalline thin gold films reduced 5 % to 20 % compared to the bulk value of 78 GPa as a function of applied modulation frequency [16]. And they attributed the reduced values of the elastic modulus to the relatively small grain size, which induced significant grain boundary sliding in thin metal films even at room temperature.

Another report given by Haque and Saif [15] where they found that the Young's modulus of the small-grained (15 nm) film is 52 GPa while the modulus is 73 GPa for the

larger grained (75 nm) sample with both film possessing the same texture. A couple of implications were made based on their observations in this study: a) grain size becomes a critical dimension that determines the mechanical properties such as Young's modulus, when the grains are much smaller (2-3 times) than the film thickness; b) elastic modulus decreases with decreasing grain size when the films grain size is in a very small regime (50 nm or smaller); c) upon unloading, the metals behave nearly as nonlinear elastic. A fairly new mechanism was proposed at the end of this study to explain both reduced Young's modulus and nonlinear elasticity of nanograined sputter deposited thin films at room temperatures: grain boundary region is elastically softer than grain interior, and it becomes increasingly softer with increasing tensile strain.

2.2 Plasticity and Relevant Strengthening Mechanisms

As the material is deformed beyond the elastic region, the stress is no longer proportional to strain in accordance with Hooke law and permanent, nonrecoverable plastic deformation begins to take place.

2.2.1 Plasticity

In single crystals, plastic deformations are accommodated by a series of dislocation motion through the lattice, which is termed as the slip process. Apparently, a certain force is necessary to move the dislocation through the lattice and this force is called Peierls force [17]. The Peierls force depends to a large extent on the width of the dislocation W and the distance between similar planes a in the following fashion [1]:

$$\tau_{p-n} \propto Ge^{-2\pi W/b} \text{ (where } W = \frac{a}{1-\upsilon}) \tag{2-5}$$

Therefore, in an effort to minimize the Peierls stress, slip occurs predominantly on closely packed planes that possess the maximum atomic density. In addition, slip also preferred to occur in the close-packed direction, which represents the shortest distance between two equilibrium atom positions and, hence, the lowest energy direction. In FCC crystals the slip plane is the family of {111} planes and the slip direction is in <110> direction, which yield a total of 12 slip systems available for FCC crystals. Plastic deformation will occur when the resolved shear stress τ_{RSS} reaches a critical value τ_{CRSS} which represents the yield strength of the single crystal [1]. And as the following equation (2-6) indicated, that the yielding will occur on the slip system possessing the greatest Schmid factor.

$$\tau_{RSS} = \frac{P}{A} \cos\phi \cos\lambda \qquad (2\text{-}6)$$

Beside slip, twinning is another mode of plastic deformation, which will be activated if the number of independent slip systems in a crystal is not sufficient enough. The nucleation of a twin requires large stress concentration while the growth of a twin needs much less. For FCC metals, the type of deformation twinning is found least frequently while annealing twins may exhibit only under the circumstance that the grain growth during the recrystallization has encountered packing sequence defects from previously deformed material. Hence, FCC metals possessing low stacking fault energy are more likely to facilitate the presence of annealing twins [1, 18].

Although slip is the most basic deformation mechanism for both single crystal and polycrystalline metals, the complexity of the polycrystals situation is increased dramatically because of the numerous randomly orientated grains. The overall plastic

deformation of a polycrystalline material corresponds to the comparable distortion caused by slips of individual grains in their individual favored microsystems. Nonetheless, because the mechanical integrity and coherency are maintained along the grain boundaries, restraints are produced and imposed on the grains during deformation, which is also the cause of why polycrystals required higher stress to initiate slip and the attendant yielding. And for each crystal with different orientation with respect to the loading axis, the external stress required to produce yielding will differ. Hence, it is expected that the type of crystal, the grain size, the orientation, as well as their distribution, will have somewhat impact on the mechanical behavior of polycrystalline materials, and the extent of these effects will become more obvious in the case of thin polycrystalline films due to the additional geometrical constraints imposed by the dimension of the structure itself.

2.2.2 Hall-Petch Relationship and Inverse Hall-Petch Behavior

It was generally believed that the presence of grain boundaries in polycrystalline materials cause dislocation pile-ups by acting as effective barriers to the movement of glide dislocations. The Hall-Petch relationship [19, 20] was originally proposed to describe this strengthening mechanism by express the dependence of the yield strength on the grain size in the following equation:

$$\sigma_y = \sigma_0 + K_{H-P}d^{-1/2} \tag{2-7}$$

where σ_0 is the intrinsic stress caused by lattice friction, can also considered as the yield strength of a single crystal. K_{H-P} is the Hall-Petch parameter, represent the sensitivity of the strength to a change in grain size; σ_y and d are the yield strength and grain size respectively. This relation has been tested valid for grain sizes ranging from

micrometers to millimeters, but is not applicable in the cases for both extremely large grains and extremely fine grains. And our attention will be focused on the latter case.

Thin films are mostly presented with relatively fine grained microstructures, grain size of one micrometer or less, the size regime around where the Hall-Petch relationship was predicted to begin to loss its validity [12, 21-26]. Because of the much smaller grains, fewer dislocations are presented in each grain and the length available to any dislocation pile-up decreases, which all lead to the failure of the pile-up model based Hall-Petch relationship at small grain size. While the exact dimension at which this transition would occur is not clear, alternative theories involving discrete pile-ups and single dislocation expansion have been proposed to predict modified grain size dependence. Furthermore, some evidences and reasons have shown that the grain boundary induced dislocation pile-ups may not be the only mechanism responsible for the yielding phenomena, model about grain boundary serving as a source of dislocations instead of being barriers to dislocation flow may also played an important role to make its own contribution to the yield strength-grain size relationship [27].

The situation becomes even more complicated when the grain size is in the deep sub-micro regime (50 nm or less). Generally these ultra fine-grained materials are reported to be softer than what predicted by extrapolation of the Hall-Petch equation, but the amount of the softening reported by different researchers on various materials initiated new argument on insight mechanism. There are observations of "kinked" Hall-Petch graphs, i.e. cases where the slope of the Hall-Petch relation is reduced but still positive. Once the grain size is reduced down below a critical value (the "critical grain size"), the Hall-Petch trend will breakdown with a negative slope, which is referred as the

"Inverse Hall-Petch relation". As shown in Figure 2-1, the Hall-Petch curve for the nanocrystalline range clearly shows a deviation from the regular trend in the microcrystalline range.
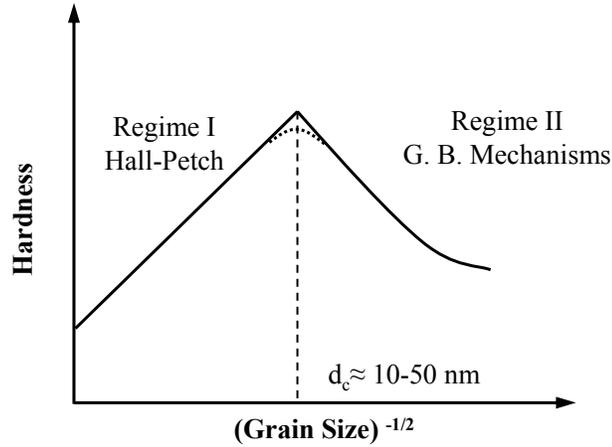
Figure 2-1 Schematic of the variation of hardness H as a function of grain size d.
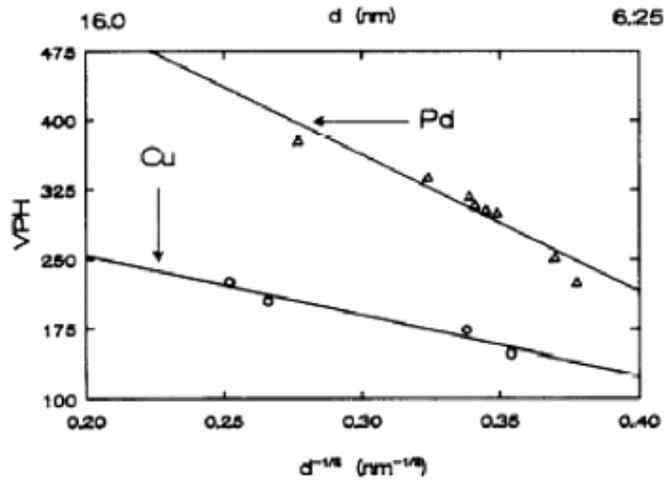
Figure 2-2 Hardness vs. grain size, $d^{-1/2}$ for nanocrystalline Cu and Pd, reported by Chokshi et al. [21].

The Inverse Hall-Petch behavior was reported firstly by Chokshi et al. on nanocrystalline Cu and Pd prepared by the gas condensation method. A clear inverse Hall-Petch behavior was observed, as shown in Figure 2-2. Similar trend was reported by

some other sources [21, 22, 24] later. This behavior is also referred as the negative Hall-Petch relation, i.e., the yield stress actually decreases when the grain sizes are further reduced. Many explanations have been proposed. Chokshi attributed this negative trend to the occurrence of rapid diffusional creep in nanocrystalline copper at room temperature analogous to grain-boundary sliding in conventionally-grained samples at high temperature. Coble creep was considered as the deformation mechanism [21]. Nieh and Wadsworth stated that once the grain size drops below the equilibrium distance between dislocations in a pileup, pileups are no longer possible, and the Hall-Petch relation should cease to valid [28, 29]. The critical grain size is estimated to be 20 nm for copper, yet how the yield strength should depend on the grain size below that point is not clear. It is not unreasonable to assume that the grain boundary structure might be different when the grain size is very small. It has been proposed that grain boundaries in nanocrystalline metals may be more "transparent" to dislocations, and thus allow dislocations to run through several grains. Another approach is to assume that as the grain size is reduced, the volume fraction of the grain boundaries increase and at some point they will begin to play a role in the deformation process. Li, Sun and Wang proposed a deformation mechanism based on motion of grain boundary dislocations [27, 30].

It is worth to mention at this point that many of the observations of a reverse Hall-Petch effect are from samples generated using inert gas condensation (IGC) method, by which a large number of nanometer-sized clusters are compacted to produce the sample. In this method, if the compaction is not complete, small voids will be present between the grains. The presence of these voids was not initially recognized, the lower density being ascribed to special low-density grain boundaries. If the nanocrystalline metal contains a

significant volume fraction of porosity, this will obviously reduce the hardness significantly. Surface defects alone have been shown to be able to reduce the strength of nanocrystalline metals by a factor of five [26, 29]. Furthermore, improved techniques [31] have allowed production of nanocrystalline samples with densities above 98 %, and no reverse Hall-Petch effect in copper has been shown at grain sized down to 10-15 nm [32]. Therefore, the genuineness of the observed negative Hall-Petch effect raised the debate by many researchers. And because there is no sufficient information to validate the existence of this effect, the real trend is still to be determined along with the knowledge for different materials below a critical grain size.

2.2.3 Texture Strengthening in Thin Films

In FCC crystals, slip occurs by movement of dislocations on close-packed {111} planes in the <110> close-packed directions. The amount of external load that is required to cause a crystal to yield will depend on the direction of loading relative to these planes and directions. It can be shown that if a shear stress τ_c is required to cause slip, the external stress, σ_e, necessary to initiate this slip will be

$$\sigma_e = \frac{\tau_c}{\cos\phi\cos\lambda} \qquad (2\text{-}8)$$

where ϕ is the angel between the tensile direction and the slip plane normal, and λ is the angle between the tensile direction and the slip direction. This is also written

$$\sigma_e = \frac{\tau_c}{m_s} \qquad (2\text{-}9)$$

where m_s is called the Schmid factor. Clearly, m_s will vary as a function of the orientation of the tensile axis with respect to the crystal lattice. For this reason, uniaxial tensile tests

45

performed on single crystals of the same material, but with the tensile axis aligned differently, will produce different stress-strain curves.

When dealing with a polycrystal the complexity of the situation is increased by the requirement for continuity between neighboring grains. Because of this, most grains will need several slip systems active during even the simplest external deformations in order to maintain compatibility. Again, for each crystal with different orientation with respect to the loading axis, the external stress required to produce yielding (in that grain) will differ. The behavior of the polycrystal will depend on the behavior of the individual crystals by themselves, as well as their distribution throughout the polycrystalline sample.

A common assumption when dealing with materials in bulk form is that the grain size is much smaller than the external dimensions of bodies they comprise. Another is that the orientation of each crystal is random in space. With these two assumptions, the effects of the differing yield strengths of the individual grains can be ignored when considering a bulk sample. These effects can no longer be ignored when the grains of a body develop texture. Texture refers to the development of preferred orientations within a polycrystal. For example, evaporated FCC metal films often develop a microstructure with many grains have a <111> direction parallel to the normal to the substrate surface and often tend to grow at the expense of other orientations because the {111} planes have the lowest surface energy.

When a sample does not contain a random distribution of crystal orientations, the external load at which it yields will differ from the yield strength found for a random polycrystal of that material. Texturing can cause a polycrystal to be either stronger or

weaker than a random sample, and texturing effects must be considered when investigating strength.

The yield stress of a polycrystalline film depends strongly on its average in-plane grain size and out-of-plane grain size, the latter being the film thickness, h, or less [33-36]. The yield stress σ_y increases with decreasing value of both h and d, and in the case of Al, has been shown to independently vary with the reciprocal of each, such that

$$\sigma_y = \frac{c_1}{d} + \frac{c_2}{h}$$

(2-10)

It has been further argued that both c_1 and c_2 can be defined for individual grains, and that their values depend on the texture of a grain such that σ_y is high for grains with (111)-texture and low for grains with (210) and (110) textures. This orientation dependence is predicted based largely on the magnitude of resolved sheer stress [37].

2.3 Creep and Strain Rate Sensitivity

Creep is characterized as the time-dependent (strain rate dependent), irreversible deformation of materials when subjected to a constant load or stress. From the micro mechanisms perspective, creep is accomplished either by atomic diffusion or by dislocation movement. Therefore, creep can be generally divided into two groups: (a) dislocation involved Power Law creep; and (b) diffusional flow creep. In each group, different mechanisms may control or compete for the overall behavior in complicated ways. A creep mechanism 'family tree' was constructed and displayed in Figure 2-3 for clarity.

47
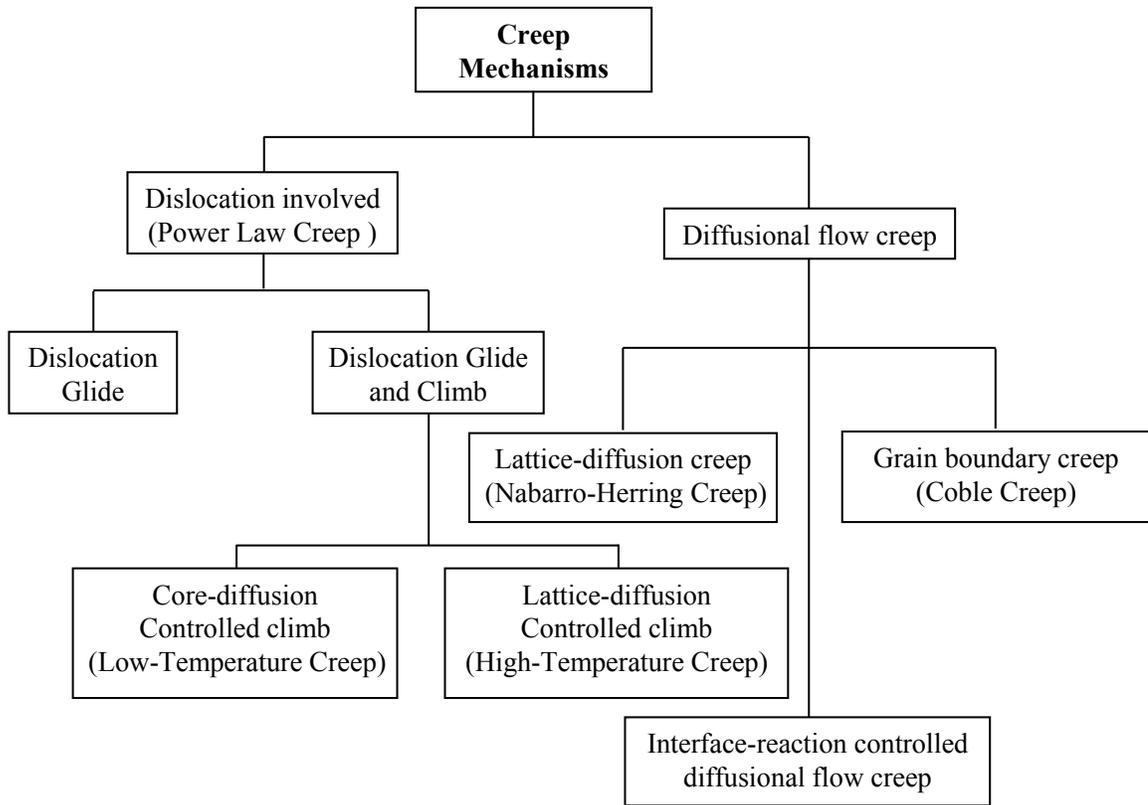
Figure 2-3 Schematic of the creep mechanism displayed as a 'family tree'

Both temperature and the level of the applied stress influence the creep characteristics. Empirical relationships have been developed in which the steady-state creep rate as a function of stress and temperature is expressed. Its dependence on stress can be written as

$$\dot{\varepsilon} = A\sigma^n \tag{2-11}$$

where $\dot{\varepsilon}$ is the strain rate, specifically, the steady-state creep rate is considered in this section. σ is the tensile stress and A and n are the material constants. n is termed as stress exponent generally. When the influence of temperature is included, Equation (2-11) becomes

$$\dot{\varepsilon} = B\sigma^n \exp(-\frac{Q}{RT}) \tag{2-12}$$

where B is constant; Q is the activation energy for creep. R is the gas constant and T is the absolute temperature. Equation (2-11) and (2-12) are the general expression for describing the stress and temperature dependency for creep. As shown in the creep mechanism chart, several theoretical mechanisms have been proposed to explain the creep behavior for various materials; these mechanisms involve stress-induced vacancy diffusion, grain boundary diffusion, dislocation motion, and grain boundary sliding etc. Each leads to a different model and numerical expression to describe creep strain rate in terms of a varied value of the stress exponent n and the material constant A and B. In addition, correlations have been made between the activation energy for creep and the activation energy for diffusion.

Creep in bulk materials has been studied extensively for decades. The results of the creep data were well-represented in the form of deformation mechanism maps by

Frost and Ashby [38]. These maps indicate stress-temperature regimes over which various mechanisms operate. Constant strain rate contours are often superimposed on the fields. Thus, for some creep situations, given any two of the three macroscopic variables: temperature, stress level, and creep strain rate, the third may be determined by the map. However, there are reasons to believe that thin films, with their unique two-dimensional geometry and much smaller-scaled microstructure, would exhibit different creep behavior. As the dimensions of thin film in one direction begin to approach the scale of material microstructure features and even the mean free path of the mobile dislocations, a large fraction of these dislocations can easily escape from the free surface and the surface energy term becomes more significant. These are the important issues when considering the creep mechanism in the deformation of free-standing thin films. It is unlikely that the lattice diffusional creep is the dominant mode of deformation in thin films at moderate temperatures. Moreover, from the few measurements of thin film creep behavior reported by several researchers, the creep mechanism for thin films are most likely based on the dislocation climb and glide and grain boundary diffusion to some extent. Therefore, these two mechanisms are addressed with details in this section.

2.3.1 Dislocation Climb-and-Glide Creep (Power Law Creep) in Thin Films

Dislocations can move through crystals by two types of motion: the conservative one as glide and the non-conservative one as climb. Glide is the movement of a dislocation in its glide plane by the incremental breaking and reforming of bonds. Climb is the movement of a dislocation line out of its normal glide plane by diffusion-assisted removal of atoms (diffusion of lattice vacancies to the bottom of the extra half plane). So when a gliding dislocation is held up by discrete obstacles, climb may release and

allowing it to glide once again. The glide portion of the motion is generally regarded as occurring much faster than the climb portion and is responsible for almost all of the strain, and the average velocity is determined by the rate at which the climb process occurs. Mechanism which is based on this climb-glide sequence is referred to as climb-controlled or climb-and-glide creep.

The most important feature about this creep mechanism is that the process is controlled at an atomic level, by the diffusive motion of single ions or vacancies to or from the climbing dislocation site. And there are two ways available to assist transporting the matter in this process: lattice diffusion and dislocation core diffusion. Since vacancy diffusion is a thermally activated process, dislocation climb becomes an important process at elevated temperatures. At high temperatures (above $0.6T_M$) and low stresses, climb is mainly controlled by lattice diffusion, and the resulting creep field is high-temperature creep. While at lower temperatures, or higher stresses, core diffusion begin to contribute to the overall diffusive process significantly, and is often referred as low temperature creep.

According to the experimental observations and empirical analysis, a relationship has been developed between tensile stress and strain rate for the dislocation climb controlled creep, as shown in equation (2-13). This is the general expressions of what is termed as "Power-law creep".

$$\dot{\varepsilon} = A\frac{DGb}{kT}(\frac{\sigma}{G})^n \qquad (2\text{-}13)$$

where $\dot{\varepsilon}$ is the steady state strain rate, σ is the tensile stress. G is the shear modulus, b is the Burgers vector magnitude, k is the Boltzmann's constant, T is the absolute temperature,

D is the diffusivity, A and n are constants. The values of D, A and n are all depending on the testing conditions.

In the earlier stage of creep study, lattice diffusion was considered as the only diffusive mechanism controlling the dislocation climb rate for most materials, and equation (2-14) is written as

$$\dot{\varepsilon} = A\frac{D_v Gb}{kT}(\frac{\sigma}{G})^n \qquad (2\text{-}14)$$

where the diffusivity term D in equation (2-13) is now specified as the lattice diffusion coefficient D_v. This equation provides a good description of experimental observations for most materials who exhibit Power-law creep over a certain range of stress. However, the wide variety for the values of n (from 3 to about 10) and the dimensionless constant A_1 (from unity up to 10^{15}) [39]; plus a drop in the activation energy for creep at lower temperatures are all strongly suggest that lattice diffusion may not be the only diffusive process involved, an other possible way of vacancy diffusion might be oversighted. Therefore, the dislocation core diffusion is assumed as another possible diffusion path, which may contribute considerably to the overall diffusional vacancy flow and become a dominant transport mechanism under certain circumstances [40]. The contribution of core diffusion is included by defining an effective diffusion coefficient, and now the strain rate is described as following:

$$\dot{\varepsilon} = \frac{AD_{eff}Gb}{kT}(\frac{\sigma}{G})^n \qquad (2\text{-}15)$$

where the diffusivity term D_{eff} is called as effective diffusion coefficient, which can be defined as:

$$D_{eff} = D_v f_v + D_c f_c \tag{2-16}$$

where D_c is the core diffusion coefficient, f_v and f_c are the fractions of atom sites associated with each type of diffusion [40, 41].

The value of f_v is essentially unity. The value of f_c is determined by the dislocation density ρ as $f_c = a_c \rho$, where a_c is the cross-sectional area of the dislocation core in which fast diffusion is taking place. And a_c is usually approximated b^2 or $2\delta^2$ (where δ is the effective boundary thickness). The dislocation density is estimated by the expression $\rho = \alpha(\sigma/bG)^2$ and α is a constant of order unity. By employing the values of f_v and f_c, the effective diffusion coefficient can be written as:

$$D_{eff} = D_v + \alpha \frac{a_c}{b^2} (\frac{\sigma}{G})^2 D_c \tag{2-17}$$

Insert the effective diffusion coefficient back into equation (2-13), the Power-law relationship between the stress and steady-state strain rate can be expressed in a more comprehensive way as following:

$$\dot{\varepsilon} = A_1 \frac{D_v Gb}{kT} (\frac{\sigma}{G})^n + A_2 \frac{D_c Ga_c}{bkT} (\frac{\sigma}{G})^{n+2} \tag{2-18}$$

2.3.2 Grain Boundary Diffusion (Coble Creep) in Thin Films

For deformation due to diffusional flux of matter through and around the surfaces of the grains, the mostly agreed model predicting this diffusion-controlled process is as following: and this flux leads to strain, provided it is coupled with sliding displacements in the plane of the boundaries themselves. Most models of the process assume that it is coupled. They are in substantial agreement in predicting a rate-equation: if both lattice and grain boundary diffusion is permitted, the rate-equation for diffusional flow is:

53

$$\dot{\varepsilon} = \frac{42 D_{eff} \delta \Omega \sigma}{d^2 kT} \qquad (2\text{-}19)$$

Through the lattice, the velocity of the diffusing atoms in the x-direction

$$v_a = \frac{D_s}{kT} \frac{\partial \mu}{\partial x} \qquad (2\text{-}20)$$

where D_s is the self-diffusivity, k is Boltzmann's constant, T is temperature, and μ is the chemical potential of an atom at the boundary of a grain. The chemical potential is usually written

$$\mu = \mu_0 + \sigma_N \Omega \qquad (2\text{-}21)$$

Assuming that the dominant diffusion creep mechanism can be expressed as the following equation proposed by Coble [42],

$$\dot{\varepsilon} = \frac{148 D_g \delta \Omega \sigma}{\pi d^3 kT} = \frac{148 D_{g0} \delta \Omega \sigma}{\pi d^3 kT} \exp\left(-\frac{Q_g}{kT}\right) \qquad (2\text{-}22)$$

where $\dot{\varepsilon}$ is the strain rate, σ is the applied stress, D_g is the grain boundary diffusion coefficient, D_{g0} is the diffusivity constant, Q_g is the activation energy, δ is the thickness of grain boundaries, Ω is the atomic volume, d is the grain size, k is Boltzmann's constant, and T is temperature.

2.3.3 Strain Rate Sensitivity in Thin Films

Nevertheless, because of the microscale dimension of thin films, the applied strain rate are more easily and likely to reach the range where creep would occur even at the room temperature for some metals. Therefore, the strain rate effect on the mechanical response of metallic thin films had drawn an increased attention from the research groups everywhere [43-45]. The early observation of creep processed in gold at room

temperature with a holding time of 10^3 to 10^5 s was found by Sakai and Tanimoto's work [46, 47], in which they claimed that the plastic deformation for nanocrystalline gold with grain size of 15-60 nm at room temperature is dominated partially but inevitably by the applied strain rate. Although the gold studied in Sakai and Tanimoto's work is in bulk form instead of as a thin film, their assessment of coble creep at room temperature in nanocrystalline gold had shed new light to the importance of considering the strain rate issue in predicting the mechanical performance. Later on, Emery and Povirk [14, 48] performed a study with systematic change of strain rates on the Ebeam evaporated free-standing gold thin films, with thickness varied from 0.23 μm to 2.10 μm, grain size in the range of 200 nm to 500 nm. From their work, it was concluded that strain rate dependent behavior is an indication of the stress driven diffusion assisted deformation mechanism. They also stated that the strain rate dependent behavior is grain size sensitive. Films with grain size larger than 500 nm rarely show any dependence on applied strain rate, while films with finer grains (less than 500 nm) show a strong dependence. More recently, Chasiotis et al. [45] reported the strain rate effects on the mechanical behaviors of evaporated and electroplated gold films with thickness of ~ 0.50 μm and 2.80 μm; grain size in the range of 100 nm to 200 nm. Mechanical properties including ultimate strain, yield strength and even effective Young's modulus were found to be impacted to different extent by the applied strain rates ranging from 10^{-3} s^{-1} to 10^{-6} s^{-1}. To this end, the aforementioned works have shown that the strain rate could induce a considerable impact on how metallic thin films deform at a certain loading condition. And therefore, being able to foresee the mechanical response of thin films under a certain applied strain rate becomes very important and critical for the design and prediction of the performance

55

and reliability of the thin film components involved in the microelectronics or Microelectromechanical system. However, the literature information related to this subject is still in great need at this point.

2.4 References

[1]   R. W. Hertzberg, *Deformation and Fracture Mechanics of Engineering Materials*, 4 ed. New York: John Wiley & Sons, 1996.

[2]   W. F. Hosford, *The Mechanics of Crystals and Textured Polycrystals*. New York: Oxford University Press, 1993.

[3]   T. H. Coutrney, *Mechanical Behavior of Materials*. New York: McGraw Hill, 1990.

[4]   H. B. Huntington, *Solid State Physics*, vol. 7. New York: Academic, 1958.

[5]   W. N. Reynolds, "Preferred orientation in polycrystalline materials," *Journal Of Physics D-Applied Physics*, vol. 3, pp. 1798-1802, 1970.

[6]   K. W. Andrews, "Elastic-Moduli Of Polycrystalline Cubic Metals," *Journal Of Physics D-Applied Physics*, vol. 11, pp. 2527, 1978.

[7]   S. R. Agnew and J. R. Weertman, "The influence of texture on the elastic properties of ultrafine-grain copper," *Materials Science and Engineering A*, vol. 242, pp. 174-180, 1998.

[8]   A. Reuss, "Account of the liquid limit of mixed crystals on the basis of the plasticity condition for single crystal," *Z. Angew. Math. Mech.*, vol. 9, pp. 49-81, 1929.

[9]   W. Voigt, *Lehrbuch der Kristallphysik*. Leipzig: Teubner, 1928.

[10]   R. Hill, "The Elastic Behaviour Of A Crystalline Aggregate," *Proceedings Of The Physical Society Of London Section A*, vol. 65, pp. 349, 1952.

[11]   H. Gleiter, "Nanocrystalline Materials," *Progress In Materials Science*, vol. 33, pp. 223, 1989.

[12]   C. Suryanarayana, "Nanocrystalline Materials," *International Materials Reviews*, vol. 40, pp. 41, 1995.

[13]   G. S. Long, D. T. Read, J. D. MsColskey, and K. Crago, "Microstructural and mechanical characterization of electrodeposited gold films," *ASTM Special Technical Publication*, vol. 1413, pp. 262, 2001.

[14]   R. D. Emery and G. L. Povirk, "Tensile behavior of free-standing gold films. Part II. Fine-grained films," *Acta Materialia*, vol. 51, pp. 2079-2087, 2003.

[15]   M. A. Haque and M. T. A. Saif, "Deformation mechanisms in free-standing nanoscale thin films: A quantitative in situ transmission electron microscope study," *PNAS*, vol. 101, pp. 6335- 6340, 2004.

[16]   A. J. Kalkman, A. H. Verbruggen, and G. C. A. M. Janssen, "Young's modulus measurements and grain boundary sliding in free-standing thin metal films," *Applied Physics Letters*, vol. 78, pp. 2673-2675, 2001.

[17]   A. H. Cottrell, *The Properties of Materials at High Rates of Strain*. London: Institute of Mechanical Engineering, 1957.

[18]   J. A. Venables, "Nucleation + Propagation of Deformation Twins," *Journal of Physics and Chemistry of Solids*, vol. 25, pp. 693-&, 1964.

[19]   E. O. Hall, "The Deformation And Ageing Of Mild Steel.3. Discussion Of Results," *Proceedings Of The Physical Society Of London Section B*, vol. 64, pp. 747, 1951.

[20]   N. J. Petch, "The Cleavage Strength Of Polycrystals," *Journal Of The Iron And Steel Institute*, vol. 174, pp. 25, 1953.

[21]   A. H. Chokshi, A. Rosen, J. Karch, and H. Gleiter, "On The Validity Of The Hall-Petch Relationship In Nanocrystalline Materials," *Scripta Metallurgica*, vol. 23, pp. 1679, 1989.

[22]   K. Lu, W. D. Wei, and J. T. Wang, "Microhardness And Fracture Properties Of Nanocrystalline Ni-P Alloy," *Scripta Metallurgica Et Materialia*, vol. 24, pp. 2319, 1990.

[23]   G. W. Nieman, J. R. Weertman, and R. W. Siegel, "Tensile-Strength And Creep-Properties Of Nanocrystalline Palladium," *Scripta Metallurgica Et Materialia*, vol. 24, pp. 145, 1990.

[24]   H. Chang, H. J. Hofler, C. J. Altstetter, and R. S. Averback, "Synthesis, Processing And Properties Of Nanophase Tial," *Scripta Metallurgica Et Materialia*, vol. 25, pp. 1161, 1991.

[25]   A. M. Elsherik, U. Erb, G. Palumbo, and K. T. Aust, "Deviations From Hall-Petch Behavior In As-Prepared Nanocrystalline Nickel," *Scripta Metallurgica Et Materialia*, vol. 27, pp. 1185, 1992.

[26]   J. R. Weertman, "Hall-Petch strengthening in nanocrystalline metals," *Materials Science & Engineering, A: Structural Materials: Properties, Microstructure and Processing*, vol. 166, pp. 161-167, 1993.

[27] J. C. M. Li, "Petch Relation And Grain Boundary Sources," *Transactions Of The Metallurgical Society Of Aime*, vol. 227, pp. 239, 1963.

[28] G. W. Nieman, J. R. Weertman, and R. W. Siegel, "Microhardness Of Nanocrystalline Palladium And Copper Produced By Inert-Gas Condensation," *Scripta Metallurgica*, vol. 23, pp. 2013, 1989.

[29] G. W. Nieman, J. R. Weertman, and R. W. Siegel, "Mechanical-Behavior Of Nanocrystalline Cu And Pd," *Journal Of Materials Research*, vol. 6, pp. 1012, 1991.

[30] D. L. Wang, Q. P. Kong, and J. P. Shui, "Creep Of Nanocrystalline Ni-P Alloy," *Scripta Metallurgica Et Materialia*, vol. 31, pp. 47, 1994.

[31] P. G. Sanders, G. E. Fougere, L. J. Thompson, J. A. Eastman, and J. R. Weertman, "Improvements in the synthesis and compaction of nanocrystalline materials," *Nanostructured Materials*, vol. 8, pp. 243, 1997.

[32] P. G. Sanders, C. J. Youngdahl, and J. R. Weertman, "The strength of nanocrystalline metals with and without flaws," *Materials Science & Engineering, A: Structural Materials: Properties, Microstructure and Processing*, vol. 234-236, pp. 77-82, 1997.

[33] W. D. Nix, "Mechanical-Properties of Thin-Films," *Metallurgical Transactions A: Physical Metallurgy and Materials Science*, vol. 20, pp. 2217-2245, 1989.

[34] J. E. Sanchez and E. Arzt, "Effects Of Grain-Orientation On Hillock Formation And Grain-Growth In Aluminum Films On Silicon Substrates," *Scripta Metallurgica Et Materialia*, vol. 27, pp. 285, 1992.

[35] R. Venkatraman and J. C. Bravman, "Separation Of Film Thickness And Grain-Boundary Strengthening Effects In Al Thin-Films On Si," *Journal Of Materials Research*, vol. 7, pp. 2040, 1992.

[36] C. V. Thompson, "The Yield Stress Of Polycrystalline Thin-Films," *Journal Of Materials Research*, vol. 8, pp. 237, 1993.

[37] C. V. Thompson and R. Carel, "Stress and grain growth in thin films," *Journal Of The Mechanics And Physics Of Solids*, vol. 44, pp. 657, 1996.

[38] H. J. Frost and M. F. Ashby, *Deformation mechanism maps*. New York: Pergamon Press, 1982.

[39] A. K. Mukherjee, J. E. Bird, and J. E. Dorn, "Experimental Correlations for High-temperature creep," *Trans. ASM*, vol. 62, pp. 155, 1969.

[40]   S. L. Robinson and O. D. Sherby, "Mechanical behavior of polycrystalline tungsten at elevated temperature," *Acta Metallurgica*, vol. 17, pp. 109, 1969.

[41]   E. W. Hart, "On The Role Of Dislocations In Bulk Diffusion," *Acta Metallurgica*, vol. 5, pp. 597, 1957.

[42]   R. L. Coble, "A Model for Boundary Diffusion Controlled Creep in Polycrystalline Materials," *Journal of Applied Physics*, vol. 34, pp. 1679-1682, 1963.

[43]   L. Lu, S. X. Li, and K. Lu, "An abnormal strain rate effect on tensile behavior in nanocrystalline copper," *Scripta Materialia*, vol. 45, pp. 1163-1169, 2001.

[44]   P. A. El-Deiry and R. P. Vinci, "Strain Rate Dependent Behavior of Pure Aluminum and Copper Micro-Wires," *Mater. Res. Soc. Sym. Proc.*, vol. 695, pp. L4.2.1, 2002.

[45]   I. Chasiotis, C. Bateson, K. Timpano, A. S. McCarty, N. S. Barker, and J. R. Stanec, "Strain rate effects on the mechanical behavior of nanocrystalline Au films," *Thin Solid Films*, vol. 515, pp. 3183, 2007.

[46]   S. Sakai, H. Tanimoto, and H. Mizubayashi, "Mechanical behavior of high-density nanocrystalline gold prepared by gas deposition method," *Acta Materialia*, vol. 47, pp. 211-217, 1998.

[47]   S. Sakai, H. Tanimoto, E. Kita, and H. Mizubayashi, "Characteristic creep behavior of nanocrystalline metals found for high-density gold," *Physical Review B*, vol. 66, 2002.

[48]   R. D. Emery and G. L. Povirk, "Tensile behavior of free-standing gold films. Part I. Coarse-grained films," *Acta Materialia*, vol. 51, pp. 2067-2078, 2003.

60

CHAPTER 3

EXPERIMENTAL METHODS

3.1 Sample Design and Fabrication

3.1.1 Sample pattern design

The sample geometry designed for the membrane deflection experiment was inspired by the testing bar used in the conventional tensile testing. The specimen geometry utilized in this study resembles the typical dog-bone tensile specimen but with an area of additional width in the center designed as the contact area where the line load is applied, as seen in Figure 3-1. This is desired to minimize stress concentrations where the loading device contacts the membrane. The suspended membranes are fixed to the wafer at either end such that they span the bottom view window. In the areas where the membrane is attached to the wafer and in the central contact area the width is varied in such a fashion to minimize boundary bending effects. These effects are also minimized through large specimen gauge lengths. Thus, a load applied in the center of the span results in direct stretching of the membranes in the areas of thin constant width in the same manner as in a direct tension test.
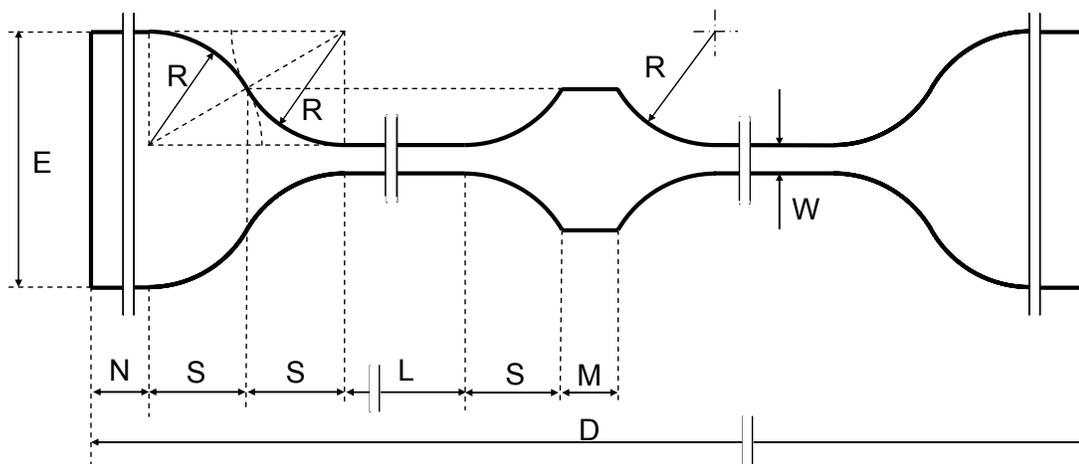
Figure 3-1 Schematic of the dog-bone shaped membrane geometry with all the parameters used to define specimen dimensions.
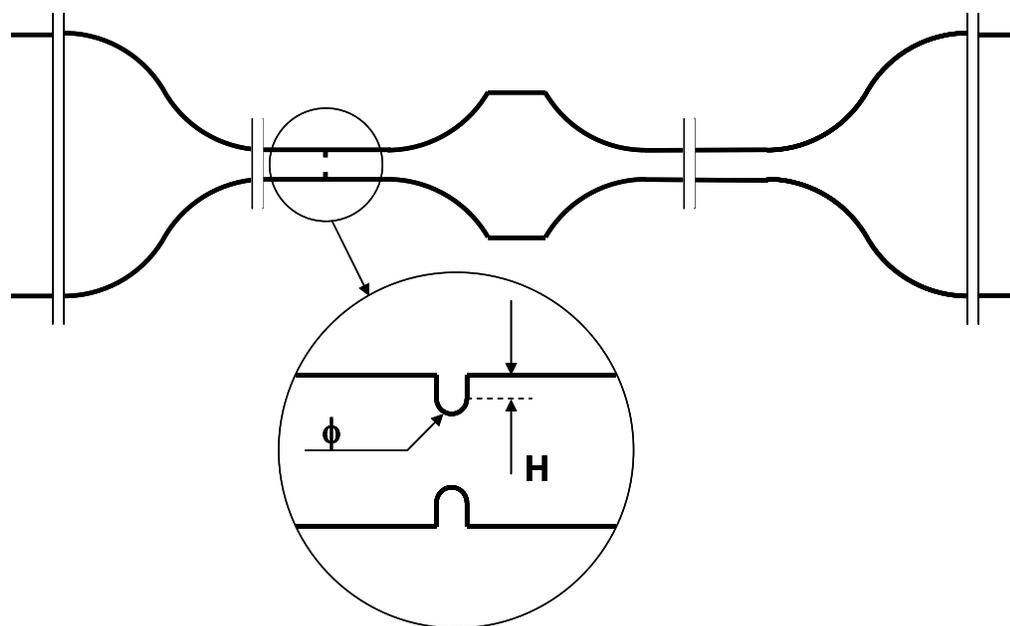
Figure 3-2 Schematic of the dog-bone shaped membrane specimen with desired notch at the gauge area.

Table 3.1 Membrane dimensions for different sized specimens in each die

Sample	Dimensions (μm)					
	W	L	D	E	R	N
Group a	1.25	25	287	11.25	5	100
Group b	2.50	50	362	22.50	10	100
Group c	5.00	100	514	45.00	20	100
Group d	10.00	200	818	90.00	40	100
Group e	20.00	400	1424	180.00	80	100
Group f	2.50	126	514	22.50	10	100
Group g	7.50	74	514	67.50	30	100
Group h	5.00	252	818	45.00	20	100
Group I	7.50	226	818	67.50	30	100
Group j	15.00	148	818	135.00	60	100
Group k	5.00	100	514	45.00	20	100
Group l	10.00	200	818	90.00	40	100
Group m	20.00	400	1424	180.00	80	100

There are two types of membranes, one is with a designed defect (an opened notch at the gauge area, as illustrated in Figure 3-2) and the other is without any defects. For the kind with defect, there are three groups of different sized membrane specimens, and for the kind without any defect, there are 10 groups of systematically altered dimensions for size effect investigation purpose. All the varieties of the samples are designed to be fabricated onto one 4 inch wafer. Figure 3-3 is a schematic drawing showing the pattern for a 4 inch wafer, consisting of 28 dies. In every one of them, a total of 13 groups of membranes with different dimensions and types are presented in each individual window named from Group (a) to Group (m), in each of them, 5 identical membranes are placed. Actual values for the dimensions of each group are listed in Table 3.1.
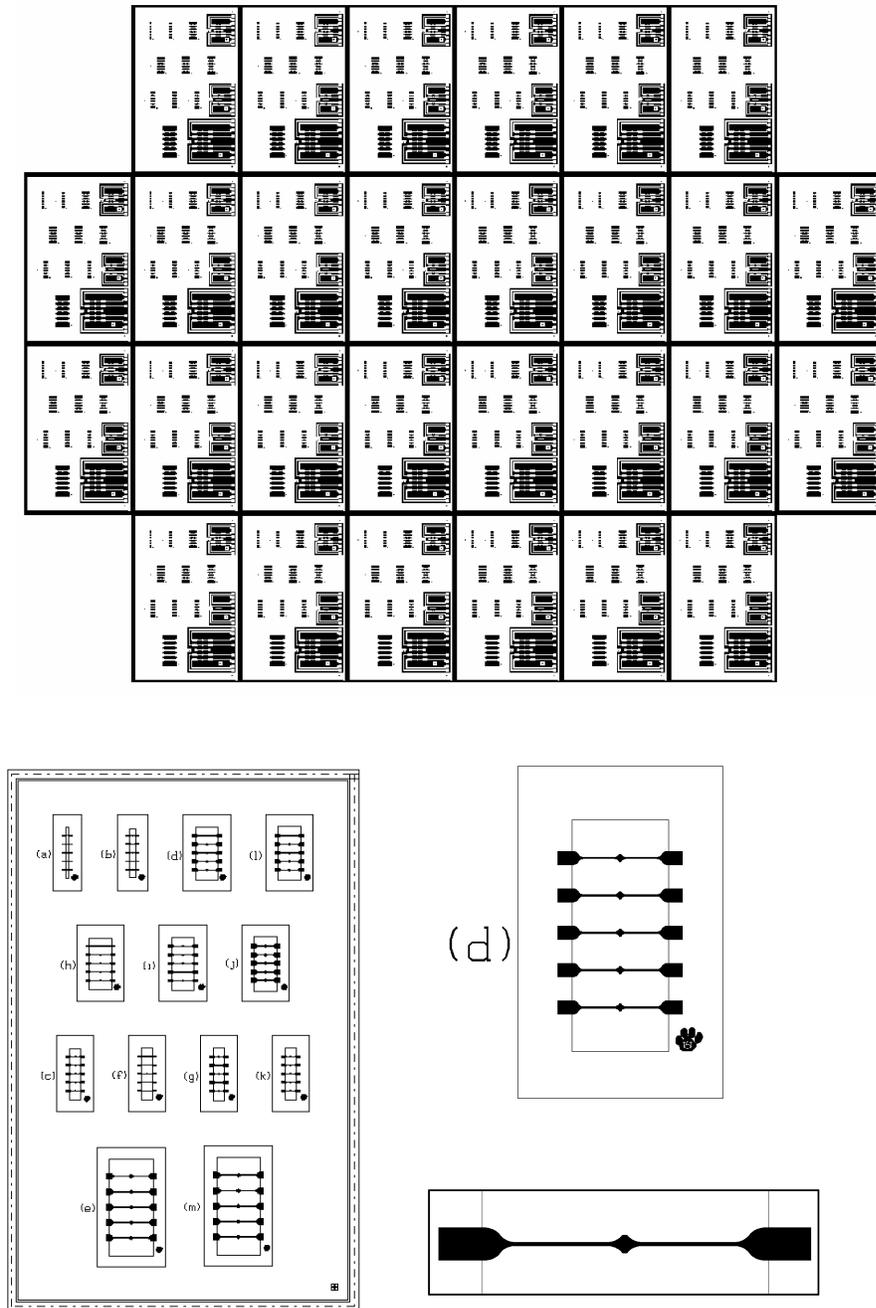
Figure 3-3 Schematic representations of the mask and the die layout of differently shaped group of membranes

3.1.2 Sample microstructure modulation

The microstructure of thin films strongly depends on the deposition process used. Characteristics such as grain size and shape, distribution, and crystallographic orientation are affected by the conditions under which grain nucleation, growth, coarsening, coalescence, and thickening occur [1, 2]. Two deposition techniques are used to modulate the microstructure of the gold thin films: E-Beam evaporation and sputtering. Figure 3-4 is the structure zone model (SZM) for thin film microstructure modulation in (a) E-Beam evaporation process and (b) sputtering process.
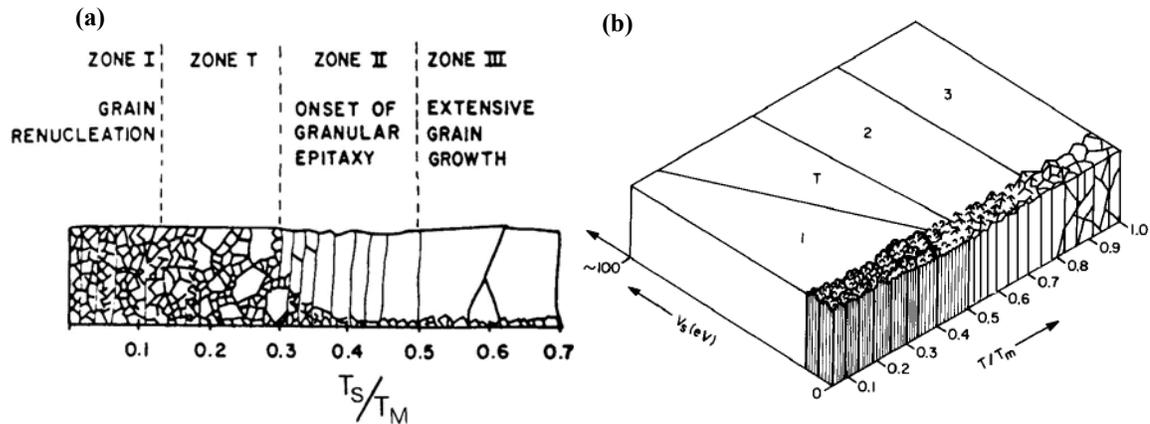
Figure 3-4 SZM for microstructure modulation by two deposition methods: (a) substrate temperature effect for evaporated film [3]. (b) Microstructure of RF-sputtered films showing effects of both substrate bias voltage and substrate temperature [4].

In evaporation the substrate is placed inside a vacuum chamber, in which a block (source) of the material to be deposited is also located. The source material is then heated to the point where it starts to boil and evaporate. The vacuum is required to allow the molecules to evaporate freely in the chamber, and they subsequently condense on all surfaces. This principle is the same for all the other evaporation technologies, only the

method used to the heat (evaporate) the source material differs. There are two popular evaporation technologies, which are E-beam evaporation and thermal evaporation. In E-beam evaporation, an electron beam is aimed at the source material causing local heating and evaporation. In thermal evaporation, a tungsten boat, containing the source material, is heated resistively with a high current to make the material evaporate. Many materials are restrictive in terms of what evaporation method can be used (i.e. aluminum is quite difficult to evaporate using resistive heating), which typically is related to the phase transition properties of that material. A schematic diagram of a typical E-beam evaporation system is shown in the Figure 3-5 (a).
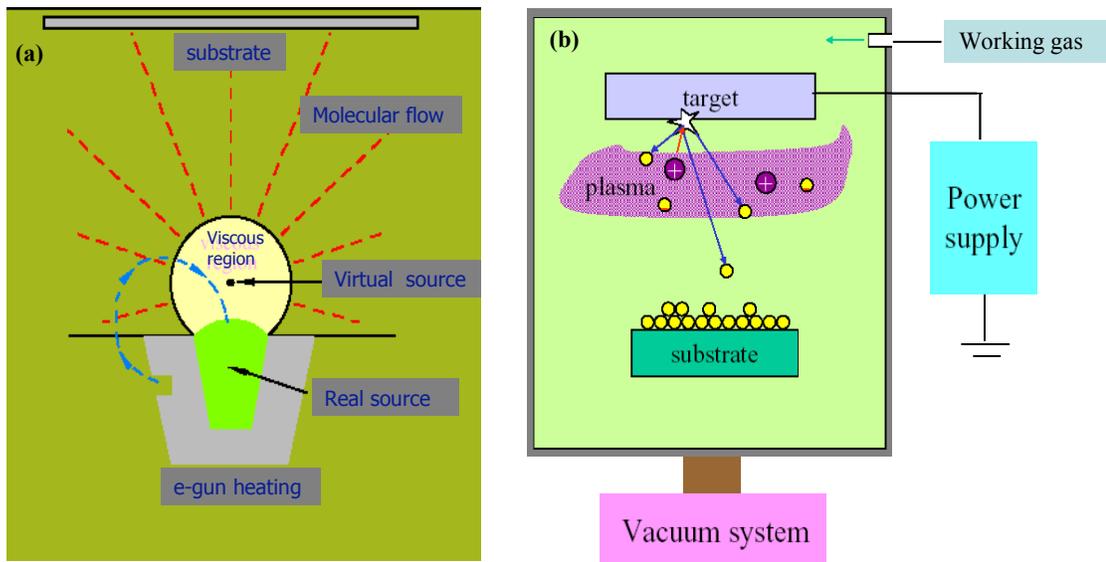
Figure 3-5 Schematic of (a) EBeam evaporation system and (b) Sputtering system.

Sputtering is a technology in which the material is released from the source at much lower temperatures than evaporation. The substrate is placed in a vacuum chamber with the source material, named a target, and an inert gas (such as argon) is introduced at low pressure. Gas plasma is created using an RF power source, which causes the gas to

become ionized. The ions are accelerated towards the surface of the target, causing atoms of the source material to break off from the target in vapor form and condense on substrate surface. Compared with evaporation, the basic principle of sputtering is the same for all sputtering technologies. The differences typically relate to the manor in which the ion bombardment of the target is realized. A schematic diagram of a typical RF sputtering system is shown in the Figure 3-5 (b).

3.1.3 Sample fabrication procedures

The sample fabrication procedures are generally follows the major processing steps in integrated circuit (IC) fabrication. The details of the complete procedure are described as following, as well as illustrated in the microfabrication flow presented in Figure 3-6. Some of the key issues related to the fabrication procedure were widely investigated experimentally and they are discussed in the text followed this outline.

Two masks as shown in Figure 3-7 were needed to fabricate the MDE specimens: the top mask as shown in Figure 3-7 (a) and the bottom mask as shown in Figure 3-7 (b). The top mask was used for the sample geometry patterning on one side of the wafer with film deposition; the bottom mask was used for the window opening in a KOH etching procedure. The dimensions of the different sized rectangular windows laid out on the mask were carefully calculated based on the relation of the bottom cavity plane width with the mask opening width in anisotropic etching of (100) silicon, as depicted in Figure 3-8.

67
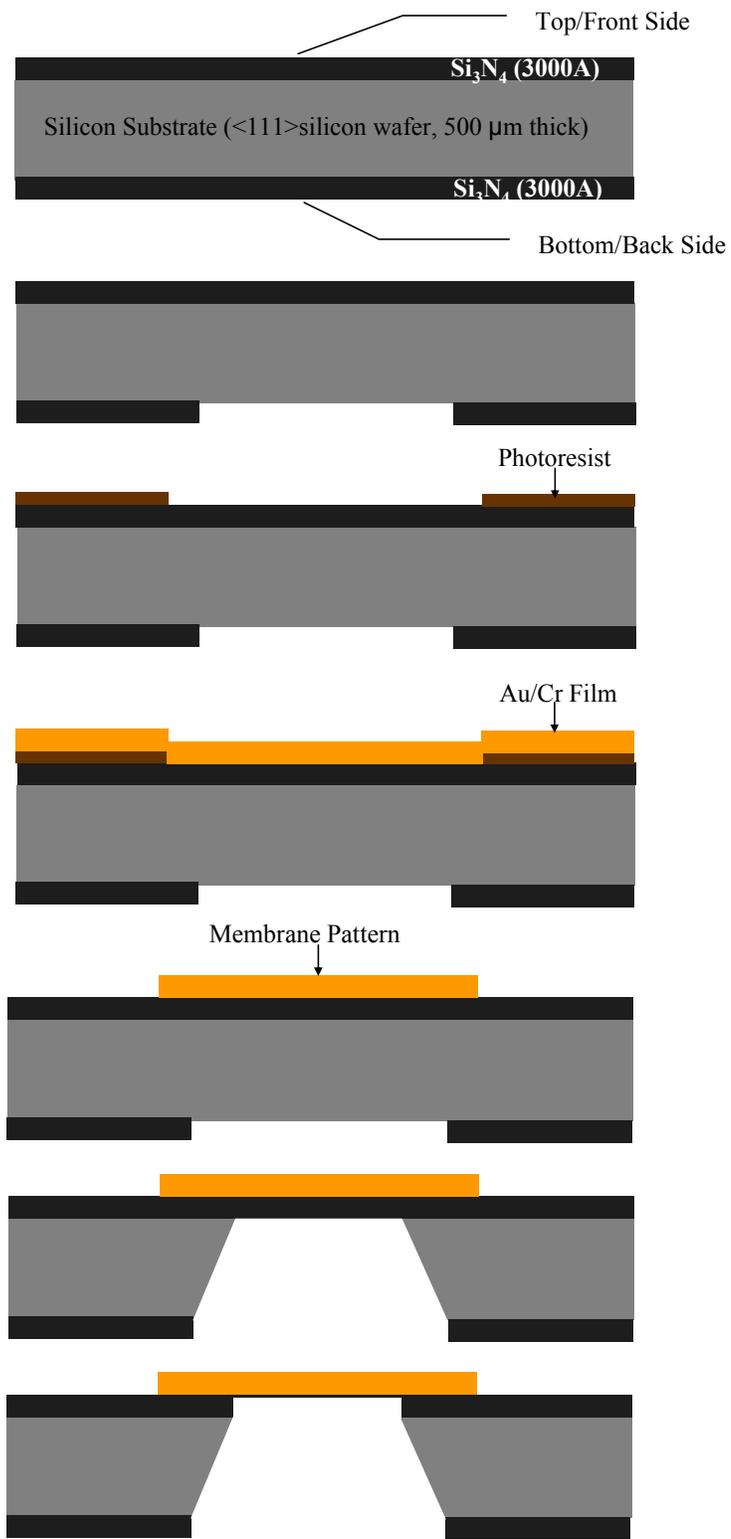
Figure 3-6 MDE Specimen fabrication process flow.
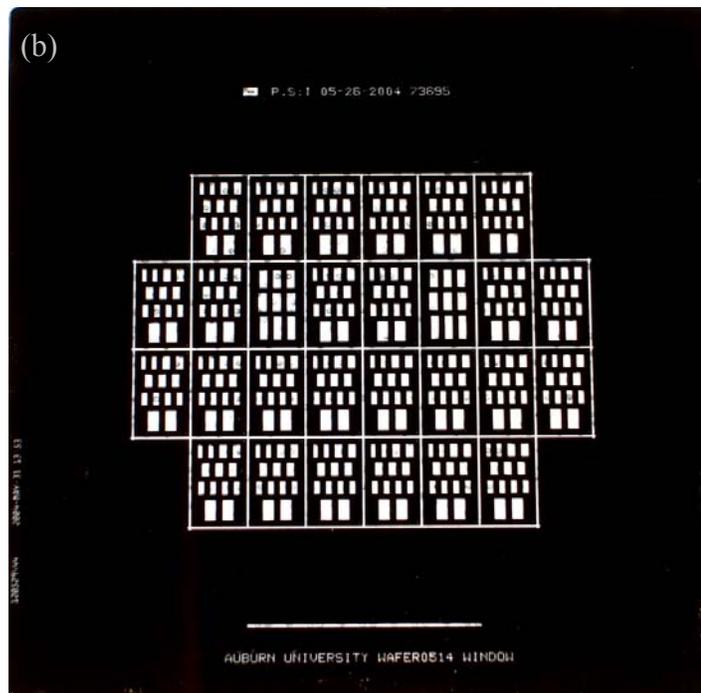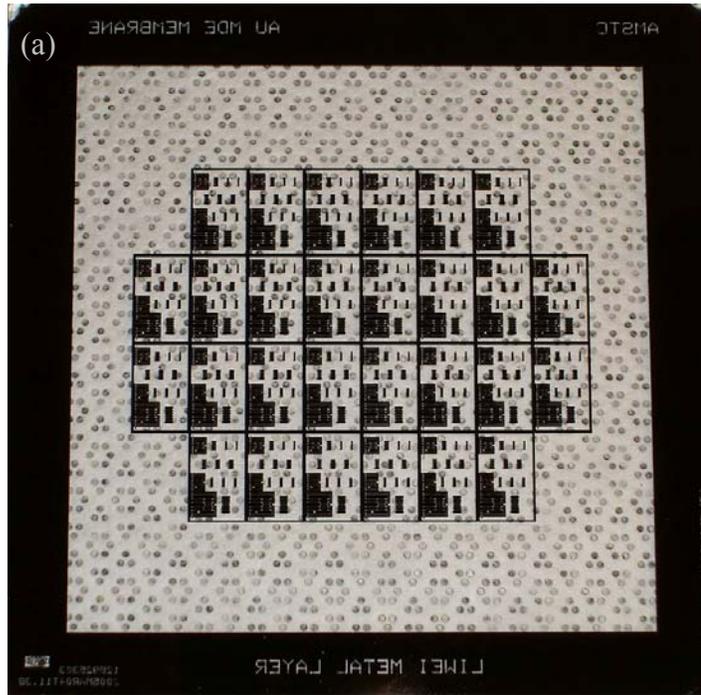
Figure 3-7 Images of the (a) top mask and (b) bottom mask.

1.   Starts with a double side polished 4 inch single crystal (100) silicon wafer, a layer of 300 nm thick low stress Si_3N_4 was deposited on both sides by LPCVD. The bottom side layer of Si_3N_4 was acted as KOH etching mask while the top side was used as the KOH etching stop. The top side of the wafer is defined to the side which film will be deposited and final MDE samples will be built, also referred as the front side. The bottom side is the side for the window opening, also referred as the back side. The silicon nitride deposition uses Diclorosilane ($SiCl_2H_2$) and Ammonia (NH_4) pressurized gas with a volume gas flow ratio of 5:1 at 850 ºC.

2.   Pattern the rectangular windows on the bottom side of the wafer with the bottom mask. The bottom windows were then opened by Matrix plasma etching, the bottom side of the wafer after Si_3N_4 etching is as seen in Figure 3-8 (a). 300 nm of Si_3N_4 can be etched in about 1 to 1.5 mins under the following etching conditions: pressure of 0.8 -1 mtorr; gas source of 40 % mass flow of O_2 and 40 % mass flow of NF_3, power of 200 W, and the temperature is about 100 ºC. During this plasma etching step, the front side layer of Si_3N_4 is protected by a layer of soft baked photoresist.

3.   Remove the protection layer of photoresist and clean, pre-bake, HDMS wafer before the top side patterning. Double side alignment is needed to pattern the top side of the wafer to assure the membranes would be suspended perfectly onto the opening window. About 1 μm thick of positive photoresist AZ5214 was spin coated onto the front side of wafer and patterned before any metal film deposition. Both E-beam evaporation and sputtering deposition are employed to grow the studied films; details of

the film deposition are given below. A layer of 20 nm of Ti or Cr should always be deposited prior to the metal film as an adhesion layer between films and substrate.

4.   The final pattern of membranes is obtained by lift off process, which require some soaking time in Acetone and some time of ultrasonic depending on the baking history and the thickness of the photoresist. For samples with thinner film thickness, a thinner layer of photoresist was applied correspondingly for the pattern and lift off process, and therefore, less time was needed to achieve a well defined pattern. Figure 3-8 (b) shows the front side of a wafer with the membranes patterned after lift off process.

5.   With a well patterned film layer on the front side, the wafer is then put into a customized Teflon wafer holder to protect the film surface during wet etching of Si. The solution was a mixture of 1350 ml of 45 wt% potassium hydroxide (KOH) solution, 880 ml of DI water and 335 ml of isopropanol. The etching temperature was 80°C and required nearly 10 hours to etch completely through the 500 μm thick silicon wafer.

6.   The remaining Si_3N_4 underneath the membranes (originally used as the KOH etching stop) was now dry etched away by plasma etching again. Although it is the same equipment employed and same thickness of Si_3N_4 layer, the etching recipe had to be altered due to the delicacy of the wafers now compared to what it was in step 2. Instead of etching away all the Si_3N_4 with a relatively high rate, this step must be taken in a more gentle manner as specified as the following recipe: pressure of 0.8 -1.0 mtorr; gas source of 20 % mass flow of O_2 and 40 % mass flow of NF_3, power of 130 W, and the temperature is about 70 ºC. To assure the Si_3N_4 was etched completely yet not over etched, it is experimentally found that applied the etching in a cyclic fashion yield better features than etched all the way through in single run.

71

7. Final release of the freestanding membranes by removing the titanium layer in a 5 wt % hydrogen fluoride acid solution.
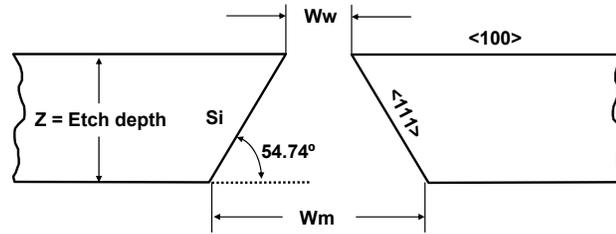
Figure 3-8 Relation of bottom mask opening width with top window opening width in anisotropic etching of (100) Silicon.
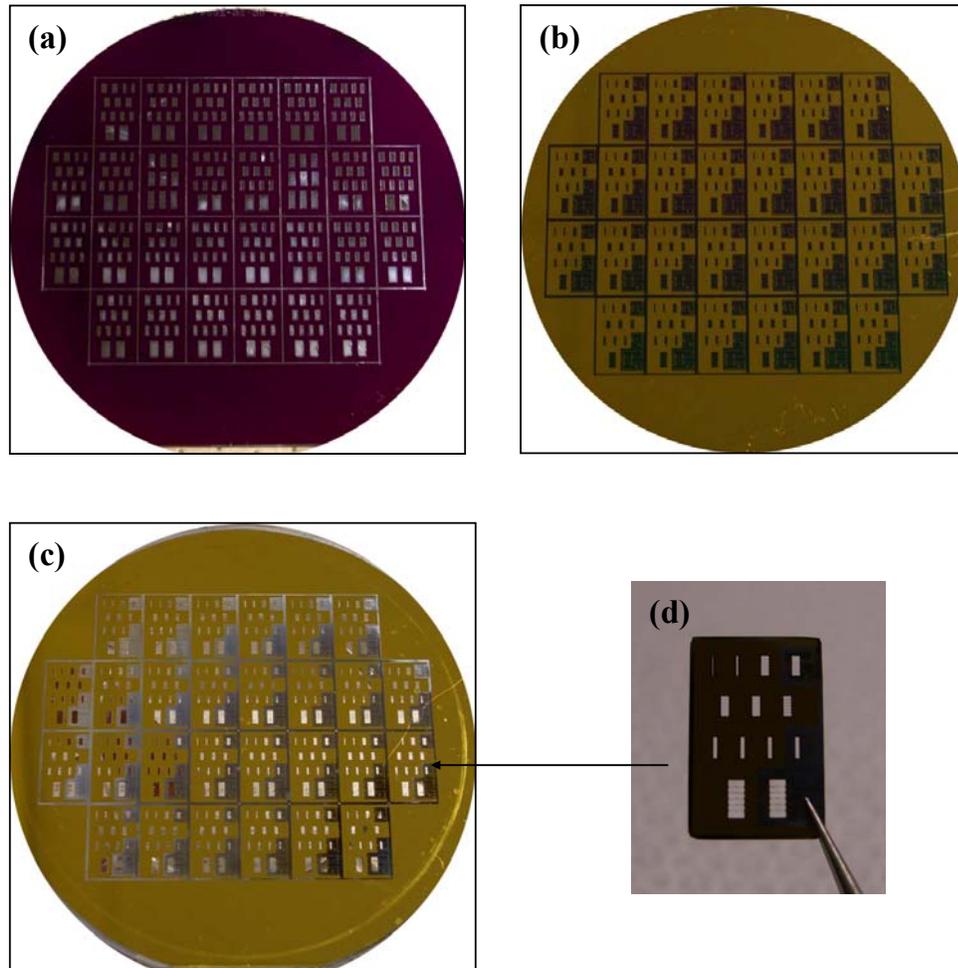
Figure 3-9 Images of (a) back side of the wafer after Si_3N_4 etching; (b) top side of the wafer with membrane patterns after lift off; (c) top side of the wafer after releasing the membranes by KOH etching; (d) an individual die separated from the fabricated wafer. (All the wafers used are 4 inch wafers)

Following the above procedure, a 4 inch wafer full of MDE freestanding membranes was produced, as shown in Figure 3-9 (c). The wafer then diced into individual dies by hand with the assistance of the existed trench etched during the KOH wet etching. One of the separated dies is shown in Figure 3-9 (d). It is worth mention that the wafer is at a very delicate state at this point, extreme care of handling in this

73

separation step was highly demanded to achieve the final success of yielding the perfect membrane samples ready to be tested in the membrane deflection experiments.

Most of the procedures listed above were carried out in a class 200 clean room facility located at the Electrical Engineering Lab Building in Auburn University. Only some of the film deposition (films deposited by sputtering method) and the KOH wet etching step were took place in another class 200 clean room located at the Materials Engineering Lab Building in Auburn University.

The silicon etching is one of the key and challenging steps in this fabrication procedure. Several commonly used silicon bulk micromachining technologies were studied and compared aim at producing the perfect opening window for the free standing membranes without contaminating the film surface to any extent. And those methods can be categorized as two classes: Isotropic dry etching and anisotropic wet etching.

Deep Reactive Ion Etching (DRIE), as a well-established dry etching representative, was first considered to be employed due to the easiness of achieving high etching rate (3.0 – 4.0 µm/min) and smooth surface. However, to prevent the contamination of the metal films to the STS Advanced Silicon Etcher chamber, the top side of the wafer had to be covered by a thick layer of photoresist during the etching, which caused the post etching problem: the photoresist used to protect the film surface had been heated slightly in the chamber and induced some uncertain polymerized reaction, as a result, the photoresist became very difficult to be removed completely afterward especially with the presence of those suspended membranes underneath them.

Anisotropic silicon wet etching is another mainstream technique for fabrication of various micromechanical devices because of their characteristic anisotropy, selectivity,

74

handling and process compatibility [5]. Many kinds of etchants have been proposed and most of them are hydroxide solution based. In our study, the most commonly used two chemical were examined: tetramethyl ammonium hydroxide (TMAH) and potassium hydroxide (KOH). The major problems for the hydroxide based wet etching are the difficulties of achieving a fairly high etching rate and a smooth silicon surface at the same time, furthermore, the etching solution would attack the metal films inevitably because it is often desirable to etch silicon substrate after metallization is completed. TMAH based etchant was employed as the first choice over KOH solution. The reasons are beside the fact that TMAH etching solution is able to achieve a high silicon etching rate and a smooth silicon surface, most importantly it can also provide a total protection of the exposed metal layer by adding a certain amount of silicon [6]. The TMAH etching solution used in this study consist of one part of 25 wt. % TMAH, two parts of DI water, and 1.4 wt. % of silicon powder. The temperature was set to 80 ºC, and kept adding 0.1 wt. % ammonium peroxodisulfate (APODS) to the solution every 20 minutes to absorb the hydrogen liberated in the reaction. With this etch recipe, an etch rate of 0.8 μm/min and a smooth silicon surface were realized. However, the exposed film surfaces were still attacked noticeably after nearly 10 hours of emersion in the solution even with an extremely low etching rate. At this point, the unsuccess of the above two methods lead to the only option left: KOH silicon etching solution.

The reason that KOH based solution was not the first choice from the beginning is because of its higher aggressiveness compared to the TMAH based solution, i.e. it is more difficult to find a good combination of concentration and temperature to achieve the perfect balance of the etch rate and silicon surface smoothness. Therefore, detailed

characterization of using KOH silicon etching solutions with various concentrations from 10 to 45 wt. % and temperatures from 60 to 90 ºC have been studied. Finally, the recipe consisting of 30 wt. % KOH solution, 13 vol. % - 15 vol. % isopropanol (IPA) and with temperature at 80 ºC yield the fairly high etching rate of 0.8 – 1.0 μm/min and smooth silicon surface. Furthermore, beside all the issues mentioned above, another key point in a long time and large volume etching operation is trying to keep the etching conditions as stable as possible; i.e., the gradient of the temperature and concentration distribution in the large volume of solution as well as the long time period are desired to be very steady.

Transene condensor

Teflon wafer holder

Heating circulator with stainless steel bath
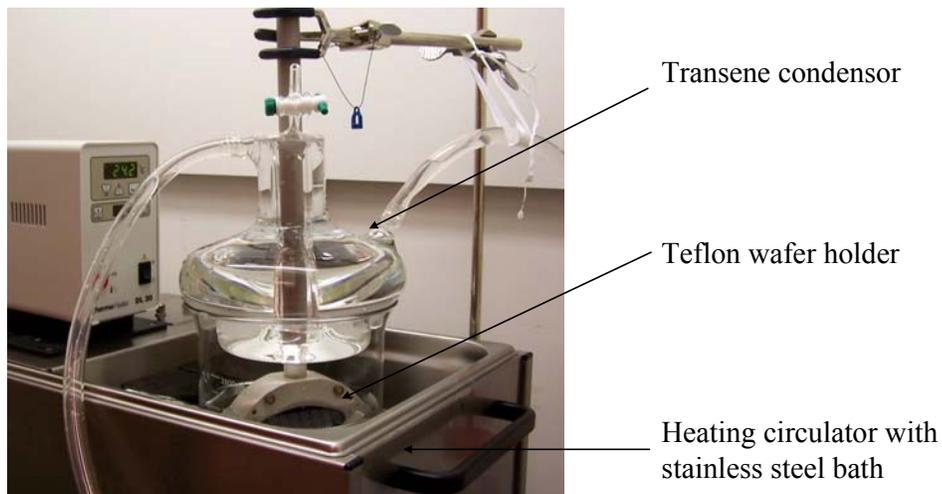
Figure 3-10 Image of the customized KOH Etching Station.

Inspired by these considerations, a specific customized KOH etching station was carefully designed and set up for this study to assure the etching conditions are well controlled. Figure 3-11 is a picture showing the KOH etching station. It consist of a customized Teflon wafer holder made by Advanced Micromachining Tool (AMMT); a 4L glass beaker; a custom made condensor with 25 mm tube diameter manufactured by

Transene; a heating circulator with stainless steel bath DL30-W26/B from Thermo Haake and a stirring hotplate from Fisher Scientific.

Firstly, the wafer was put into the holder body with the front side inward and back side outward, then the holder cover was placed on the exposed side of the wafer and tightened with 6 screws, there are three O-rings altogether assembled in between the body part and cover part of the holder in an effort to seal the protected side of the wafer reliably from the etchant, and also allows the minimum mechanical stress induced to the processed wafer, as seen in Figure 3-10, the holder provides a vented but untouchable space for the front side of the wafer, while expose the silicon area on the back side in the KOH etching solution.

Then the holder was immersed into the solution with care: instead of sitting the holder in the etchant bath, the holder was suspended in the bath because of the magnetic stir placed at the bottom of the beaker to improve the circulation of the large volume of liquid; and the top part i.e. the handle of the holder was designed long enough (32 cm) to be placed not only out of the 4 L beaker but even through the cavity tube opened at the center of glass condenser which is sitting on the top of the beaker to prevent the water evaporation induced concentration change. And the top end of the holder was eventually stabilized by a clip stand.

The heating element in this station is a heating circulator with stainless steel water bath, as seen in Figure 3-10, the whole beaker of solution was immersed into the bath and surrounded by heated water completely, and this greatly improved the temperature distribution uniformity in the solution compared to heating up by a hot plate. To further improve the circulation of the large volume solution and help removing the hydrogen

bubble from the etched silicon surface, a magnetic hot plate was sit underneath the heating bath to drive the magnetic stir placed in the bottom of the beaker. In a summary, this specific customized KOH etching station designed and built for this study assist the etching step in the fabrication process successfully attributed to the following advantages: the etching conditions including temperature and concentration are very well controlled from every aspect; the holder assured that the film was absolutely untouched by any surface or etchant.

Another challenging step in the fabrication process is the mask alignment. The structure of the MDE specimens requires the perfect alignment between the pattern on the front side of the wafer (the dog bone shaped metal membranes) and that on the back side (the rectangular opening windows). To accomplish this, particular care were needed and special alignment marks were added when the two masks were designed with LASI software. The physical outcome of any misalignment was that the final released membranes were not suspended on the opening window symmetrically. And there are two possible types of misalignment: translational and rotational. As a consequence, the deflection applied desirably at the center contact area of the membrane would not be able to induce a uniform tensile loading distribution along the length axis of the specimen. Therefore, to check the alignment after the completion of the test, before the MDE test is very necessary and was conducted with the assistance of SEM imaging.
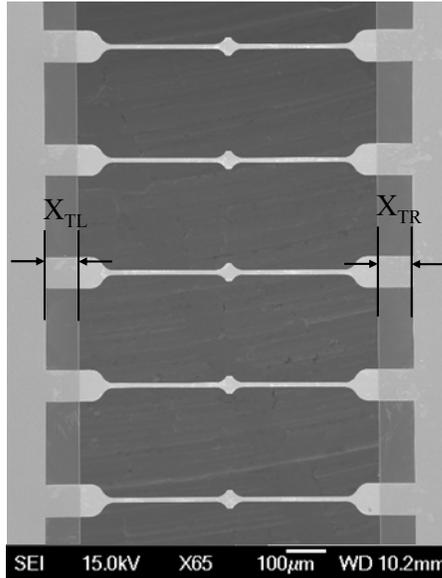
Figure 3-11 SEM image of one group of 5 identical membranes.

Figure 3-11 is an SEM image of one group of 5 identical membranes, the notations on the image helped to illustrate how the alignment is checked routinely for each to be tested membrane. Measure the distance from the one end of the dog bone shaped specimen to the edge of the opened silicon window for both sides (X_{TL} and X_{TR}), if X_{TL} is as same as X_{TR}, then there is no translational misalignment; the rotational misalignment is evaluated by measuring the angle between the edge of the window and the long axis of the membrane, and if it was measured as a 90 degree angle, then no rotational misalignment was created. However, it was very rare the case to get the samples with X_{TL} exactly equal to X_{TR}; and the edge of the window perfectly perpendicular to the long axis of the membrane exactly. Therefore, a slight misalignment was acceptable, after some experimental study about how the difference of testing results effected by the extent of the misalignment, it was ruled that samples which were aligned

79

within 2 % of the half length of the membrane (for example, if the half length of one membrane was measured as 250 µm, then the allowance would be 5µm) and 1° were considered qualified for the test.

3.1.4 Film Deposition

Films were prepared by two deposition methods: E-Beam evaporation and sputtering. By each deposition method, films with different thickness were produced. For E-Beam evaporation, films ranging in thickness from 0.25 µm to 1.0 µm; and for sputtering, it is from 0.25 µm to 1.5 µm. It is noteworthy to mention that all the films were deposited on to the substrate in a continuous fashion: even the interested thicknesses were designed to vary incrementally; each of the thicknesses was grown independently in one time run.

E-Beam depositions were conducted by a CHA Mark 50 E-Beam evaporation system located in the Electrical Engineering clean room. Up to 57 4-inch wafers can be loaded at once into this evaporation system. In our case, usually 6 to 10 wafers were loaded at each time. Because a thin layer of 20 nm thick titanium was always deposited as an adhesion promoter prior to gold film, two crucibles were engaged: crucible #1 contains the titanium while gold was put into crucible # 2. The titanium target was provided by the clean room facility. But the gold target was prepared and used only for this project and they are 0.25 inch by 0.50 inch gold pellets with purity of 99.999% purchased from KAMIS Inc. The base pressure was achieved at 2×10^{-7} torr and the deposition rate was controlled and maintained at about 4.0 Å/s for each run.

Sputtering depositions were carried out using a Denton Discovery 18 system installed in the Materials Engineering clean room. Only one wafer can be loaded each

time in this system. Similar to the E-Beam evaporation, an adhesion promoter prior to depositing gold without breaking the vacuum was also required. And this was realized by the two separate power guns equipped with the Denton discovery 18 system. The titanium layer was deposited by the RF gun with a RF sputter power density of 4.5w/cm^2, and the sputter rate for titanium was about 5 Å/s. The gold film was then deposited onto the top of the titanium by the DC gun with a DC sputter power density of 4.5w/cm^2, and the sputter rate for gold was about 10 Å/s to 12 Å/s. The titanium target was again provided by the clean room facility. And the gold target used for all the sputtered samples is 3 inch diameter by 0.25 inch thick gold disc with purity of 99.99% purchased from Electronic Space Products Inc. The base pressure was achieved at 1.0 x 10^{-6} torr or lower for each deposition. The argon gas flow rate was set at 25 sccm and the deposition pressure was controlled at 5 torr for all the sputtered films. Both titanium and gold targets were pre sputter cleaned for 3 minutes and 1 minute respectively with a covered shutter before each film deposition.

3.2 Sample geometry determination

The accurate determination of the dimensions of the samples is very important in this study due to their extensive and sensitive involvement in the data reduction part, which is the interpretation part of the stress and strain. The dimensions of the sample need to be determined carefully include the half length of the suspended membrane, the width of the gauge region and the membrane thickness. The thickness was controlled by the calculated deposition time based on the deposition rates, which were carefully characterized under each deposition condition prior to the real film deposition. And the

81

thickness was measured by a TENCOR alpha-step 200 profilometer. This step was carried out before the release of the membrane in the KOH etchant. And to achieve higher accuracy, the thicknesses were measured at many different spots (20-25 spots) distributed all over the whole area for each sample, and the average value was taken and used in the data reduction part. The half length and width of the suspended membrane were determined with the assistance of the measuring tool in the SEM equipment for every individual membrane instead of taking an averaged value. And this measurement was carried out after the release of the membrane, right before the tensile testing. Although the values of those two dimensions were set to a certain value when the masks were designed, there are always a slight change differed from the desired values due to the microfabrication issues, for instance, the half length of the freestanding membrane was related directly to the extent of the bottom window opening during the KOH etching, and this can be affected by the etching conditions, wafer thickness etc.

3.3 Membrane Deflection Experiment

3.3.1 MDE apparatus setup

The membrane deflection experiment set-up consists of an MTS Nanoindenter XP system equipped with a diamond wedge tip with length of 200 μm and width of 10 μm, to apply line load to the center of the membrane from the top. A Mirau microscope interferometer, with an integrated five axis manipulation stage and CCD camera, is positioned directly below the specimen to examine deflection through the micromachined window, as illustrated in Figure 3-12. Calibration and alignment between nanoindenter tip, freestanding membrane and Mirau objective were performed prior to testing to ensure

that the membrane was loaded at the center area and perpendicular to the plane of membrane. The Nanoindenter in the membrane deflection experiment set-up is aimed to apply a line load to the center of the membrane from the top, and to make sure the nanoindenter does so, a test flow has to be designed and programmed to control the nanoindenter to act in such a desired way.
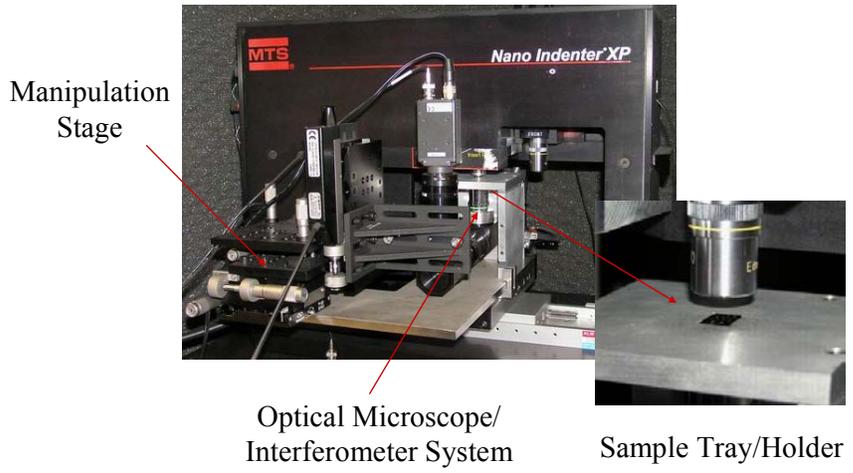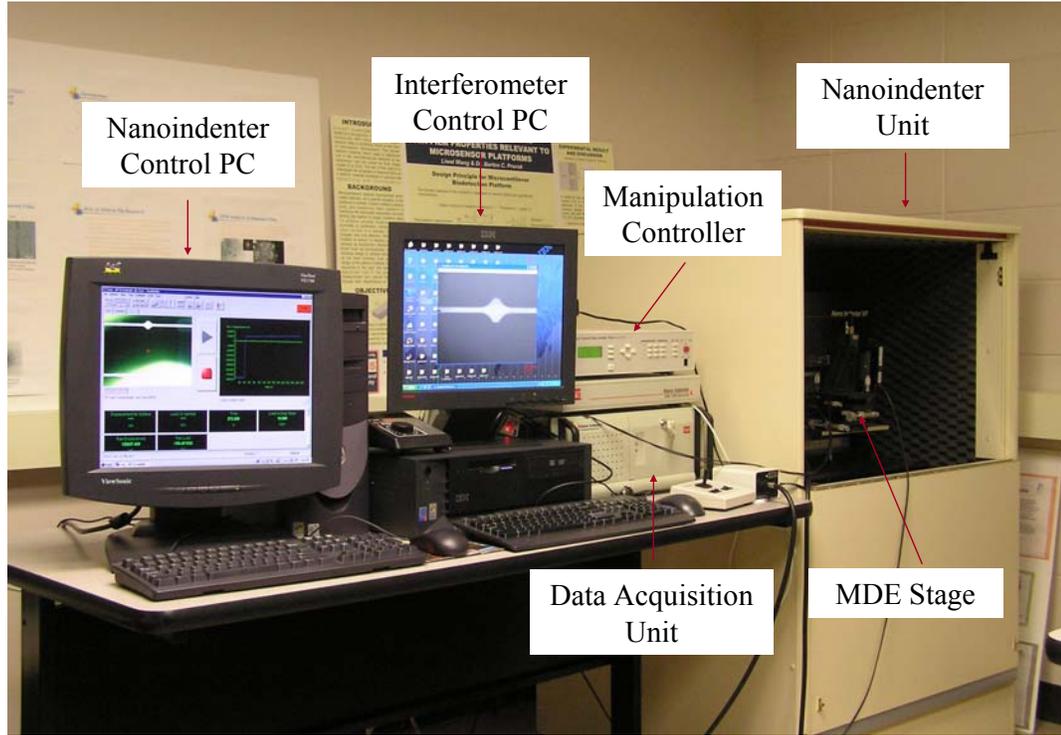
Figure 3-12 MDE set up showing the main components and detail testing configurations.

3.3.2 MDE testing procedure

The typical experimental procedure can be described in three steps:

- The first step is to locate and characterize the membrane geometry by means of the optical microscopy and interferometry. Once the dimensions and surface profile are stored, the sample die is moved to the Nanoindenter to begin the second step by means of an x-y translation stage with a positioning accuracy of less than 1μm.

- The second step is the membrane deflection experiment involved deflection of the membrane by the Nanoindenter. Parameters are set and the instrument performs a drift test. Once the test criterion is reached, the membrane is loaded. Simultaneously, the aligned interferometric station is focused on the back surface of the film. The camera is then set to acquire digital images within a desired period of time. Force and displacement data are stored in the Nanoindenter controller PC, and full field displacements are stored by acquiring monochromatic images. Prior to acquiring each set of images, the focus on the surface is updated to correct for the out-of-plane motion resulting from the downward displacement of the membrane.

- The third step of the experiment is data reduction. The data directly obtained from the MDE test must then be reduced to arrive at a stress-strain signature for the membrane. The load in the plane of the membrane is found as a component of the vertical Nanoindenter load. Therefore, using the measured distance between fringes, obtained from the interferometer, and load and deflection data, obtained from the Nanoindenter measurements, Cauchy stress and strain are independently computed [7, 8].

3.3.3 Stress calculation

The load data directly obtained from the nanoindenter must be converted to the load lying directly in the plane of the membrane, which is found as a component of the vertical nanoindenter load through the following equations:

$$P_M = \frac{P_V}{2 Sin\theta} \tag{3-1}$$

$$\tan\theta = \frac{\Delta}{L_M} \tag{3-2}$$

where θ is the angle of deflection, Δ is the displacement, L_M is the membrane half-length, P_M is the load in the plane of the membrane, and P_V is the load measured by the nanoindenter, see Figure 3-13. Once P_M is obtained, the stress, $\sigma(t)$, can be obtained from:

$$\sigma(t) = \frac{P_M}{A} \tag{3-3}$$

where A is the cross-sectional area of the membrane in the gauge region.
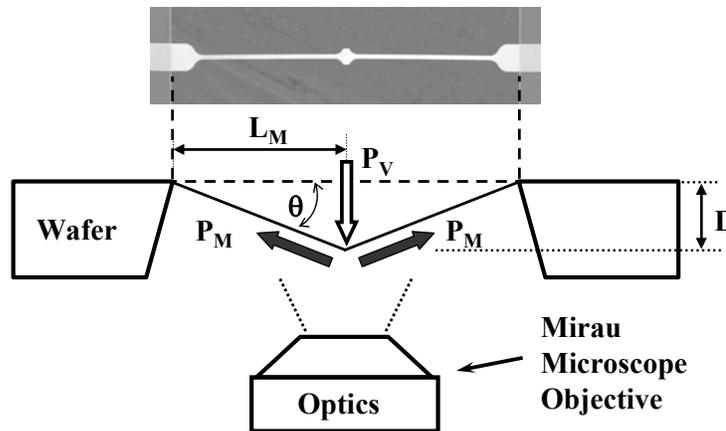
Figure 3-13 Schematic diagram illustrate the relationship between the applied vertical load and the load developed in the plane of the deflected membrane in the MDE test.

3.3.4 Strain measurement

As the membrane is deflected by the Nanoindenter, the interferometer, which works based on the Michelson Interferometer principle, records the membrane deflection by resolving surface fringes. The fringes are a result of phase differences of monochromatic light reflecting off the surface by traveling different path-lengths to and from the membrane. This light is recombined with a reference beam of fixed path length. When the path-length of the reflected light is a half of a wavelength, $\lambda/2$, out of phase with the reference beam they cancel each other resulting in a dark fringe. A fringe will occur at each $\lambda/2$ change in vertical height of the membrane.
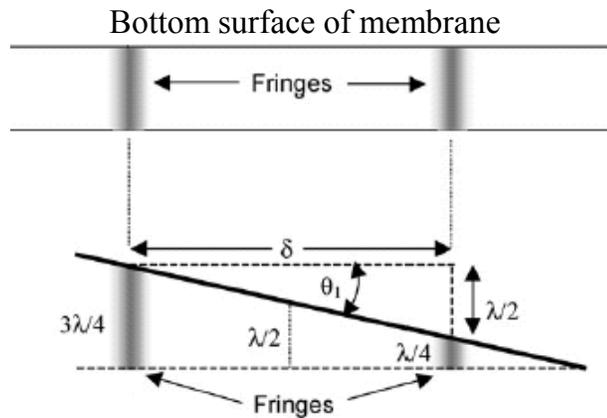
Figure 3-14 Schematic image showing the relationship between the distances between fringes (δ), wavelength of the monochromatic light used (λ), and vertical displacement.

Figure 3-14 shows a typical monochromatic image obtained and the corresponding relationship between deflection and the distance between fringes. The relationship for the distance between interference fringes, δ, and the vertical displacement is related through the wavelength, λ, of the monochromatic light. By finding the average

87

distance between the number of fringes that are in the focal plane of the interferometer, an overall strain, ε(t), for the membrane can be computed from the following relation:

$$\varepsilon(t) = \frac{\sqrt{\delta^2 + (\lambda/2)^2}}{\delta} - 1 \qquad (3\text{-}4)$$

where λ = 540 nm and is the wavelength of the monochromatic light used. Finally, stress-strain curves can then be generated based on this data. It should be noted that when testing specimens at this scale it is important to treat each membrane as an individual, being careful to measure film thickness and membrane dimensions of each rather than applying the same values across the board.

The strain of the deformed membrane used to be determined from the interpretation of the interferometer images that were acquired at periodic intervals for MDE testing. Complete details of that procedure can be found in [7, 8]. However, in the strain rate study part of this work, to achieve the desired variety range for the applied strain rate from 10^{-4} s^{-1} to 10^{-6} s^{-1}, the time required to accomplish each test is therefore extended from 10^2 s for the higher strain rate to 10^4 s for the lowest one, in which case, an enormously increased amount of work was demanded as to measure the average distance between fringes for every collected interferometer images.

Alternatively, the strain of the deformed membrane can be evaluated based on the geometric relation between the original half length and elongated half length of the membrane, as described in the following equation.

$$\varepsilon = \frac{\dfrac{L_M}{Cos\theta} - L_M}{L_M} = \frac{1}{Cos\theta} - 1 \qquad (3\text{-}5)$$

As illustrated in Figure 3-13, the angle θ can be obtained for each data point nanoindenter acquisition system provided. It is worth mentioning that although the strain is computed from the nanoindenter data directly, the interferometer is still critical to assisting pinpoint the exact moment of contact between the nanoindenter tip and membrane, as well as being able to observe the deformation progression of the membrane including the onset of shear localization and the membrane failure.

The strain rate is described by the following equation as a function of the membrane deflection at time t (Δ (t)) and the applied displacement rate (dΔ / dt).

$$\dot{\varepsilon} = \frac{d}{dt}\left(\frac{\Delta L(t)}{L_M}\right) = \frac{\Delta(t)}{L_M \sqrt{\Delta(t)^2 + L_M{}^2}}\left(\frac{d\Delta}{dt}\right) \tag{3-6}$$

From this relation, it is obvious that if the applied displacement rate is constant, the strain rate change continuously along with the membrane deflection. Therefore, the strain rate stated in this paper was defined as the experimentally applied strain rate, which corresponding at the onset of plasticity.

3.4 References

[1]   C. V. Thompson and R. Carel, "Grain growth and texture evolution in thin films," in *Grain Growth In Polycrystalline Materials II*, vol. 204-, *Materials Science Forum*, 1996, pp. 83.

[2]   C. V. Thompson, "Structure evolution during processing of polycrystalline films," *Annual Review of Materials Science*, vol. 30, pp. 159-190, 2000.

[3]   H. T. G. Hentzell, C. R. M. Grovenor, and D. A. Smith, "Grain-Structure Variation with Temperature for Evaporated Metal-Films," *Journal of Vacuum Science & Technology a-Vacuum Surfaces and Films*, vol. 2, pp. 218-219, 1984.

[4]   R. Messier, A. P. Giri, and R. A. Roy, "Revised Structure Zone Model For Thin-Film Physical Structure," *Journal Of Vacuum Science & Technology A-Vacuum Surfaces And Films*, vol. 2, pp. 500, 1984.

[5]   O. Tabata, R. Asahi, H. Funabashi, K. Shimaoka, and S. Sugiyama, "Anisotropic Etching Of Silicon In Tmah Solutions," *Sensors And Actuators A-Physical*, vol. 34, pp. 51, 1992.

[6]   G. Z. Yan, P. C. H. Chan, I. M. Hsing, R. K. Sharma, J. K. O. Sin, and Y. Y. Wang, "An improved TMAH Si-etching solution without attacking exposed aluminum," *Sensors And Actuators A-Physical*, vol. 89, pp. 135, 2001.

[7]   B. C. Prorok and H. D. Espinosa, "Effects of nanometer-thick passivation layers on the mechanical response of thin gold films," *Journal of Nanoscience and Nanotechnology*, vol. 2, pp. 427-433, 2002.

[8]   H. D. Espinosa, B. C. Prorok, and M. Fischer, "A methodology for determining mechanical properties of freestanding thin films and MEMS materials," *Journal of the Mechanics and Physics of Solids*, vol. 51, pp. 47-67, 2003.

CHAPTER 4

MICROSTRUCTURE OBSERVATIONS OF EVAPORATED AND

SPUTTERED FILMS

Obtaining a qualitative description of the microstructure of a material is often essential to develop an understanding of its macroscopic behavior. This chapter focuses on microstructural observations of as-deposited gold thin films in terms of surface topology, grain size, grain orientation and film texture. Since the microstructure of thin films strongly depend on the deposition process used, the gold films deposited by two deposition techniques: E-Beam evaporation and sputtering are characterized and compared systematically in this chapter.

4.1 Topography and Microstructures

The microstructures of the gold films were characterized using a JEOL JSM-7000F field-emission scanning electron microscope. The SEM micrographs were taken for films of different thickness deposited by both E-Beam evaporation and sputtering methods. All the images were taken with an accelerating voltage of 30 kV and a working distance around 10 mm. For each film sample, micrographs with two different magnifications were taken and displayed here, as seen in Figure 4-1 through Figure 4-6. The surface topology and grain distribution was intended to be depicted by the lower

magnification (50000X) images while the larger magnification (80000X) images were aimed at revealing the details of the grain size and shape.

The microstructures of all the deposited gold films were seen to vary as a function of thickness and somewhat as a function of deposition method. Uniform grain sizes of the gold films are clearly developed from each deposition process. An increase of grain size is observed as the film thickness increased for both processes, which may result from higher thermal energy induced and larger number of gold atoms available for aggregation for thicker films [1, 2]. The microstructure of the sputtered films appears to be better-developed than the E-Beam evaporated films regarding somewhat more equiaxed grains and better defined grain boundaries as well as slightly larger grain size, which are likely attributed to the inherently higher thermal and kinetic energy associated with sputtering process.

(a) t = 0.25 µm

Auburn   SEI   30.0kV   X50,000   100nm   WD 11.5mm

(b) t = 0.25 µm

Auburn   SEI   30.0kV   X80,000   100nm   WD 11.5mm
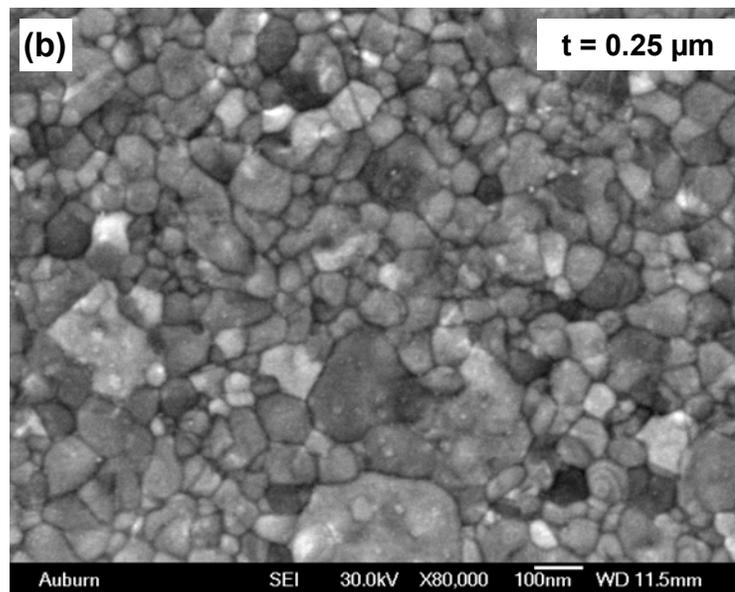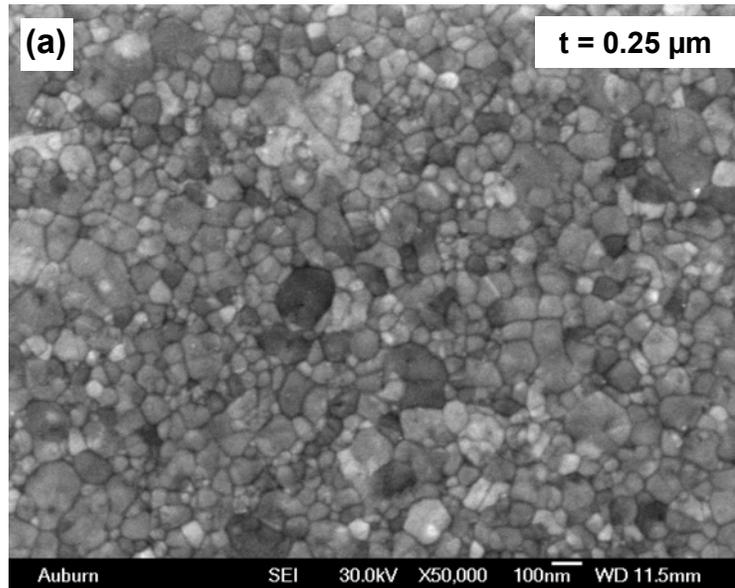
Figure 4-1 SEM micrographs of the EBeam evaporated film, 0.25 µm thick, showing (a) the grain distribution with magnification of X 50000 and (b) the grain structure detail with magnification of X 80000.
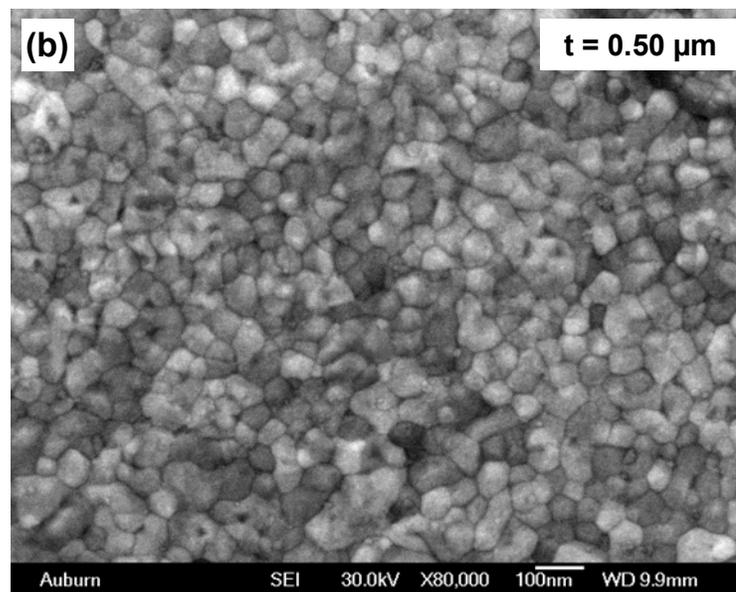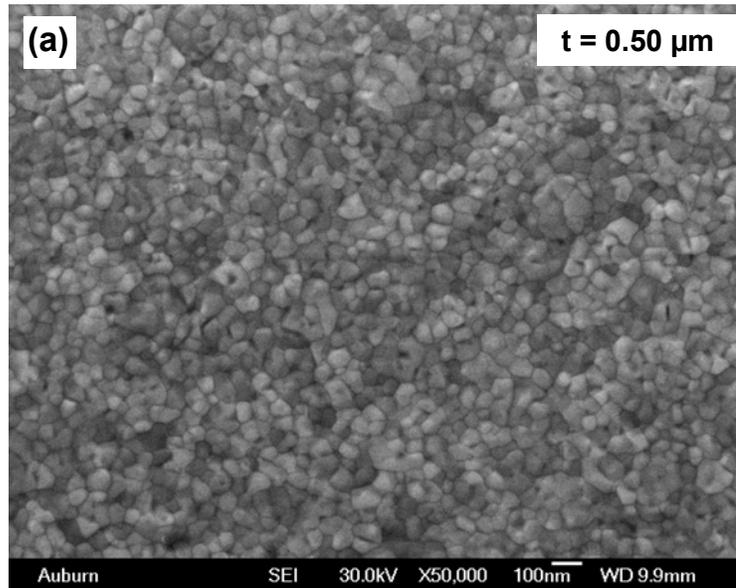
Figure 4-2 SEM micrographs of the EBeam evaporated film, 0.50 μm thick, showing (a) the grain distribution with magnification of X50000 and (b) the grain structure detail with magnification of X 80000.
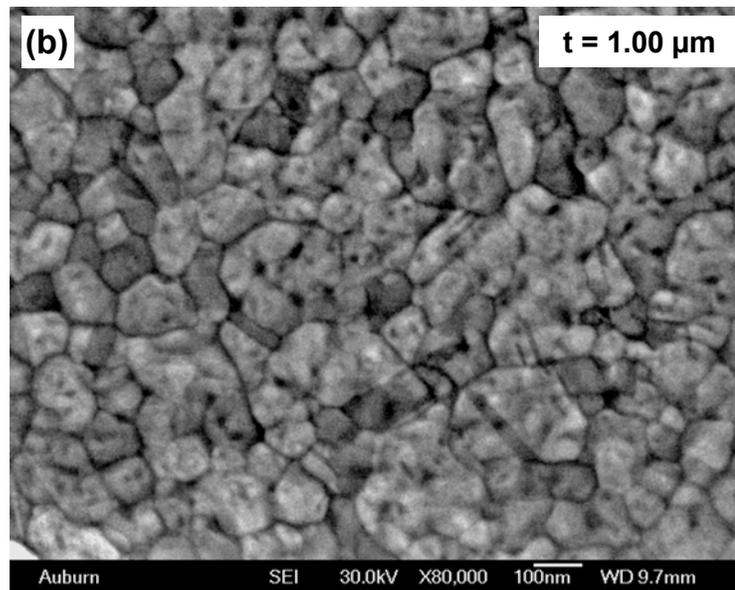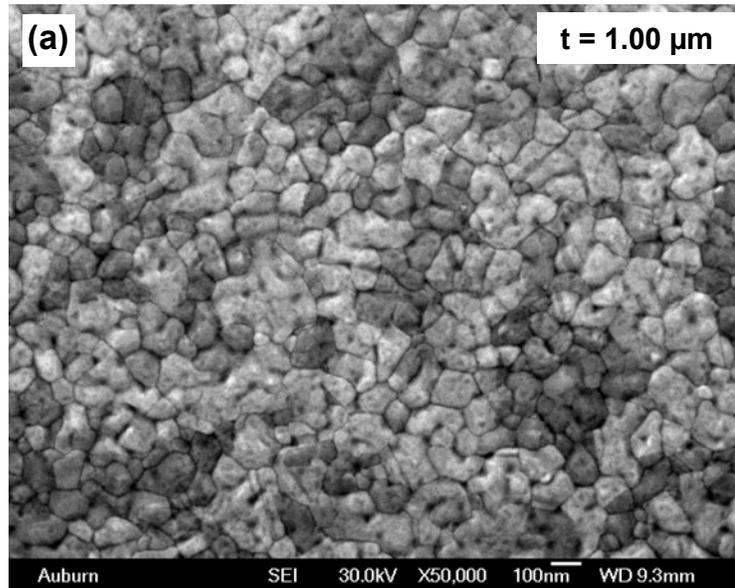
Figure 4-3 SEM micrographs of the EBeam evaporated film, 1.00 μm thick, showing (a) the grain distribution with magnification of X50000 and (b) the grain structure detail with magnification of X 80000.
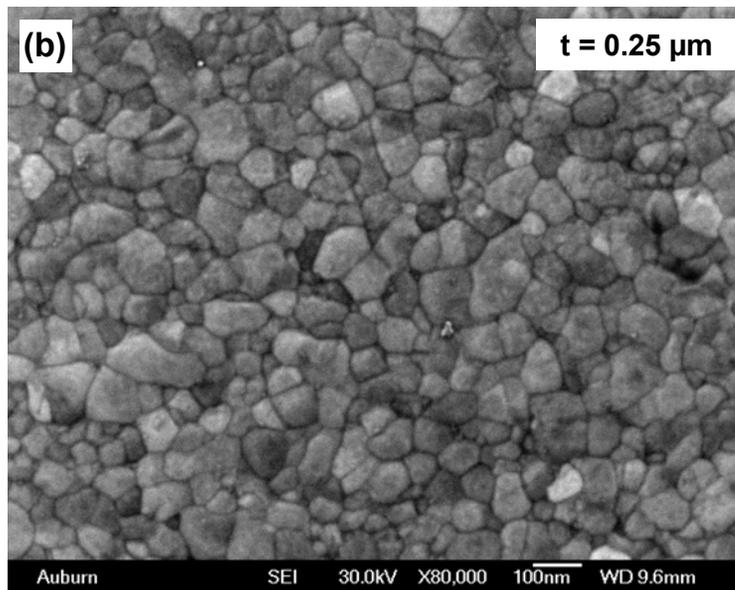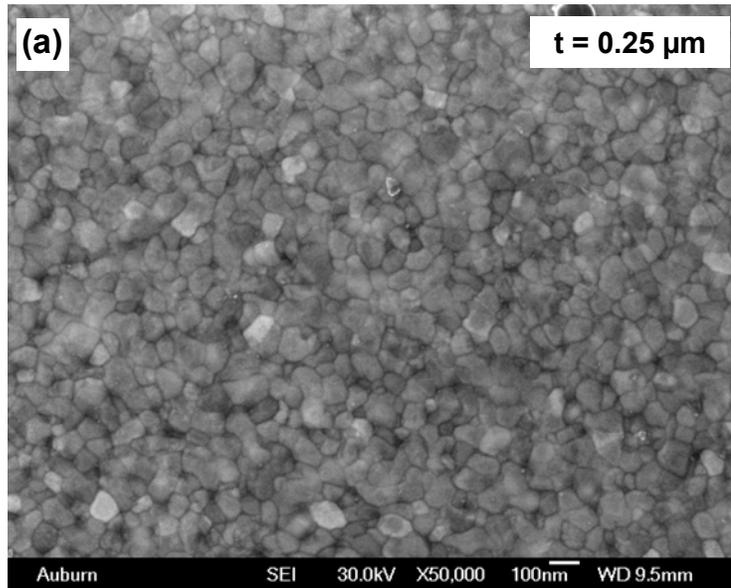
Figure 4-4 SEM micrographs of the sputtered film, 0.25 µm thick, showing (a) the grain distribution with magnification of X50000 and (b) the grain structure detail with magnification of X 80000.
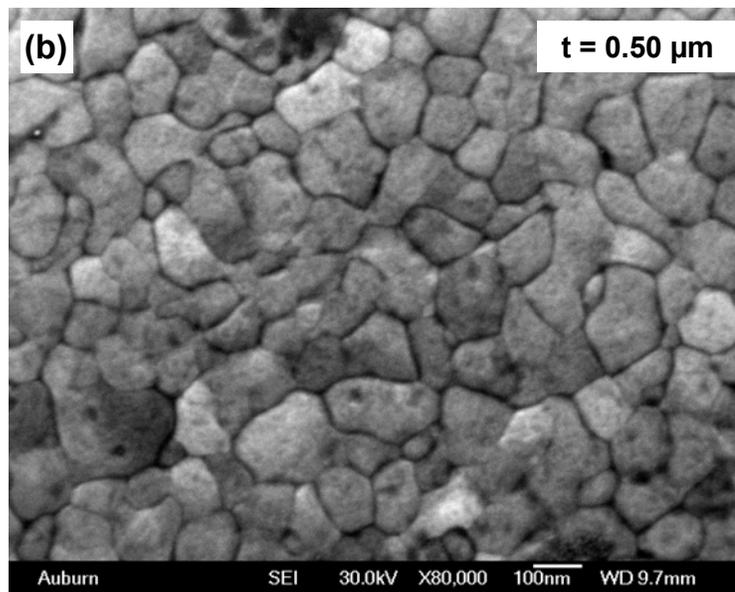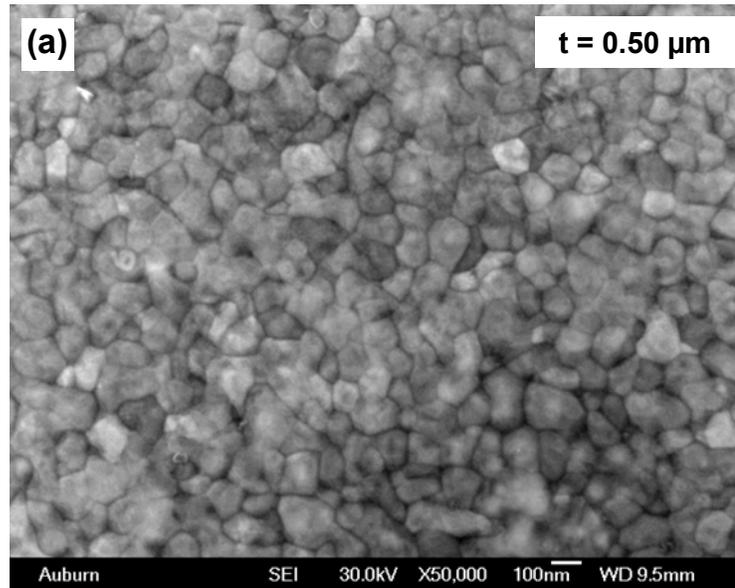
Figure 4-5 SEM micrographs of the sputtered film, 0.50 µm thick, showing (a) the grain distribution with magnification of X50000 and (b) the grain structure detail with magnification of X 80000.

(a) t = 1.00 µm

Auburn SEI 30.0kV X50,000 100nm WD 9.4mm

(b) t = 1.00 µm

Auburn SEI 30.0kV X80,000 100nm WD 9.4mm
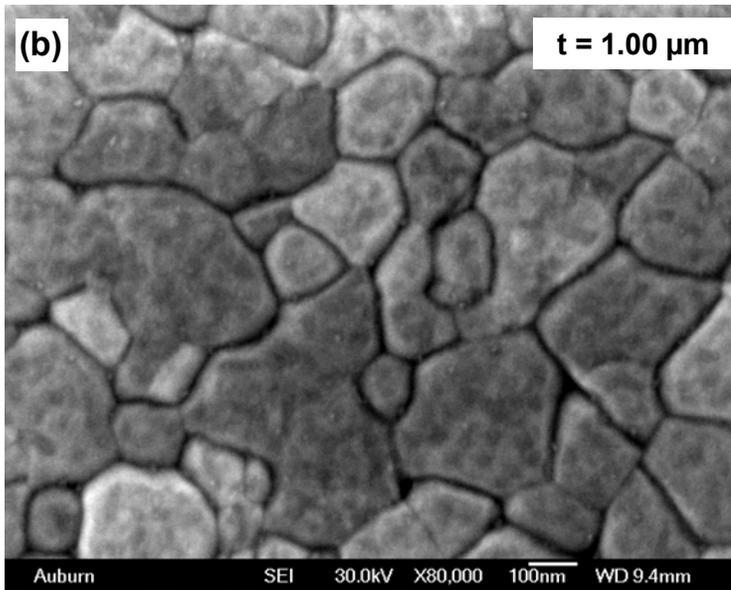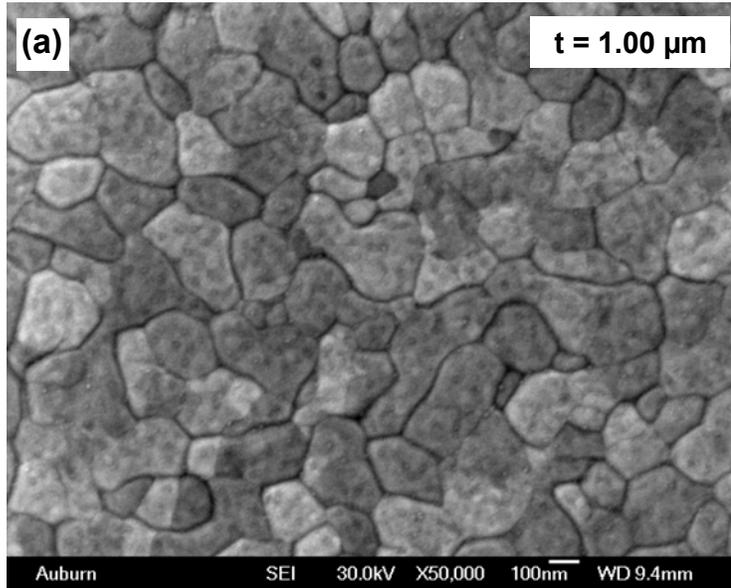
Figure 4-6 SEM micrographs of the sputtered film, 1.00 µm thick, showing (a) the grain distribution with magnification of X50000 and (b) the grain structure detail with magnification of X 80000.

4.2 Cross-Section Grain Structures

Besides the microstructure of the film surface, the cross-section microstructure through the film thickness was also characterized. Cross-sectioning is very essential to the microstructure property relationship analysis considering the information it can provide, such as grain structure and the number of grains across the specimen thickness. The cross-sectioning characterization in this study is completed with the assistance of the Focused Ion Beam (FIB) installed in a Nova 200 NanoLab Dual Beam (FIB-SEM) system. This part of the characterization was carried out at the FIB[2] center in Georgia Institute of Technology.
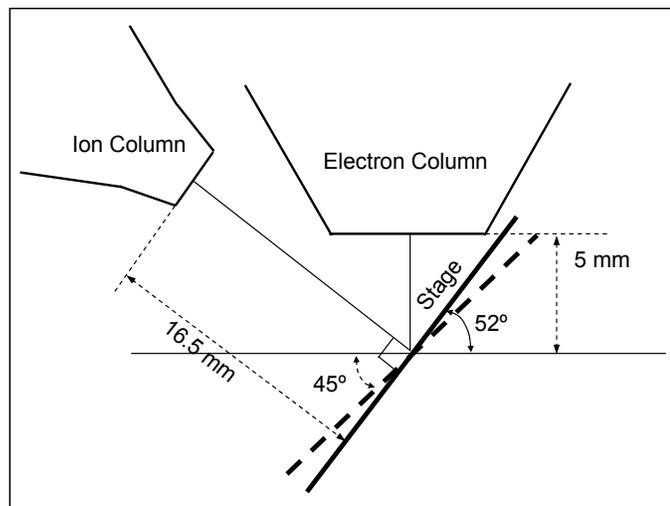
Figure 4-7 A typical dual-beam system configuration including a vertical SEM column and a tilted FIB column.

The dual beam incorporates both a focused ion beam (FIB) column and a scanning electron microscope (SEM) column in a single system. This combination is especially useful for cross-section sample preparation using the electron beam to view the cross-section face as the ion beam mills normal to the sample surface. SEM imaging

during the ion beam milling enables real-time monitoring of the milling process [3]. The typical dual-beam column configuration is a vertical electron column with a tilted ion column. Figure 4-7 shows such a configuration with the ion beam at 52° tilt to the vertical. In this case, the sample will be tilted to 52° for milling normal to the sample surface.

To obtaining the precision cross-sectioning characterization, firstly, the sample will be titled to 52° for ion milling normal to the sample surface, the films were milled by the focused ion beam with a beam voltage of 30 kV and an aperture of 400 pA to 1000pA depending on the film volume; then, the sample will be tilted to 45° to the vertical electron column for the SEM imaging with an electron beam voltage of 15 kV and a working distance of 5 mm.

The cross-section images of all the free-standing gold film samples are illustrated in Figure 4-8 through 4-10. In each figure, the cross-section grain structures of films with same thickness but deposited by different technique are displayed comparatively.

These figures show that a limited number of grains or even a single grain presented through the film thickness. And there is slight difference in the film structure presented in these two films.
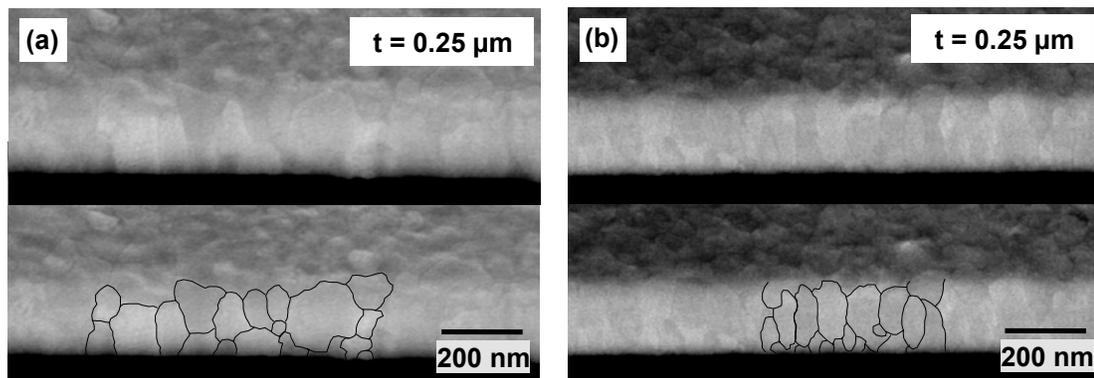
Figure 4-8 SEM micrographs of the cross-section of (a) 0.25 μm thick EBeam evaporated film and (b) 0.25 μm thick sputtered film.

100
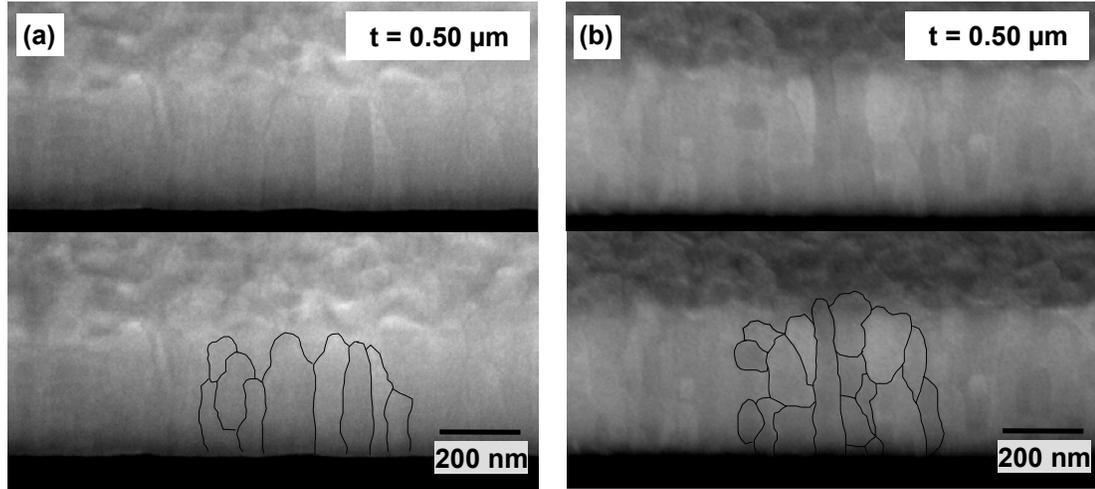
Figure 4-9 SEM micrographs of the cross-section of (a) 0.50 µm thick EBeam evaporated film and (b) 0.50 µm thick sputtered film.
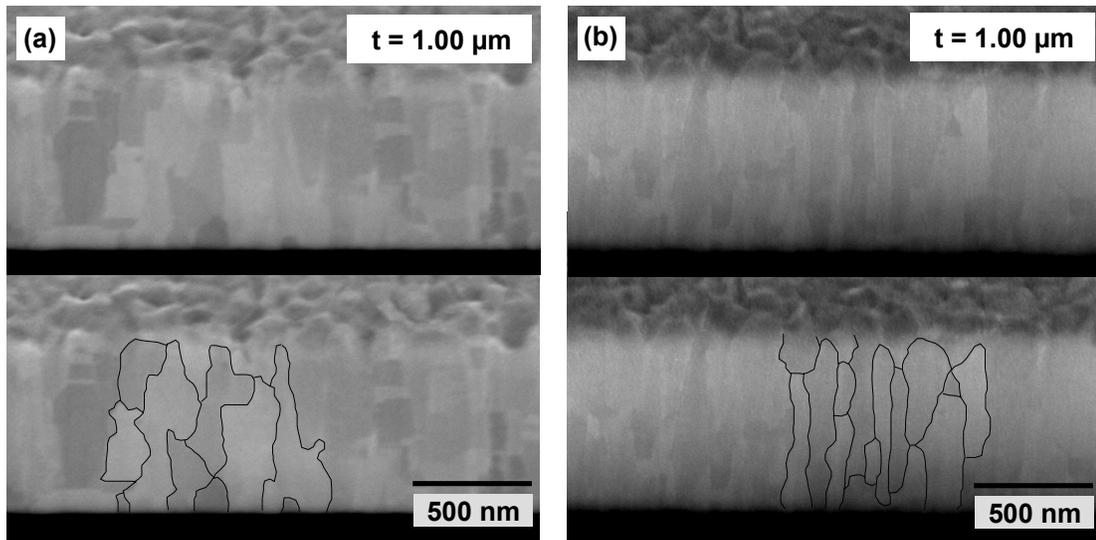
Figure 4-10 SEM micrographs of the cross-section of (a) 1.00 µm thick EBeam evaporated film and (b) 1.00 µm thick sputtered film.

4.3 Quantitative Grain Size Measurement

Two different ways of quantitatively evaluating the grain size were approached in this study. One is conducted manually with the assistance of the scanning electron microscopy (SEM) images, using the well established mean lineal intercept method described as ASTM Standard E 112-96 [4]. The procedure of this method can be outlined briefly as following: 1. take a SEM image with certain magnification; 2. draw a test line across the field of the image, the length of a single test line and the magnification should be such that as many intercepts as possible can be counted; 3. count the intercepts (an intercept is the segment of the test line which overlays one grain). To obtain more reliable and accurate data, some measurement strategies are followed for each measurement: (a) Make counts on 3 to 5 randomly selected images; (b) Use 3 or more orientations of the test line for each image; (c) Chose 2 different magnification for each sample. As a result, a reasonable average grain size and a desired statistic for each specimen can be reported by this method.

As a check on the measurements made above, grain sizes were also determined by interpreting the electron backscattered diffraction (EBSD) data. The physical principle of how to collecting the EBSD data is given in detail in the following section 4.4.1. Two methods to access the grain size measurement are available in the EBSD data analysis software Tango. One is the line intercept measurement just like we introduced above, a major difference between this software implementation and the manually conventional one is that the crystallographic orientation data is being used rather than a processed image from a specimen. The other is grain area determination. Compared to manually

measure the grain size on the images collected by the scanning electron microscopy, the advantage of EBSD data is that there is no ambiguity about the grain boundaries since they are measured in terms of crystallographic data rather than a processed scanning electron microscopic image.

Table 4.1: The grain size values measured by ASTM Standard E 112-96 Method and EBSD Grain Size Analysis method.

Sample	ASTM Standard E 112-96 Method			EBSD Grain Size Analysis		
	Ave Grain Size (nm)	Grains (#)	STD (nm)	Ave Grain Size (nm)	Grains (#)	STD (nm)
E250	52.97	573	2.18	30.06	745	13.87
E500	53.56	576	2.92	45.45	592	17.14
E1000	107.38	325	7.75	102.23	346	15.63
S250	61.41	530	4.19	54.36	806	15.45
S500	117.32	281	10.24	108.98	429	19.67
S850	182.64	191	11.55	169.25	362	23.36
S1000	218.62	159	13.55	206.83	309	21.36
S1500	327.26	197	11.33	310.86	265	28.65

The resulting grain sizes for each sample are summarized in table 4.1. Both the manually estimation guided by ASTM Standard E112-96 and the automated measurement conducted by EBSD are displayed in table x with the average grain size, number of grains, and standard deviation. And the results agreed well with the quantitative observation from the SEM micrographs: the median grain size increases with film thickness; the sputtered films possessed a slightly larger grain size compared to the E-Beam evaporated films.

4.4 Grain Orientation and Film Texture

Grain orientation and texture sometimes can be important to the mechanical properties of bulk polycrystalline materials depending on the extent of the preferred orientation or texture resulted from all the individual grains that comprise the material as elastic and plastic properties of crystals depend on the crystallographic orientation [1, 5, 6]. But most of other cases, the grains in polycrystalline materials are more likely to become randomly orientated and results in no preferred orientation and strong texture because of the large ratio of the volume to grain boundary. However, it is the opposite for thin films in term of limited number of grains available across the thickness; much smaller ratio of volume to grain boundary and volume to the surface compared to the bulk materials, which make the polycrystalline metallic thin films are often highly textured with grain typically aligned so as to minimize the surface energy of the system. Therefore, grain orientation and texture measurement are always very critical for evaluating the mechanical properties of thin films.

4.4.1 Introduction to EBSD

Traditional techniques for measuring texture in bulk metals by x-rays are not very effective in the case of thin films. This is mainly because the penetration depth of the interrogating beam can be on the same order of magnitude as the film thickness depending on the angle of incidence of the beam. Although recent study on developing new techniques utilizing x-rays to measure the texture particularly for thin films have shown the possibility and gained its popularity in this field, accessing the individual grain orientation information is still a big challenge step for x-rays [7-9]. Another option for more accurately measuring the grain orientation and texture of thin films was to use

electron backscattered diffraction (EBSD) technique. The primary advantage of this method is that accelerated electrons penetrate a small depth below the surface, on the order of several hundred angstroms, so that the texture on the front and back sides of a film could be quantitatively determined.

The formation of an EBSP can be described as follows: (1) The electrons strike the specimen, and within the pattern source point they are inelastically scattered, losing ~1% of their energy – this produces a little line broadening. (2) These scattering events generate electrons traveling in all conceivable directions in a small volume which is effectively a point source. (3) Electrons that satisfy the Bragg diffraction condition for a particular plane are channeled differently to the other electrons- thus producing a change in intensity. (4) For each crystallographic plane, these electrons form two cones that intersect the imaging plane (phosphor screen) as hyperbolae. These are the Kikuchi lines construct the EBSP at that certain location of the sample. The resulting EBSP is then automatically collected, indexed and analyzed.

4.4.2 EBSD Set up and Experiments

The CHANNEL 5 EBSD system from HKL used in this study was attached to a JEOL JSM-7000F SEM instrument equipped with a field emission gun. The principal components of this EBSD system are schematically shown in Figure 4-11. and listed as follows:

- A sample tilted at 70° from the horizontal.
- A phosphor screen which is fluoresced by electrons from the sample to form the diffraction pattern.

- A sensitive charge coupled device (CCD) video camera for viewing the diffraction pattern on the phosphor screen. The camera is connected to a computer with a frame grabber which captures the EBSP image.

- A computer that runs EBSD experiment; communicates with the SEM; receive images from the EBSD detector; analyze the diffraction pattern and display the results.
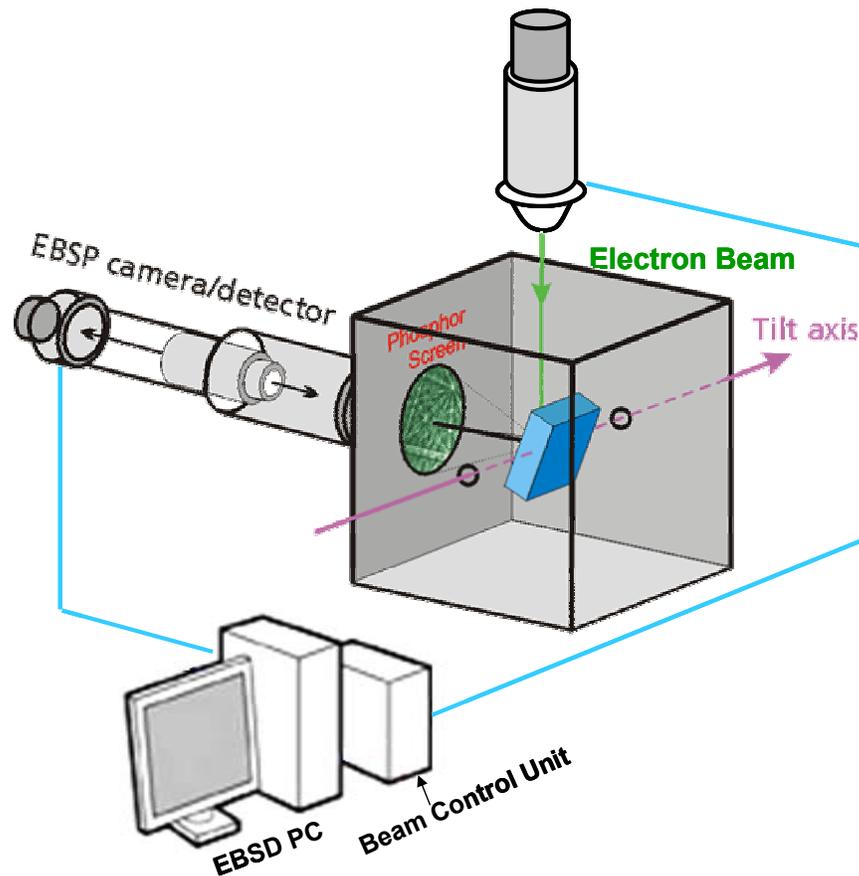
Figure 4-11 Schematic of the principal components in an EBSD system.

To produce an optimum EBSP signal, the specimen has to be highly titled, usually at 70° from the horizontal to increase the amount of electrons which can reach the detector and also optimize the contrast in the diffraction pattern. For smaller tilt angles the contrast in the diffraction pattern decreases. A customized sample stub holder with a

70º wedge was made to meet this tilt requirement. The EBSD detector unit in our system called "Nordlys" uses the latest digital imaging technology to produce high quality EBSPs. It consists of a rectangular phosphor screen which is matched to the size of the CCD and a high resolution digital CCD camera with motorized insertion and pixel binning. The insertion/retraction movement of the "Nordlys" detector is controlled by a digital handset. The Flamenco software is used to automatically analyze the EBSP and control the SEM beam and stage scanning. Other software in CHANNEL 5 like Tango, Mambo etc. are used to post processing the analyzing the EBSP data.

Because in EBSD, the diffracted electrons escape from within a very thin layer (only a few tens of nanometers) of the specimen surface, the specimen needs to be well prepared and relatively free of surface damage. Most of the samples in this study possessed a fairly smooth surface attributed to the mild film deposition condition employed. However, some of the sample presented a relatively rough surface which might caused during the fabrication process, in such a case, the following solution was used for cleaning the gold surface: 3 parts of Hydrogen Peroxide H_2O_2 and 1 part of ammonium hydroxide NH_4OH solution. Once a sample is carefully prepared and checked by imaging in SEM, mount the sample (a single die separated from the processed wafer) onto the special stub which has a 70º wedge surface.

The principle steps for running an EBSD experiment were outlined in the flow chart Figure 4-13. And the detail of each main step is given as following: a) Load the sample/stub into the SEM chamber with the specimen surface is at 70º from the horizontal; adjust the tilted specimen surface to a suitable working distance of usually 20 – 22 mm. b) The microscope operating parameters for most of the measurements are set

as accelerating voltage of 20 kV, probe current of 8nA and magnification of 50000 X. Focus the image as perfect as possible under this condition before inserting the Nordlys detector. c) With the detector located at the operating position, start software Flamenco and acquire a SEM image through Flamenco with adjusted magnification and tilt correction to assure the SEM image appeared correctly with the right scale bar. d) After acquiring an appropriate SEM image with Flamenco, proceed to the camera set up step for enabling the acquisition of good quality EBSPs, which including select the desired level of binning and gain level: 4 x 4 binning and a low gain level are employed mostly. Other parameters like timing per frame and number of frames for background collection are need to be altered and set until a good quality EBSP is obtained when position beam on the frozen SEM image. e) In order to index a collected EBSP, possible phase(s) presented in the sample are needed to be load into the match unit window by either select from available phase database or created individually. f) Before detect bands and index the collected EBSP, a routine calibration of the detector distance and pattern center is required to get reliable index results. g) Detect and index the Kikuchi bands collected on the EBSP by band edges with a minimum of 4 and a maximum of 5 bands, Figure 4-12 shown an example of a detected and indexed EBSP. Check the Mean Angular Deviation (MAD) to affirm good match between the detected Kikuchi banks and the simulation. The smaller the number, the better the match, a number less than 1° is acceptable for most systems. Repeat this indexing cycle for several EBSPs before moved to the Automatic data collection step. h) Ensure that the EBSPs are of a reasonable quality, begin collecting the data using automated EBSD to map areas on the sample surface, this is usually done by collecting EBSPs from a regular grid on the sample surface, from which

an orientation or phase map can be reconstructed. Two options of scan method are available in Flamenco: Beam scan and stage scan. In our study, beam scan mapping was chose over stage scan mapping due to the advantage of being much faster and with better spatial resolution. For most of samples, areas of 0.5-5 μm^2 were scanned at step internals of 0.005 – 0.05 μm depending on the grain features. The approximate time per scan job was controlled within a period of 2 hr. Longer scan times were avoided in order to prevent drift problems. EBSD analyses were repeated over 4-10 different regions for each sample film to obtain reliable and reproducible data. It is important to balance the requirements of total experiment time, orientation accuracy and spatial resolution when designing an EBSD experiment.
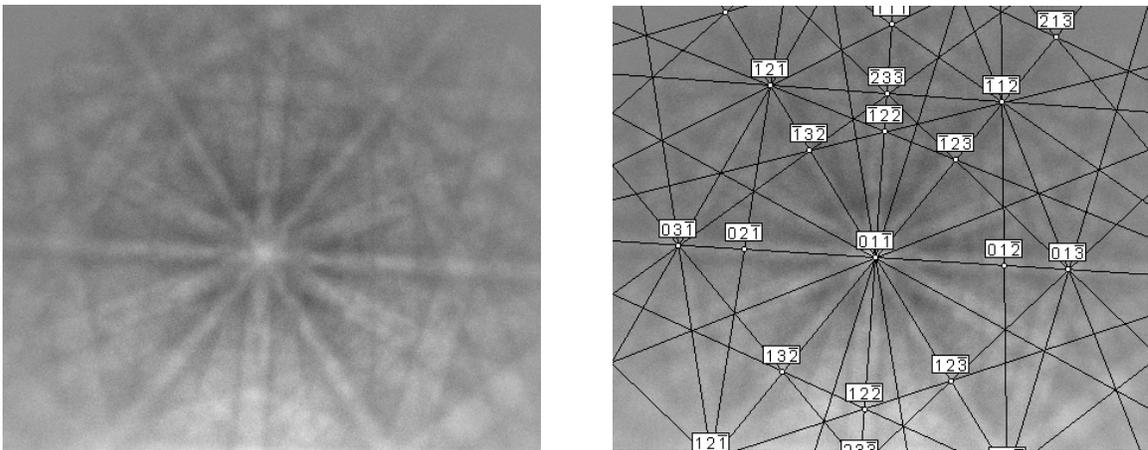
Figure 4-12 An example of detected EBSP and indexed EBSP.

Once finishing the collection of data, proceed to the data post processing step by utilizing the multiple analyze software provided with the CHANNEL 5 system. The mainly used ones are:

- Tango – the mapping software, used for plotting maps, boundaries, measuring grain sizes, determining area fractions etc.

- Mambo- the texture software for plotting orientations and misorientations in both pole figures and inverse pole figures.

- Salsa- the software for calculating and plotting orientation and misorientations distribution functions.

```
┌─────────────────────────────┐
│ Load sample in SEM at a     │
│ suitable WD                 │
└─────────────────────────────┘
              │
              ▼
┌─────────────────────────────┐
│ Set up SEM (Acceleration    │
│ Voltage Probe Current,      │
│ Focus)                      │
└─────────────────────────────┘
              │
              ▼
┌─────────────────────────────┐
│ Switch on Nordlys control   │
│ box and Insert detector to  │
│ operating position          │
└─────────────────────────────┘
              │
              ▼
┌─────────────────────────────┐      ┌──────────────────────────┐
│ Start Flamenco Acquire SEM  │      │ Choose Nordlys Pixel     │
│ image with Flamenco         │      │ binning level            │
│ Adjust magnification and    │      └──────────────────────────┘
│ tilt correction             │                  │
└─────────────────────────────┘                  ▼
              │                      ┌──────────────────────────┐
              ▼                      │ Set acquisition time and │
┌─────────────────────────────┐      │ collect background       │
│ Setting up for EBSP indexing│──┐   └──────────────────────────┘
└─────────────────────────────┘  │               │
              │                   │               ▼
              ▼                   │   ┌──────────────────────────┐
┌─────────────────────────────┐  │   │ Switch on pattern        │
│ Position beam on the frozen │  │   │ enhancement and select   │
│ SEM image and Snap EBSP     │  │   │ # of frames              │
└─────────────────────────────┘  │   └──────────────────────────┘
              │                   │               │
              ▼                   │               ▼
┌─────────────────────────────┐  │   ┌──────────────────────────┐
│ Run a routine calibration   │  └──│ Load match unit and set  │
└─────────────────────────────┘      │ max # of reflectors      │
              │                      └──────────────────────────┘
              ▼
┌─────────────────────────────┐
│ Detect bands and Index EBSP │
└─────────────────────────────┘
              │
              ▼
┌─────────────────────────────┐      ┌──────────────────────────┐
│ Repeat indexing cycle for   │──┐   │ Select job type          │
│ several EBSPs – Ready for    │  │   └──────────────────────────┘
│ Data Collection             │  │               │
└─────────────────────────────┘  │               ▼
              │                   │   ┌──────────────────────────┐
              ▼                   │   │ Define job parameters    │
┌─────────────────────────────┐  │   │ (Grid size, step size    │
│ Collecting data in Automatic│──┘   │ etc)                     │
│ mode with Flamenco          │      └──────────────────────────┘
└─────────────────────────────┘                  │
              │                                   ▼
              ▼                      ┌──────────────────────────┐
┌─────────────────────────────┐      │ Add job to the job list  │
│ Post processing data with   │      │ and Press "Run"          │
│ CHANNEL 5 system software   │      └──────────────────────────┘
└─────────────────────────────┘
```

Figure 4-13 The flow chart of the principle steps for running an EBSD experiment.

4.4.3 Orientation and Texture Results from EBSD

The EBSD system (HKL, channel 5) used in this study was attached to a JEOL JSM-7000F SEM instrument equipped with a field emission gun. The measurements were carried out at a working distance of 20 - 22 mm and an accelerating voltage of 20 kV. Areas of 0.5-5 μm^2 were scanned at step internals of $0.005 – 0.05$ μm to determine grain orientations, size and shape. The approximate time per scan job was controlled in the period of 2 hr. Longer scan times were avoided in order to prevent drift problems. EBSD analyses were repeated over 4-15 different regions for each film thickness to obtain reliable and reproducible data. The number of grains investigated via EBSD varied from 300 to 800 for the different film thicknesses (different grain size). Using the Tango HKL software, the grain size can be measured. For grain detection a critical misorientations of 5º was specified and the twin boundaries were ignored. Furthermore, the boarder grains were excluded from the grain size statistics. Using the Mango HKL software, the texture of the films can be measured and presented as the inverse pole figures.

EBSD orientation maps with Euler shading for evaporated and sputtered gold films are shown comparatively in Figure 4-14 to Figure 4-16. In order to achieve sufficient resolution as well as a large measuring area without prolonging the required scan time, the step size was increased from $0.005 – 0.05$ μm with increasing film thickness. The resulting maps revealed the constituent grain morphology, orientations, and boundaries. This data also shows good agreement with the grain structure characterized by SEM.
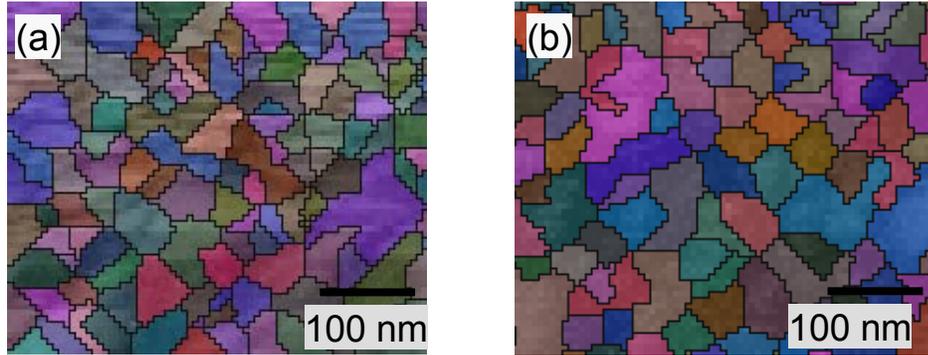
Figure 4-14 EBSD orientation maps with Euler shading for (a) 0.25 μm thick EBeam evaporated film and (b) 0.25 μm thick sputtered film.
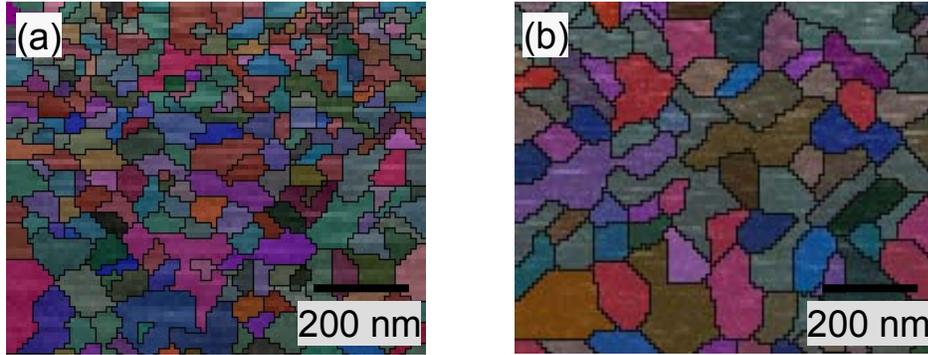
Figure 4-15 EBSD orientation maps with Euler shading for (a) 0.50 μm thick EBeam evaporated film and (b) 0.50 μm thick sputtered film.
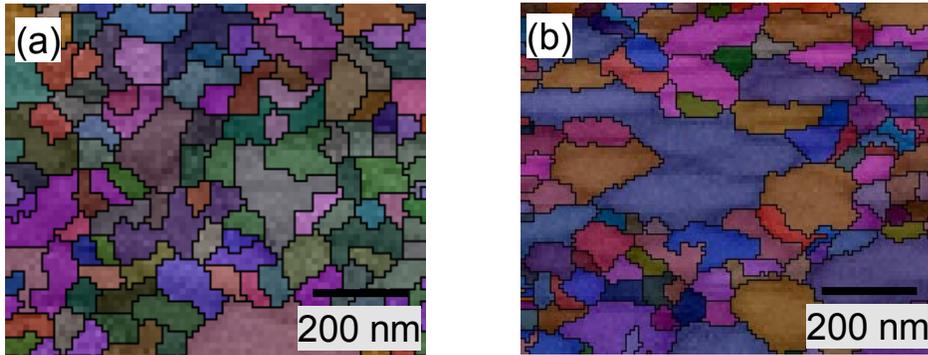
Figure 4-16 EBSD orientation maps with Euler shading for (a) 1.00 μm thick EBeam evaporated film and (b) 1.00 μm thick sputtered film.

Textures of the deposited gold films were represented by the inverse pole figures, which are shown in Figure 4-17 for EBeam evaporated films and Figure 4-18 for sputtered films with thicknesses of 0.25 μm, 0.50 μm and 1.00 μm.
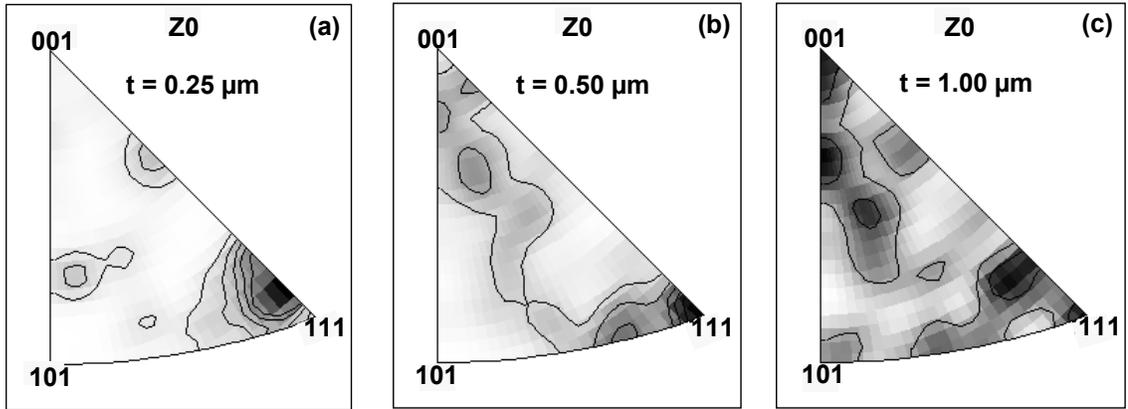
Figure 4-17 Inverse pole figures illustrating the film texture as viewed from the film surface for EBeam evaporated gold films (a) 0.25 μm, (b) 0.50 μm and (c) 1.00 μm thick.
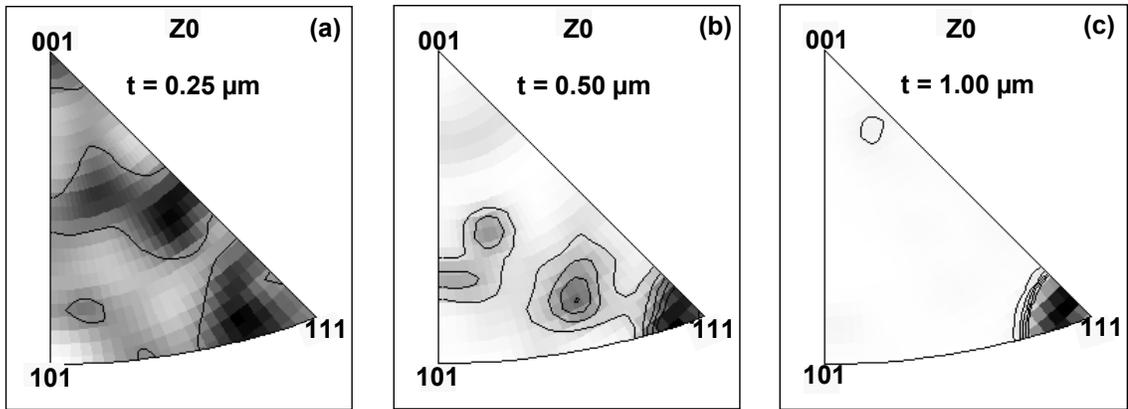
Figure 4-18 Inverse pole figures illustrating the film texture as viewed from the film surface for sputtered gold films (a) 0.25 μm, (b) 0.50 μm and (c) 1.00 μm thick.

The texture of the evaporated gold films are seen to progress a transition from a predominant (111) texture for the thinnest film of 0.25 μm to a more mixed texture at 1.00 μm occurred, which appears to be in the process of developing a preferred (100)

114

texture. The (111) texture is expected since this plane possesses the minimum surface energy, especially for the thinner films owing to the larger proportion of the exposed grain surface area to the film structure volume [10-12]. Most prior texture characterization of thin metallic films involved x-ray studies that are not very adept at assessing the micro-texture of a thin film [7-9] and may not observe this transition. The gradually growth of the preferred (100) texture component on top of the (111) texture with increasing film thickness has also been observed by other researchers in other FCC thin metallic films, namely Cu and Ag [13-16], which were all in good agreement with the predictions of the texture evolution model proposed by Thompson and Carel [1, 5].

The sputtered films, on the other hand, are seen to progress from a mixed texture at 0.25 μm to a well-defined (111) texture at 1.00 μm. A strong (111) crystallographic texture was observed for the thicker sputtered films while the Ebeam processed films exhibited a more mixed orientation with (001) showing a stronger intensity. The sputtered films were subjected to increased thermal and kinetic energy during deposition, which imparted additional energy to the atoms to arrange in more favorable positions. In contrast, the Ebeam deposited films possessed lower grain size and less clear texture. The extra energy imparted to the atoms in the sputtered films is analogous to a low-temperature anneal and thus resulting in a larger grain size and a clear texture development.

It is expected that this observed structural evolution will significantly impact the mechanical properties of the films tested in this work. However, it should be noted that the EBSD technique samples only the first few nanometers of the film, which may vary from the remaining film volume.

4.5 References

[1]   C. V. Thompson and R. Carel, "Grain growth and texture evolution in thin films," in *Grain Growth In Polycrystalline Materials II*, vol. 204-, *Materials Science Forum*, 1996, pp. 83.

[2]   C. V. Thompson, "Structure evolution during processing of polycrystalline films," *Annual Review of Materials Science*, vol. 30, pp. 159-190, 2000.

[3]   R. J. Young and M. V. Moore, "Dual-Beam (FIB-SEM) Systems," in *Introduction to Focused Ion Beams*, L. A. Giannuzzi and F. A. Stevie, Eds. New York: Springer, 2005.

[4]   ASTM, "Standard E112-96E2," in *Annual Book of ASTM Standards*, 1996.

[5]   C. V. Thompson and R. Carel, "Stress and grain growth in thin films," *Journal Of The Mechanics And Physics Of Solids*, vol. 44, pp. 657, 1996.

[6]   C. V. Thompson, "The Yield Stress of Polycrystalline Thin-Films," *Journal of Materials Research*, vol. 8, pp. 237-238, 1993.

[7]   A. J. Schwartz, M. Kumar, and B. L. Adams, *Electron Backscatter Diffraction in Materials Science*. New York: Kluwer Academic Publishers, 2000.

[8]   U. F. Kocks, C. N. Tomé, H. R. Wenk, and H. Mecking, *Texture and Anisotropy*. Cambridge: Cambridge University Press, 2001.

[9]   H. J. Bunge, *Texture Analysis in Materials Science*. Toronto: Butterworths, 1982.

[10]   L. Vitos, A. V. Ruban, H. L. Skriver, and J. Kollár, "The Surface Energy of Metals," *Surface Science*, vol. 411, pp. 186-202, 1998.

[11]   C. V. Thompson and R. Carel, "Texture Development In Polycrystalline Thin-Films," *Materials Science & Engineering, B: Solid-State Materials for Advanced Technology*, vol. 32, pp. 211, 1995.

[12]   C. L. Liu, J. M. Cohen, J. B. Adams, and A. F. Voter, "EAM Study of Surface Selfdiffusion of Single Adatoms of FCC Metals Ni, Cu, Al, Ag, Au, Pd, and Pt.," *Surface Science*, vol. 253, pp. 334-344, 1991.

[13]   J.-M. Zhang, K.-W. Xu, and V. Ji, "Competition between surface and strain energy during grain growth in free-standing and attached Ag and Cu films on Si substrates," *Applied Surface Science*, vol. 187, pp. 60, 2002.

[14]   P. Sonnweber-Ribic, P. Gruber, G. Dehm, and E. Arzt, "Texture transition in Cu thin films: Electron backscatter diffraction vs. X-ray diffraction," *Acta Materialia*, vol. 54, pp. 3863, 2006.

[15]   M. T. Perez-Prado and J. J. Vlassak, "Microstructural evolution in electroplated Cu thin films," *Scripta Materialia*, vol. 47, pp. 817, 2002.

[16]   N. J. Park, D. P. Field, M. M. Nowell, and P. R. Besser, "Effect of Film Thickness on the Evolution of Annealing Texture in Sputtered Copper Films," *Journal of Electronic Materials*, vol. 34, pp. 1500-1508, 2005.

CHAPTER 5

RESULTS OF MECHANICAL TESTING OF EVAPORATED AND SPUTTERED FILMS

In this chapter, the primary objective is to report the qualitative observation of the mechanical testing performed on thin gold films at room temperature. The discussions of these results will be given with details in the following chapter. Many repeat tests have been performed for each sample films to ensure that the results reported are statistically significant.

The size effect was studied on freestanding thin gold film. We only reported the results of evaporated films here because the sputtered sample shared the similar trends. The more important aspect of this work is the comparative study of the mechanical behavior for the thin gold films deposited by two different techniques: EBeam evaporation and sputtering. Also, various loading conditions are applied to investigate the strain rate effect for the mechanical behavior of thin film materials.

5.1 Interpretation of Stress-Strain Curves from MDE Tests

As described in Chapter 3, stress-strain curves can be generated by the interpretation of the nanoindenter and interferometer data, see Figure 5-1, which is a typical stress-strain curve obtained from MDE test. Mechanical properties including

Young's modulus, yield strength, tensile strength and fracture strain etc. can be extracted from the curve as illustrated.
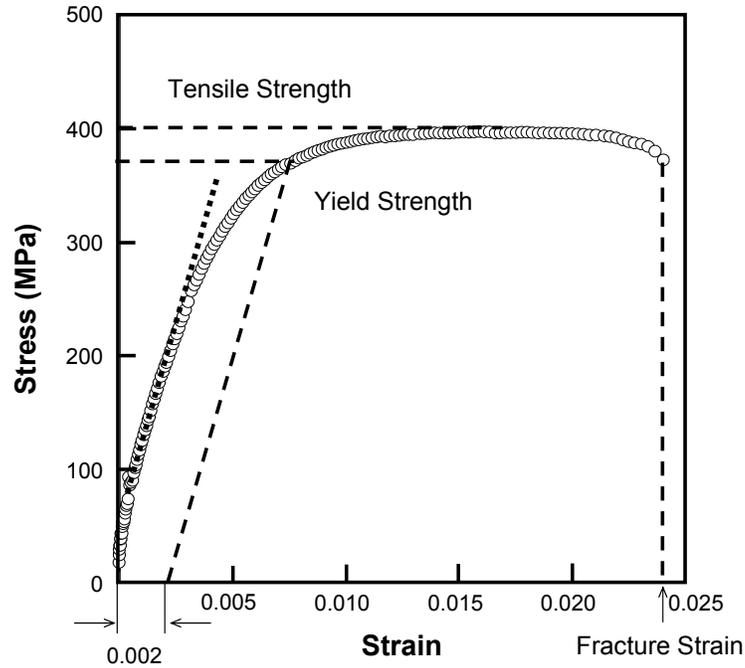
Figure 5-1 A representative stress-strain curve obtained from MDE test.

5.1.1 Elastic Modulus

As shown in Figure 5-1, a roughly linear region was found at the very beginning of the stress-strain curve. However, the modulus was not taken as the slope of this portion of data from the stress-strain curve. In order to make an accurate determination of the tensile modulus, it was decided to use the data when the sample was at higher loads, as this is presumably the time when the membrane is loaded most uniformly (no bending, pure stretching). A linear fit was then performed to the stress-strain data at high loads region, see the dotted line in Figure 5-1, and the slope of this linear fit generates an elastic modulus.

119

The stress-strain curve showed in Figure 5-1 is a representative stress-strain curve from MDE test. However, for each sample, at least five membranes were tested; therefore, five independent stress-strain curves were generated and used to determine the mechanical properties. A linear fit was performed at the same data range to each individual stress-strain curve and the average value of the five slopes yields the reported modulus.

5.1.2 Yield Strength and Tensile Strength

Yield Strength: For the mechanical testing of large-scale specimen, the convention of the 0.2 % offset rule has been established to identify the yield strength of a material. Basically, the yield strength of our tested films was defined by adopting this same convention. However, there are a few issues to contemplate in using this offset method to find the yield strengths of the films tested here. For materials such as gold, their stress-strain curves do no exhibit a very sharp and distinct yield point, developing a consistent way of measuring the yield strength can be difficult. Furthermore, as stated earlier, the stress-strain curves were roughly linear at the beginning of the test, presumably because of non-uniform loading at the outset of the test. This makes the slopes of the stress-strain curves at low load varied slightly in some cases, which would affect any yield strength measurement based on strain offset. Therefore, the stress-strain curves used to determine the yield stress have to be carefully chosen and calibrated. Also, an accurate liner fit for the determination of Young's modulus from the stress-strain curves is very critical for the measurement of the yield strength. In practice, the reported yield strength value was obtained by averaging five or more stress-strain curves for a given kind of sample.

Tensile Strength: The tensile strength is the stress at the maximum on the engineering stress-strain curve. This corresponds to the maximum stress that can be sustained by a structure in tension; if this stress is applied and maintained, fracture will result. The determination of tensile strength from the stress-strain curves is relatively easier compared to the yield strength.

The fracture strength corresponds to the stress at fracture. Ordinarily, when the strength of a metal is cited for design purposes, the yield strength is used. Furthermore, fracture strengths are not normally specified for engineering design purposes. Therefore, in this work, only the yield strength and tensile strength are measured and studied.

5.1.3 Fracture Strain/Ductility

Ductility is another important mechanical property. It is a measure of the degree of plastic deformation that has been sustained at fracture. Ductility may be defined quantitatively as either percent elongation or percent reduction in area at fracture, and it can be expressed in terms of the percent elongation as following:

$$\%EL = (\frac{l_f - l_0}{l_0}) \times 100 \qquad (5\text{-}1)$$

where l_f and l_0 are the fracture length and original gauge length of the tested membrane respectively. The determination of fracture strain/ductility from the stress-strain curves is quite straightforward as illustrated in Figure 5-1.

5.2 Qualitative Observations from MDE Tests

5.2.1 Repeatability and Reliability

Figure 5-1 is a typical stress-strain curve obtained from MDE test, represents the average for at least five test curves for a given sample. An important feature of every experimental method is repeatability in the measurements. To examine this issue, some reliability experiments were designed and conducted.

Figure 5-2 is the stress-strain curves for one group (Group k) of five evaporated film membranes with identical dimensions (thickness (t) = 0.50 μm, half length (L_H) = 200 μm, width (w) = 5 μm) suspending on the same window, denoted as M1-M5 (M represent Membrane) in Figure 5-2. As shown in Figure 5-2, a high repeatability in the measurement of the MDE method can be achieved. Another reliability experiment is to perform four tests on four sputtered membranes of the same size (Group d) chosen from different dies within two wafers, denoted as W1-D1-M1, W1-D2-M2, W2-D1-M1, and W2-D2-M4 (W represent wafer; D represent die) in Figure 5-3. The stress-strain signatures from these thin film gold membranes are shown in Figure 5-3. The membranes compared all have identical dimensions: thickness (t) = 0.50 μm, half length (L_H) = 350 μm and width (w) = 10 μm. The films tested are all originating from the same run of EBeam deposition and tested at a displacement rate of 200 nm/s.

Because these films are nominally the same, and tested under similar conditions, this figure is an example of the scatter of the data for similar material. The variations are presumed to reflect sample to sample variability. The signatures of the curves are similar to one another, and the values for parameters such as modulus, tensile strength and ductility are fairly uniform. This was found to be true for all samples originating from the

same lot of films and indicates that the MDE procedure is a repeatable and reliable method to uniformly stretch, much like a direct tensile test, thin films and MEMS materials at the micro scale.
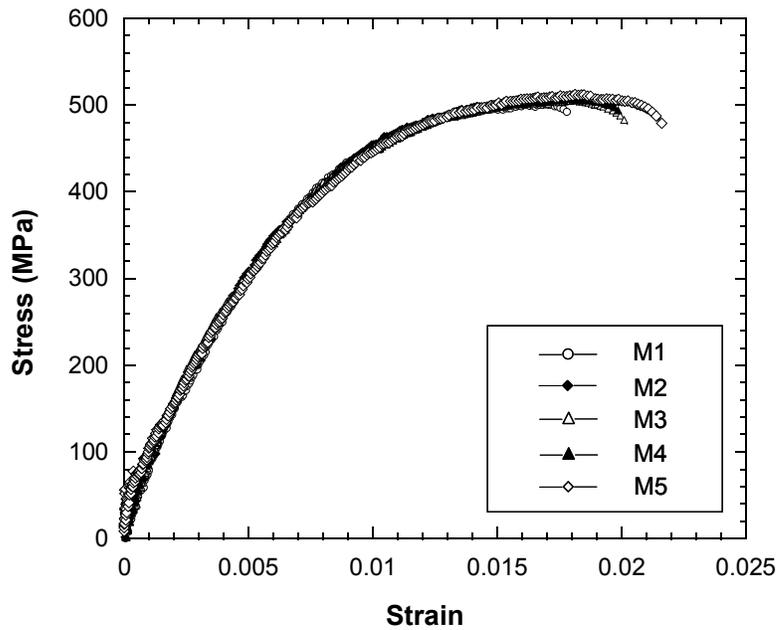
Figure 5-2 Stress-strain curves for one group of 5 evaporated gold membranes with identical dimensions (thickness = 0.5 µm, half length = 200 µm, width = 5 µm).
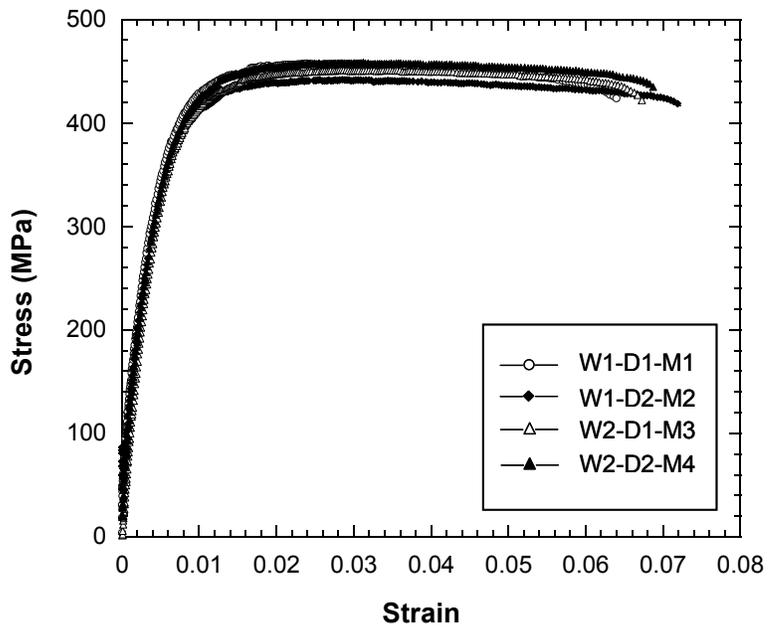
Figure 5-3 Stress-strain curves for 4 sputtered gold membranes with identical dimensions (thickness = 0.5 µm, half length = 350 µm, width = 10 µm).

5.2.2 Results of Evaporated Films and Sputtered Films Tested at Same Strain Rates

In this session, the mechanical behaviors reported for both the evaporated and sputtered films are all tested at the same displacement rate of 200 nm/s. Although strain rate may change from membrane to membrane slightly according to the definition for applied strain rate by equation (3-6) described in Chapter 3, the variation is negligible and will be considered as the same loading condition. The size effects including length effect, width effect and thickness effect were studied on freestanding thin gold films. Besides, the different behaviors between the membranes with and without an artificial defect notch are compared. However, the most important aspect of this work is to investigate the different mechanical behavior for the thin gold films deposited by two different techniques: EBeam evaporation and sputtering. Therefore, the resulted stress strain curves for each case of effect study are displayed in a comparative fashion for EBeam evaporated films and sputtered films.

Effect of Membrane Length

The length effect was studied on the 0.50 μm thick evaporated films. Figure 5-4 shows the stress-strain curves for the films with width of (a) 5 μm, half length of 200 and 350 μm and (b) 7.5 μm, half length of 200 and 350 μm. We only reported the results of evaporated films for the length effect study here because the sputtered sample shared the similar trends. Moreover, as seen in Figure 5-4, beside the fracture strain who varied with the length accordingly, the overall mechanical behavior was not affected by the membrane half length greatly.
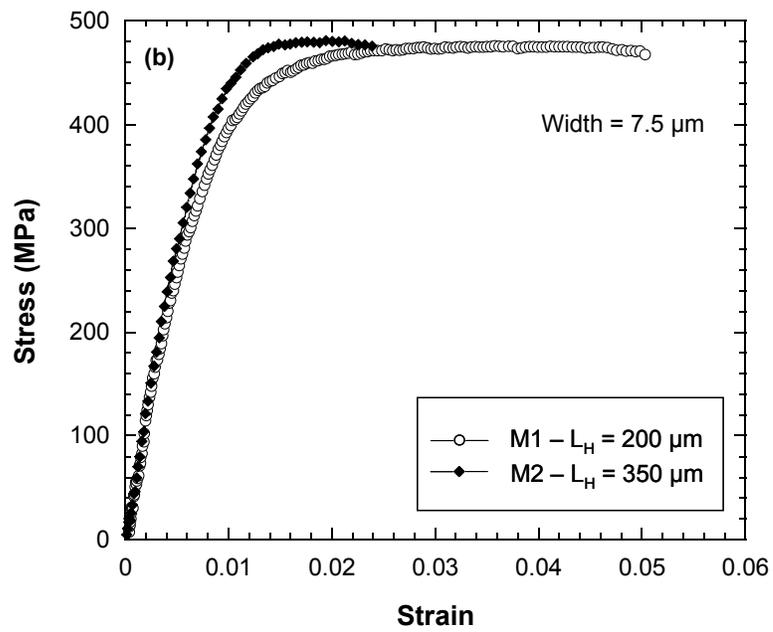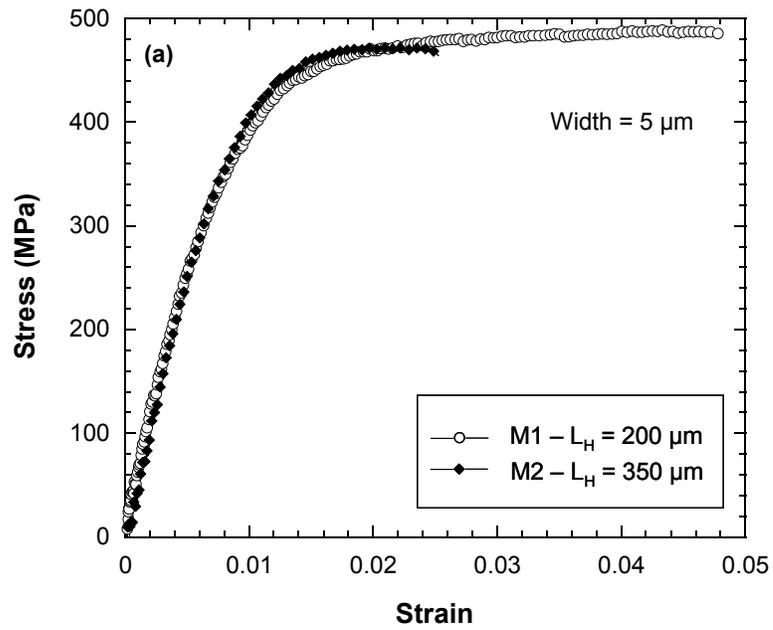
Figure 5-4 Stress-strain curves for (a) film width of 5.0 µm and (b) film width of 7.5 µm evaporated gold membranes with membrane half length of 200 and 350 µm.

Effect of Membrane Width

Figure 5-5, 5-6, and 5-7 show the stress-strain curves for evaporated and sputtered gold films 0.25, 0.50, and 1.00 μm thick, respectively. Each plot shows the effect of membrane width of 7.5 and 10 μm (5.0, 7.5 and 10 μm for 0.50 μm thick films) on the mechanical response of all tested films.

For the 0.25 μm thick specimens, both evaporated and sputtered films exhibited similar response to the variation of the membrane width. In both cases, a well defined elastic regime can be found; the narrower films possessed relatively higher yield strength and less ductility. For evaporated films, beside the plastic part, the elastic region was also influenced by the membrane width to some extent. The narrower film shows an extended elastic zone and a larger yield stress of 480 MPa compared to the 320 MPa for specimen of 10 μm width. The Young's modulus for the 7.5 μm width film is slightly higher than the 10 μm width film by ~5 GPa. For sputtered films, the specimens of widths 7.5 and 10 μm exhibit nearly identical elastic region; some variability on the yield strength and fracture strain are presented. It is necessary to note that for the purpose of display clarity, the strain axis for the figures (a) evaporated films and (b) sputtered films are not identical and it is easy to oversee the fact that the sputtered films possessed much larger ductility than the evaporated films.

Increasing the film thickness to 0.50 μm resulted in a nearly identical effect to the mechanical behavior for 0.50 μm thick films as the 0.25 μm thick specimens, see Figure 5-6. As with the 0.25μm thick membranes, all 0.50 μm thick specimens with membrane widths of 5.0, 7.5, and 10 μm show a clear defined elastic region with a Young's modulus of 51-55 GPa for evaporated films and 67-70 GPa for sputtered films. The

overall yield stress of the 0.50 μm thick films is lower than the thinner films, and the difference in ductility is not as much as for the 0.25 μm films.

The 1.00 μm thick thin film specimens exhibited distinctly different deformation and failure behavior. Figure 5-7 shows the stress-strain curves for this thickness. Young's modulus for the 1.00 μm thick specimens was found to be 62-65GPa for evaporated films, which is higher than the thinner films; and 68-72 GPa for sputtered films, which is consistent with 0.25 and 0.50 μm thick specimens. However, significant lower yield strength and ductility are found in the 1.00 μm thick films. The 7.5 μm and 10 μm width membranes did not exhibit as significant effect as in the case of the thinner films in terms of both elasticity and plasticity.

These results clearly indicate that size effects appear to have a significant influence on deformation behavior for both the evaporated films and sputtered films. In the case of decreasing membrane width, it is clear that the number of grains contained in that width directly affect the onset of plastic yielding. The more grains, the lower the yield stresses. This could result from geometric constraints in deformation mechanisms or from strong statistical effects due to the small number of grains. Membrane thickness also plays a major role in deformation behavior. In the plots presented thus far, it is a little inconvenient to directly observe thickness effects. The thickness effects will be discussed in the next section, where the data are reexamined by directly plotting thickness data for membranes of equal width at various applied strain rates.
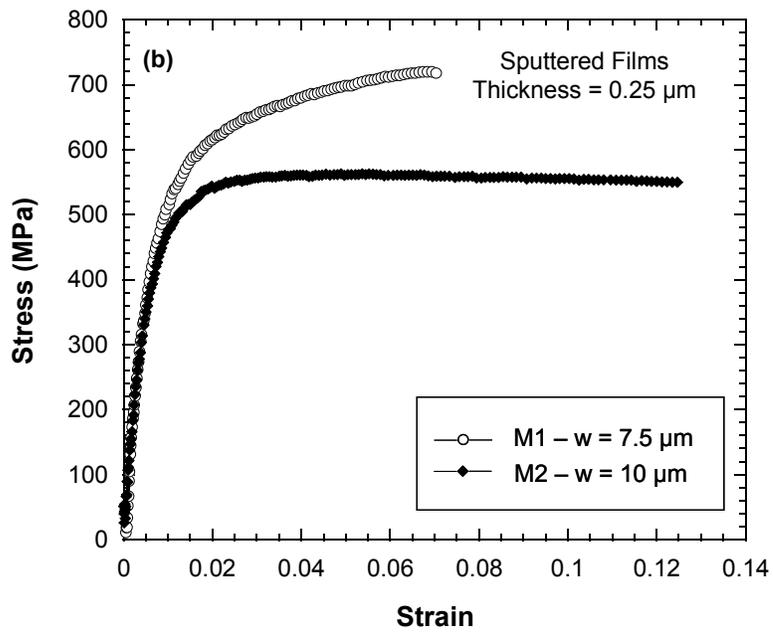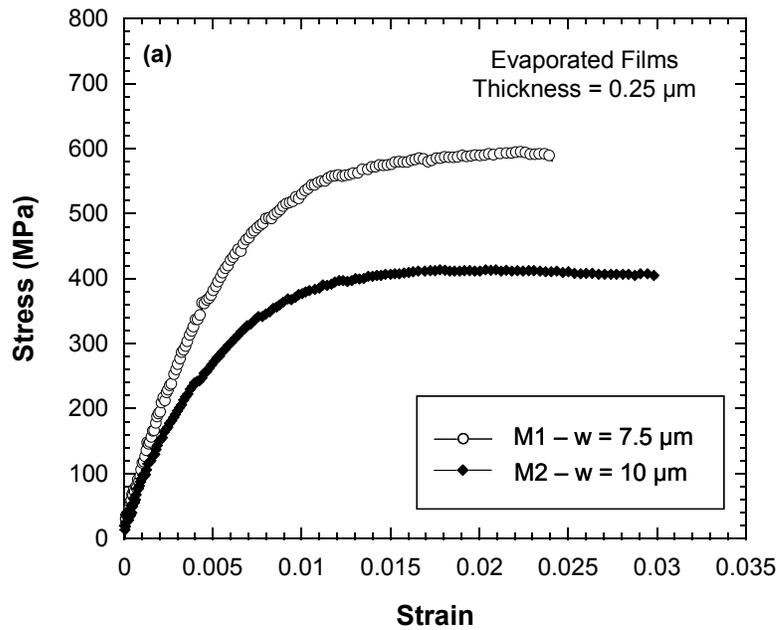
Figure 5-5 Stress-strain curves for a film thickness of 0.25 µm (a) evaporated films and (b) sputtered films with membrane width of 7.5 and 10 µm.
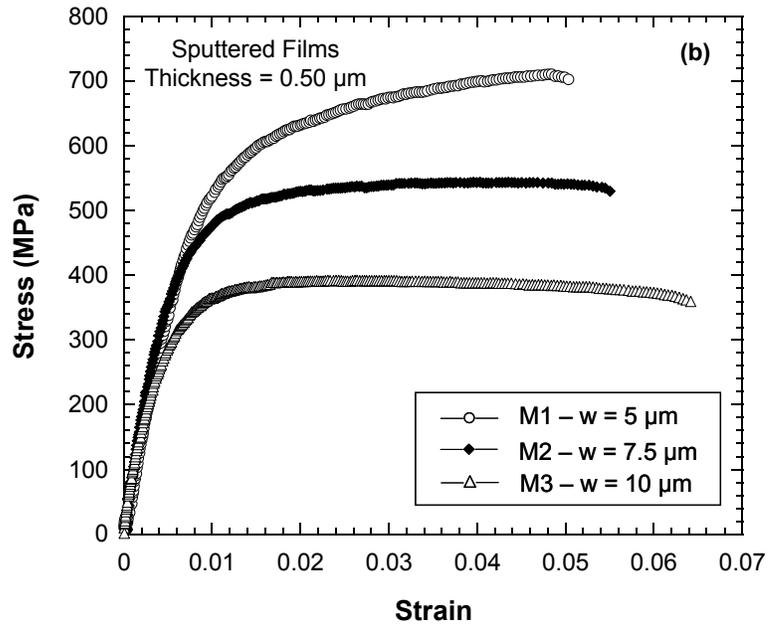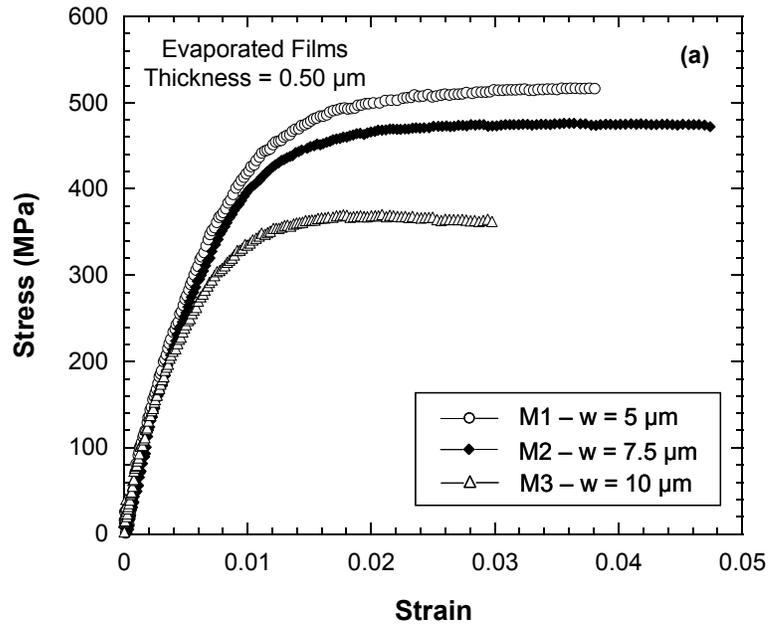
Figure 5-6 Stress-strain curves for a film thickness of 0.50 µm (a) evaporated films and (b) sputtered films with membrane width of 5.0, 7.5 and 10 µm.
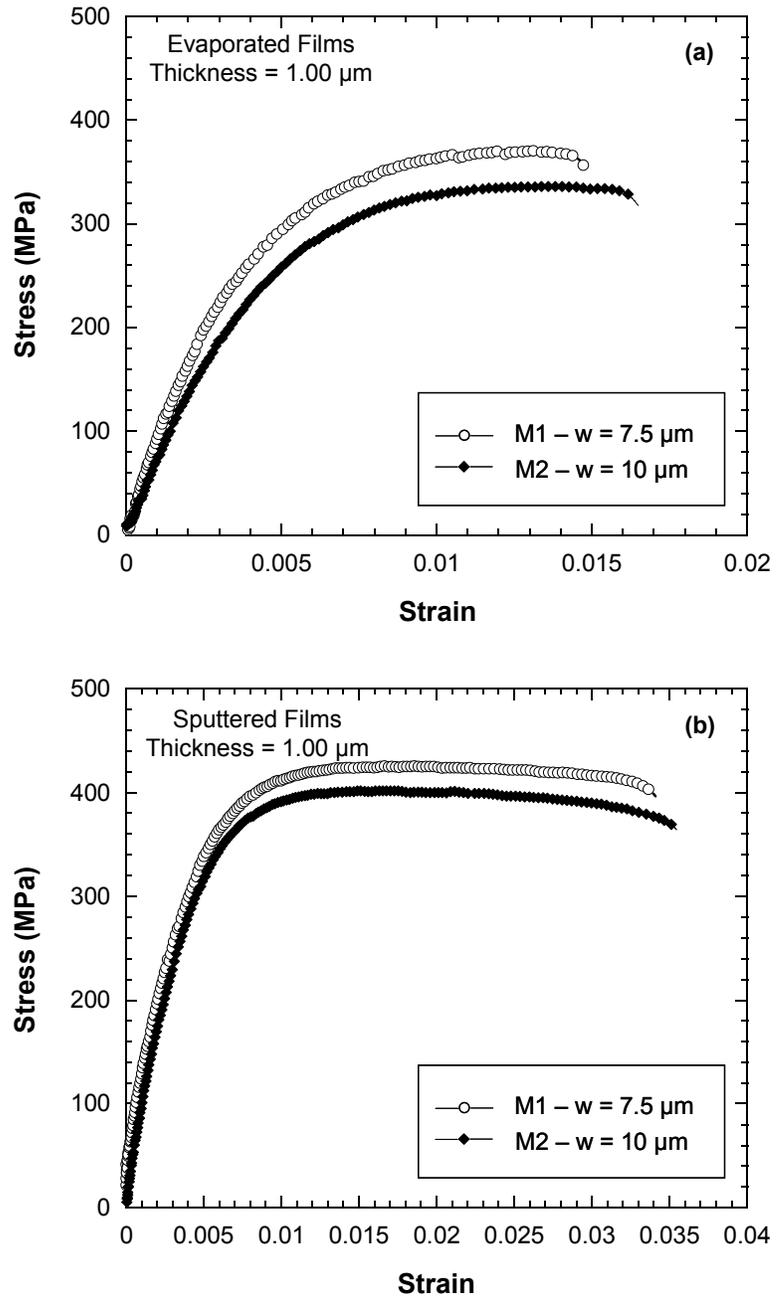
Figure 5-7 Stress-strain curves for a film thickness of 1.00 µm (a) evaporated films and (b) sputtered films with membrane width of 7.5 and 10 µm.

Effect of Artificial Defect

To study the effect of artificial defect to the fracture behavior of freestanding thin gold films, MDE specimens with opened notches at the gauge area were designed. Figure 5-8 shows the stress-strain curves for evaporated gold films of 0.50 μm thick, two groups (width of 5 μm specimens and width of 10 μm specimens) of membranes with identical dimension except one is with notch and the other is without. Only the evaporated samples were reported here because the sputtered ones show the nearly identical trend. The stress-strain curves for membranes with and without notch show a clear defined elastic region as all the other specimens. The yield stress for both specimens is agreed well with the regular samples. The most distinctive difference between these two kinds of membranes is the more brittle like fracture behavior presented by membranes with notch.

Strain rate is not considered as an issue so far when comparing membranes of different width or thickness although as we mentioned earlier that the strain rate may change from membrane to membrane slightly according to the definition for applied strain rate by equation (3-6) described in Chapter 3. The strain rate variations are not large enough for is strain rate effects to be identified, and for strain rate effect investigation in this work, we designed a systematic study as presented in the next section.
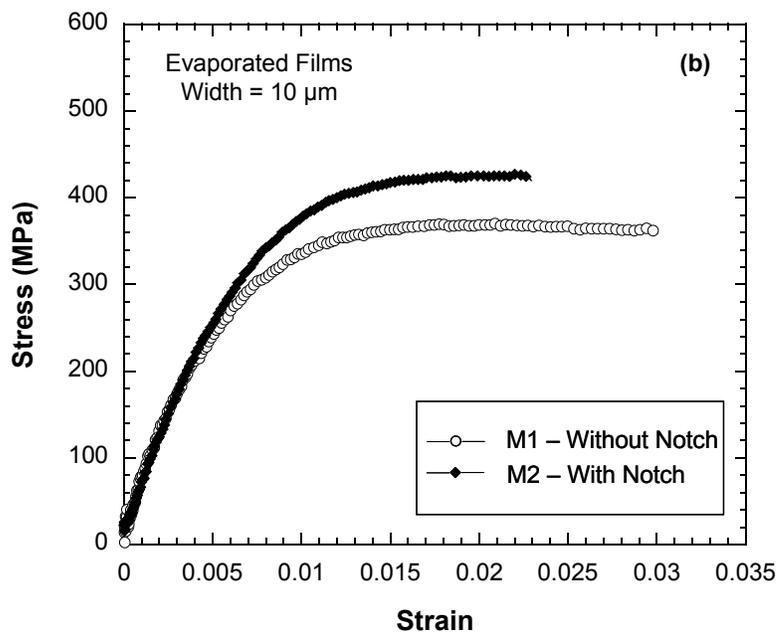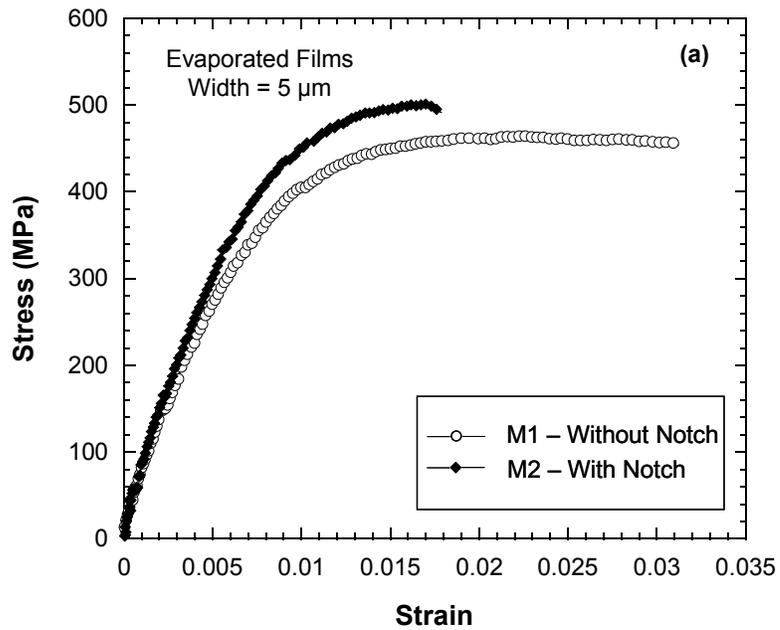
Figure 5-8 Stress-strain curves for (a) film width of 5.0 µm and (b) film width of 10 µm evaporated gold membranes with and without an artificial defect notch.

5.2.3 Results of Evaporated Films and Sputtered Films Tested at various Strain Rates

The stress-strain curves generated from the membrane deflection experiment for films 0.25, 0.50 and 1.00 μm thick are shown in Figure 5-9, 5-10 and 5-11 respectively. Each figure compiles the average of five specimen curves of all displacement rates applied; 10, 50, 200, 500 and 1000 nm/s for both evaporated films and sputtered films. All the specimens for strain rate study are from group (d) and possess identical dimensions as thickness (t) = 0.50 μm, half length (L_H) = 350 μm and width (w) = 10 μm. Material properties such as Young's modulus and yield strength can be easily identified as well as variations in fracture behavior. For each film thickness, the stress-strain curves exhibited notable differences in response to the variety of displacement rates applied, more so for the thinner films. In general, evaporated films exhibited a higher sensitivity to the strain rate than the sputtered films; also, the plastic properties were found to be very sensitive to displacement rate while elastic properties remained relatively unchanged. Table 5-1 and Table 5-2 summarize all measured properties and characteristics of these specimens respectively.

The elastic response of the films did not appear to be influenced by the applied displacement rate as Young's modulus remained relatively constant for each thickness as displacement rate was varied.

The plastic properties of the films were significantly influenced by the applied displacement rate. Yield strength was observed to vary greatly with displacement rate as shown in Figure 5-9 to 5-11 as well as Table 5-1 and 5-2. For evaporated films, The yield strength of all films tested at a displacement rate of 10 nm/s was in the range of

approximately 220 to 230 MPa. As displacement rate increased yield strength was observed to increase significantly to values as high as 390 GPa at a displacement rate of 1000 nm/s. In this regard, the thinner films exhibited the largest variability with both the 0.25 and 0.50 μm films increasing by ~60 to 70 % as displacement rate increased from 10 to 1000 nm/s, while the 1.00 μm film increased by only ~30 %. For sputtered films, The yield strength of all films tested at a displacement rate of 10 nm/s was in the range of approximately 280 to 410 MPa. As displacement rate increased yield strength was observed to increase fairly to values of 520 GPa at a displacement rate of 1000 nm/s for the thinnest films. Not like the evaporated films, in the case of sputtered films, the thicker films exhibited the relatively larger variability in yield strength values with both the 0.50 and 1.00 μm films increasing by ~50 to 60 % as displacement rate increased from 10 to 1000 nm/s, while the 0.25 μm film increased by only ~20 %.
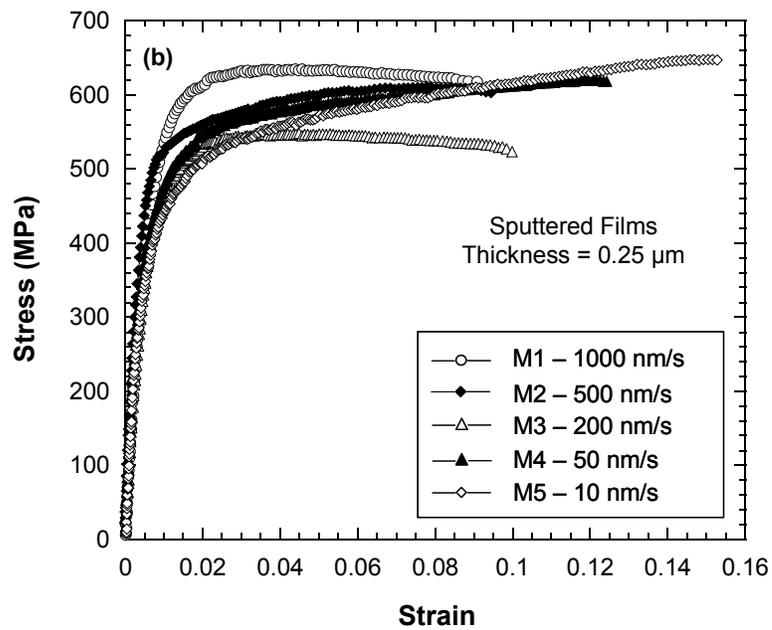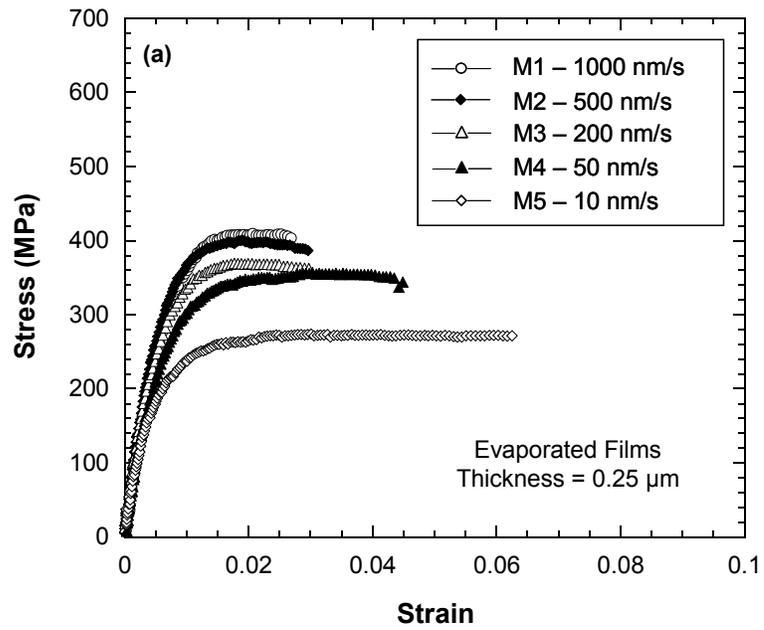
Figure 5-9 Stress-strain curves for the 0.25 µm thick (a) evaporated films and (b) sputtered films at the five displacement rates applied.
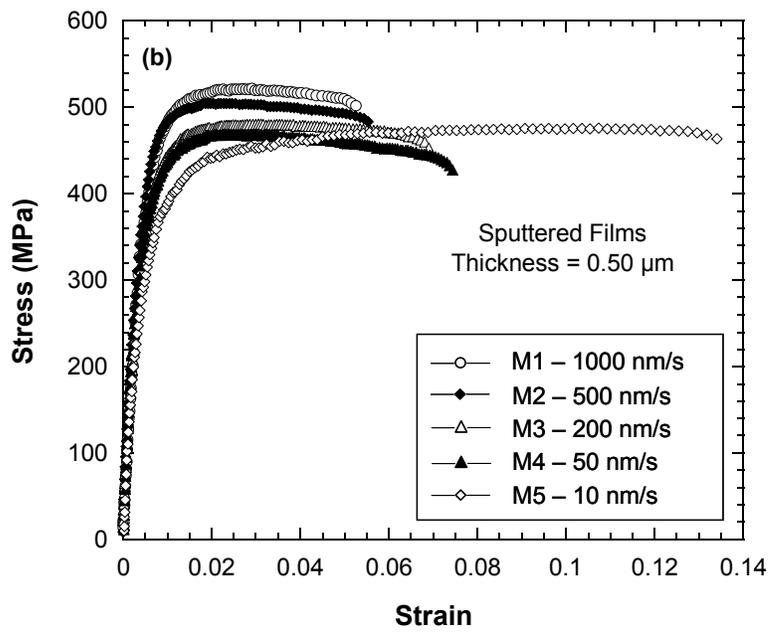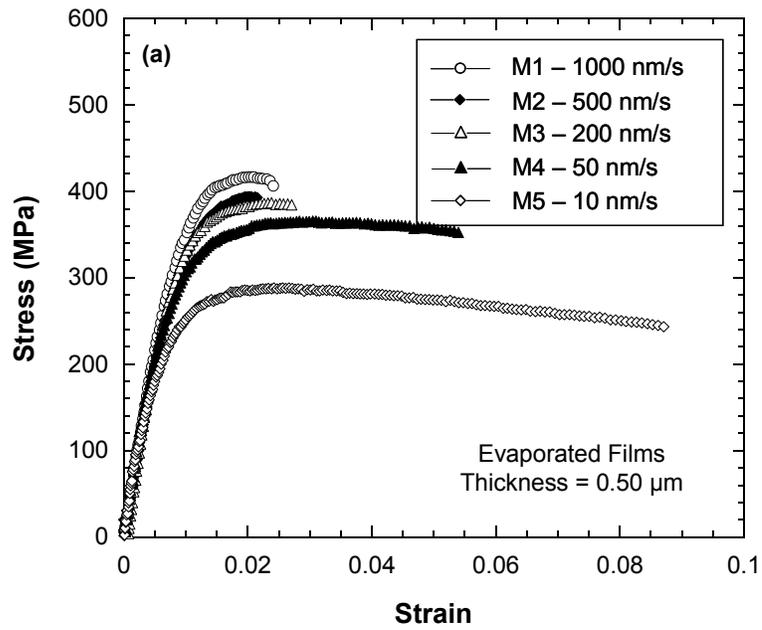
Figure 5-10 Stress-strain curves for the 0.50 µm thick (a) evaporated films and (b) sputtered films at the five displacement rates applied.
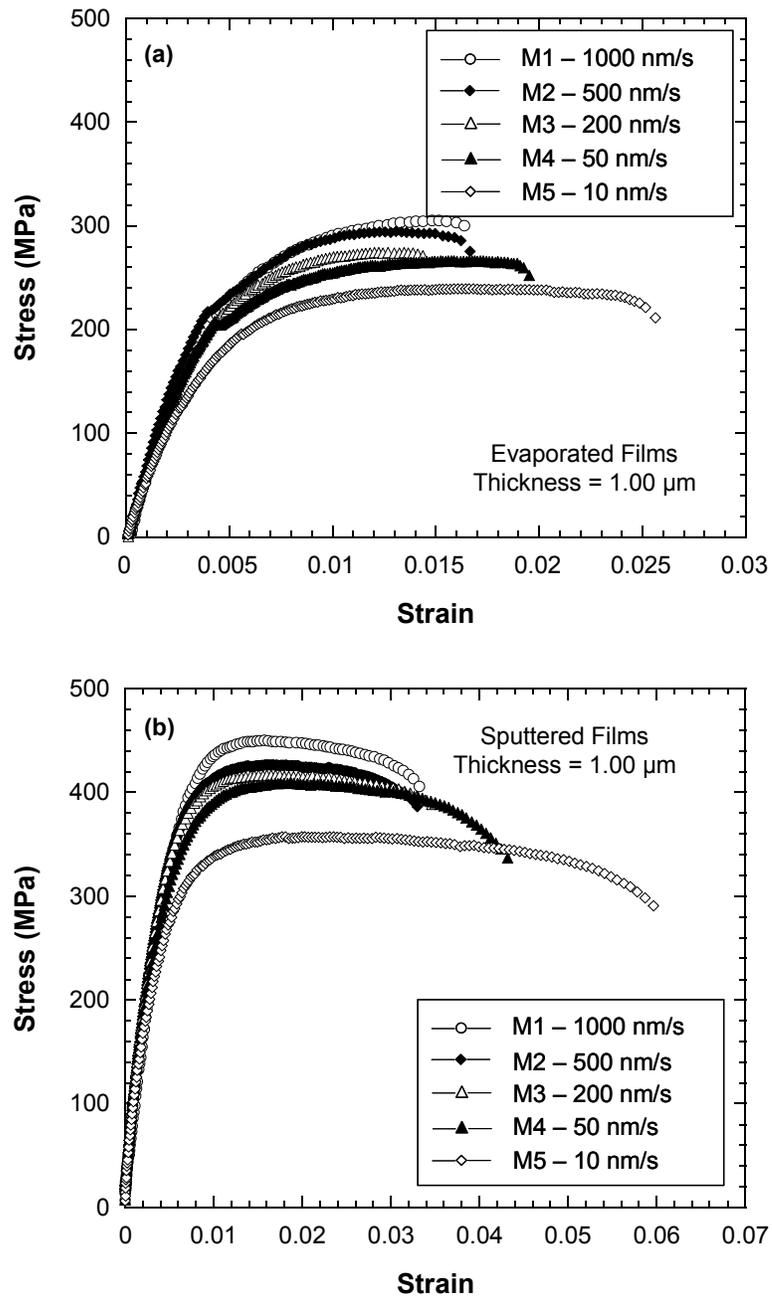
Figure 5-11 Stress-strain curves for the 1.00 µm thick (a) evaporated films and (b) sputtered films at the five displacement rates applied.

Table 5.1: Properties of EBeam evaporated gold films of different thickness subjected to various applied displacement rates.

Film Thickness (μm)	Grain Size (nm)	Displacement rate (nm/s)	Strain rate (1/s)	Young's Modulus (GPa)	Yield Strength (MPa)	Ultimate Strain
E0.25	40	1000	2×10^{-4}	58 ± 0	390 ± 14	0.024 ± 0.005
		500	1×10^{-4}	59 ± 2	358 ± 11	0.028 ± 0.002
		200	5×10^{-5}	58 ± 2	308 ± 4	0.031 ± 0.002
		50	2×10^{-5}	59 ± 0	275 ± 7	0.042 ± 0.005
		10	2×10^{-6}	54 ± 3	230 ± 14	0.060 ± 0.006
E0.50	50	1000	5×10^{-4}	52 ± 0	355 ± 7	0.023 ± 0.002
		500	2×10^{-4}	51 ± 1	330 ± 7	0.024 ± 0.002
		200	4×10^{-5}	52 ± 1	313 ± 7	0.029 ± 0.001
		50	1×10^{-5}	52 ± 1	275 ± 7	0.057 ± 0.004
		10	5×10^{-6}	53 ± 1	223 ± 15	0.079 ± 0.008
E1.00	100	1000	4×10^{-4}	65 ± 1	277 ± 25	0.014 ± 0.003
		500	2×10^{-4}	62 ± 2	250 ± 10	0.015 ± 0.003
		200	7×10^{-5}	63 ± 1	235 ± 9	0.015 ± 0.004
		50	2×10^{-5}	63 ± 2	237 ± 15	0.016 ± 0.006
		10	8×10^{-6}	66 ± 3	218 ± 15	0.020 ± 0.007

Table 5.2: Properties of sputtered gold films of different thickness subjected to various applied displacement rates.

Film Thickness (μm)	Grain Size (nm)	Displacement rate (nm/s)	Strain rate (s^{-1})	Young's Modulus (GPa)	Yield Strength (MPa)	Ultimate Strain
S0.25μm	60	1000	$4x10^{-4}$	71 ± 2	530 ± 14	0.085 ± 0.006
		500	$1x10^{-4}$	72 ± 2	515 ± 12	0.090 ± 0.002
		200	$5x10^{-5}$	71 ± 2	490 ± 18	0.092 ± 0.004
		50	$2x10^{-5}$	70 ± 1	420 ± 18	0.128 ± 0.005
		10	$2x10^{-6}$	73 ± 2	362 ± 7	0.147 ± 0.008
S0.50 μm	120	1000	$4x10^{-4}$	69 ± 1	450 ± 11	0.053 ± 0.005
		500	$1x10^{-4}$	73 ± 3	448 ± 5	0.058 ± 0.006
		200	$6x10^{-5}$	69 ± 3	390 ± 7	0.065 ± 0.007
		50	$2x10^{-5}$	71 ± 2	380 ± 18	0.072 ± 0.004
		10	$2x10^{-6}$	69 ± 3	330 ± 11	0.127 ± 0.012
S1.00 μm	220	1000	$4x10^{-4}$	67 ± 3	415 ± 9	0.029 ± 0.004
		500	$2x10^{-4}$	69 ± 2	395 ± 8	0.033 ± 0.002
		200	$7x10^{-5}$	71 ± 1	365 ± 10	0.035 ± 0.003
		50	$2x10^{-5}$	70 ± 2	345 ± 14	0.048 ± 0.006
		10	$4x10^{-6}$	66 ± 2	315 ± 16	0.054 ± 0.006

The influence of displacement rate on mechanical behavior was also observed to vary with film thickness. Figures 5-12, 5-13, 5-14, 5-15 and 5-16 compiles data from Figure 5-9, 5-10 and 5-11 to best illustrate the thickness effect by plotting data from specimens of the same displacement rate but different thickness. Figure 5-12 to Figure 5-16 are the stress-strain curves for the displacement rate of 1000, 500, 200, 50, and 10 nm/s respectively, showing the mechanical response for films of different thickness, i.e. 0.25, 0.50, and 1.00 µm for both the evaporated films and sputtered films.

For evaporated films, the thinner ones including 0.25 µm and 0.50 µm films show nearly identical behavior and separate themselves as a group from the thick film (1.00 µm films) distinctively, and one can also observed that the separation between plastic yielding of the thinner films and the 1.00 µm films increased gradually with displacement rate. Moreover, the thinner films exhibited considerably larger ultimate strain values, especially for small displacement rates where strains on the order of 9 % were achieved in the 0.50 µm film. However, for the sputtered samples, the separation between each film thickness was presented in a more uniform fashion and there is no apparent variation with the displacement rate. Great dependence of the yield stress and ductility on the film thickness is clearly shown in the sputtered films at all the displacement rates. Thinner films exhibited larger ultimate strain value and higher yield stress.

Further discussion on the size effect and strain rate effect issues is given in the following chapter.
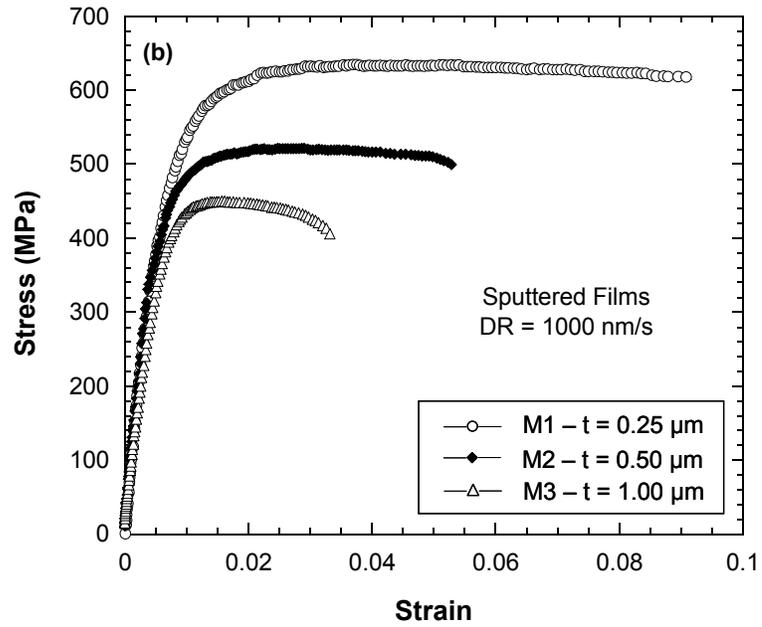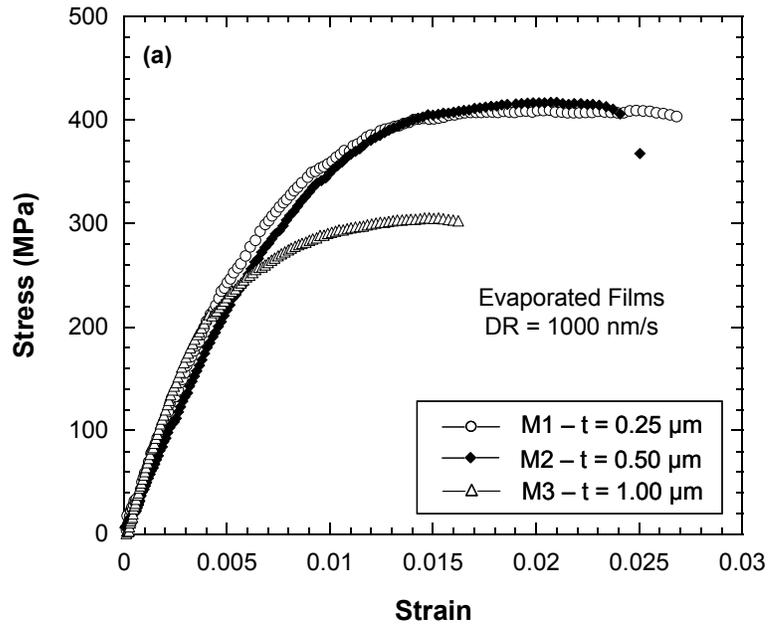
Figure 5-12 Stress-strain curves for the (a) evaporated films and (b) sputtered films with 3 thicknesses at a displacement rate of 1000 nm/s applied.
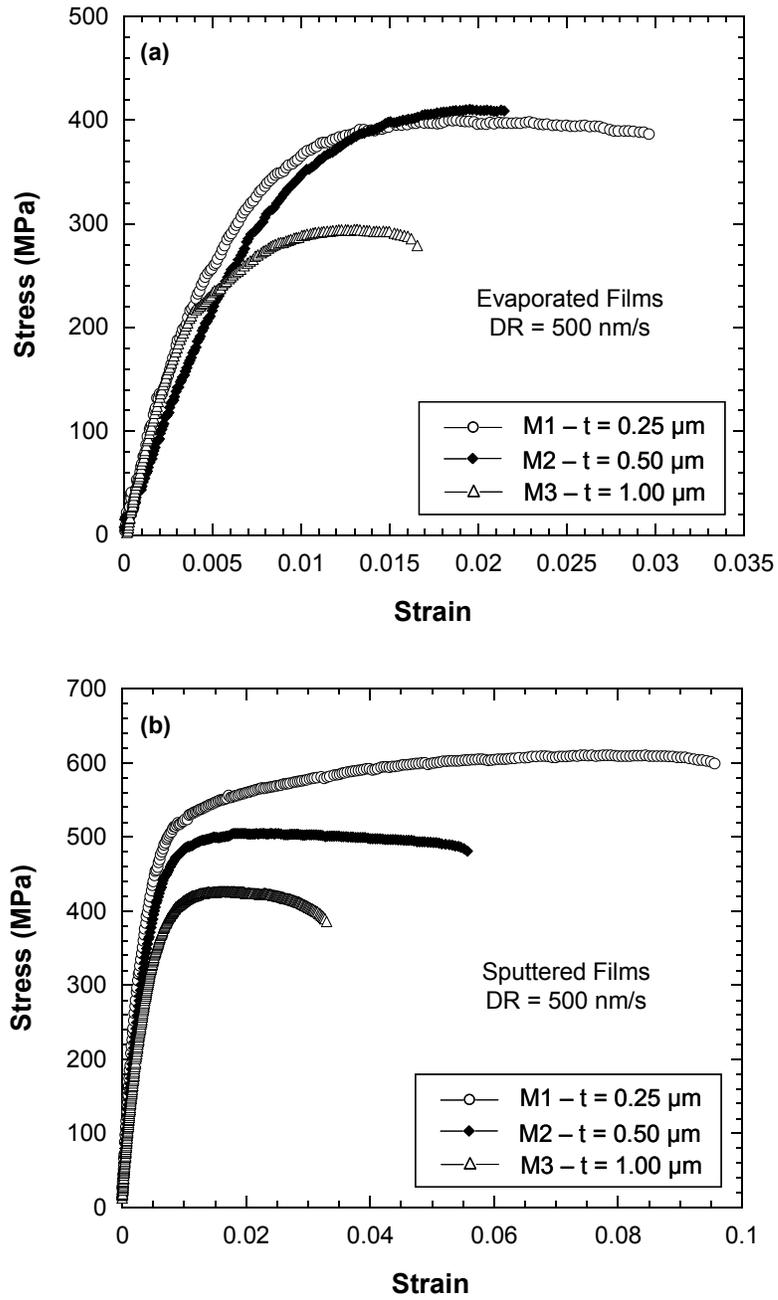
Figure 5-13 Stress-strain curves for the (a) evaporated films and (b) sputtered films with 3 thicknesses at a displacement rate of 500 nm/s applied.
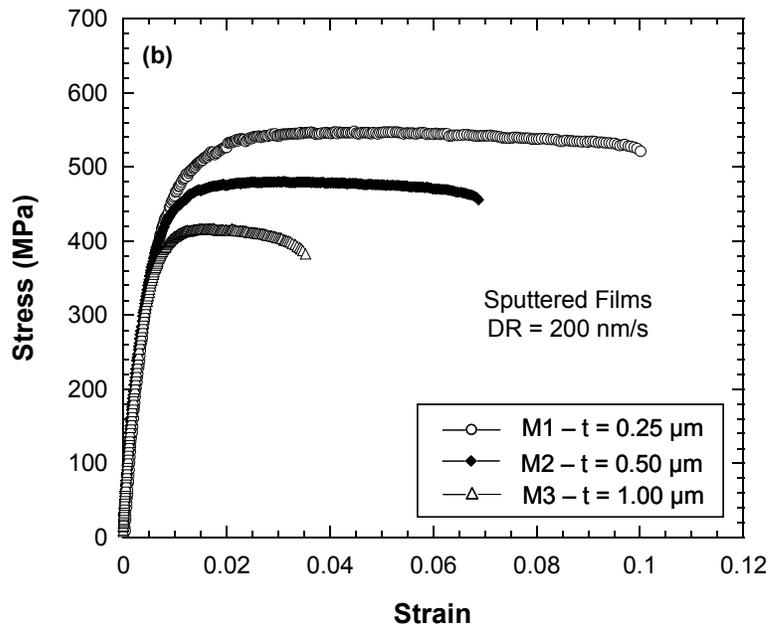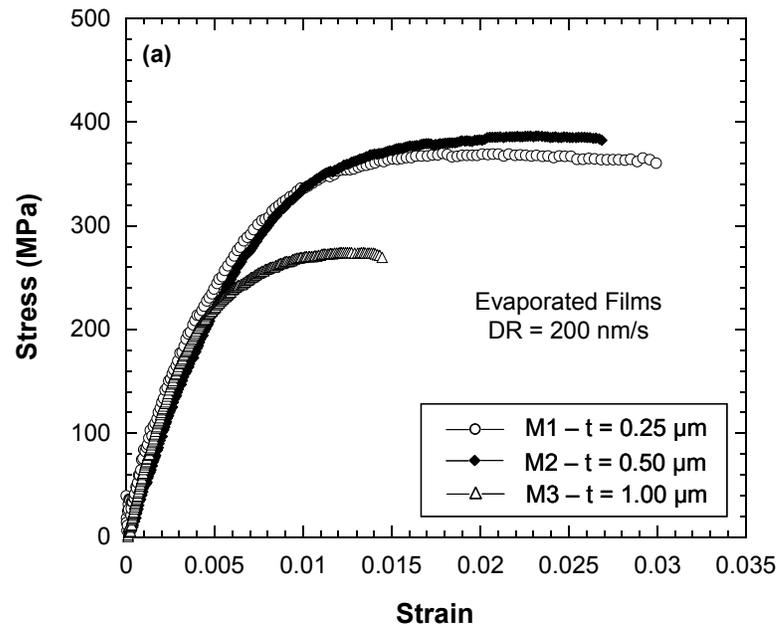
Figure 5-14 Stress-strain curves for the (a) evaporated films and (b) sputtered films with 3 thicknesses at a displacement rate of 200 nm/s applied.
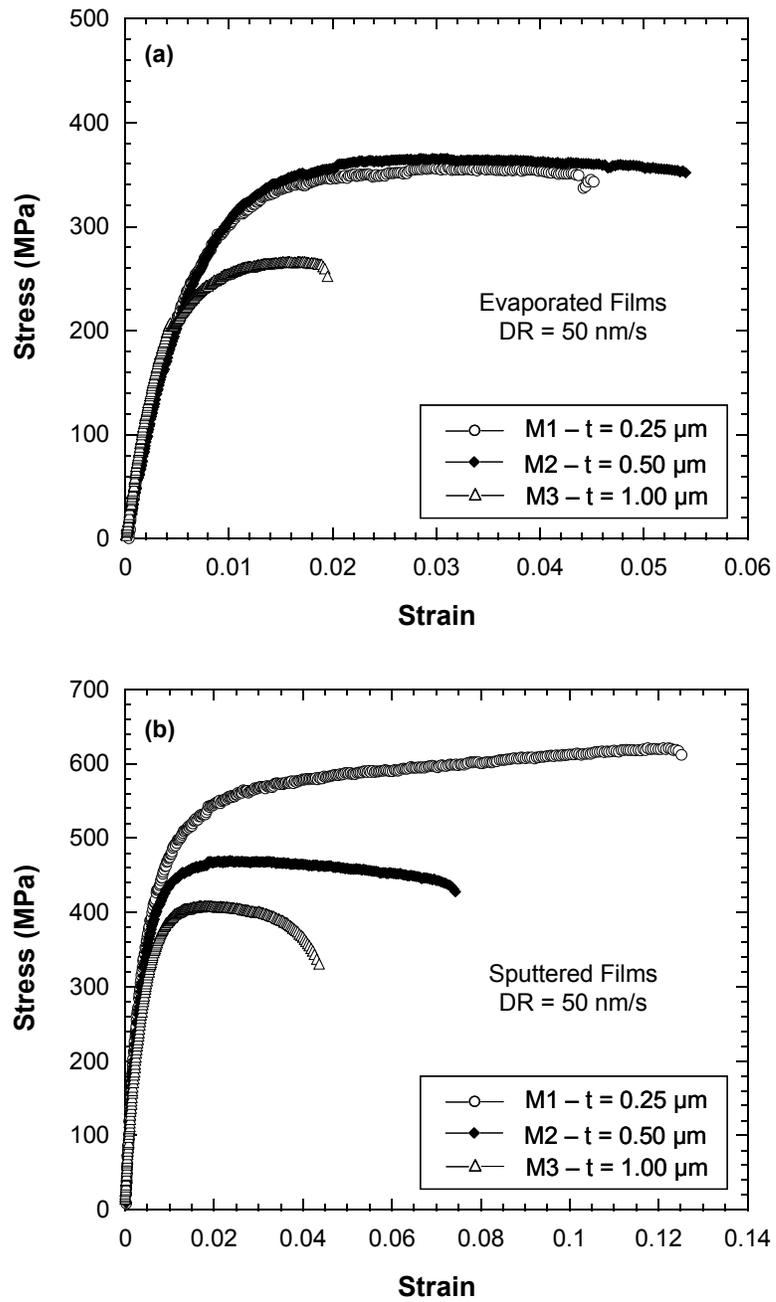
Figure 5-15 Stress-strain curves for the (a) evaporated films and (b) sputtered films with 3 thicknesses at a displacement rate of 50 nm/s applied.
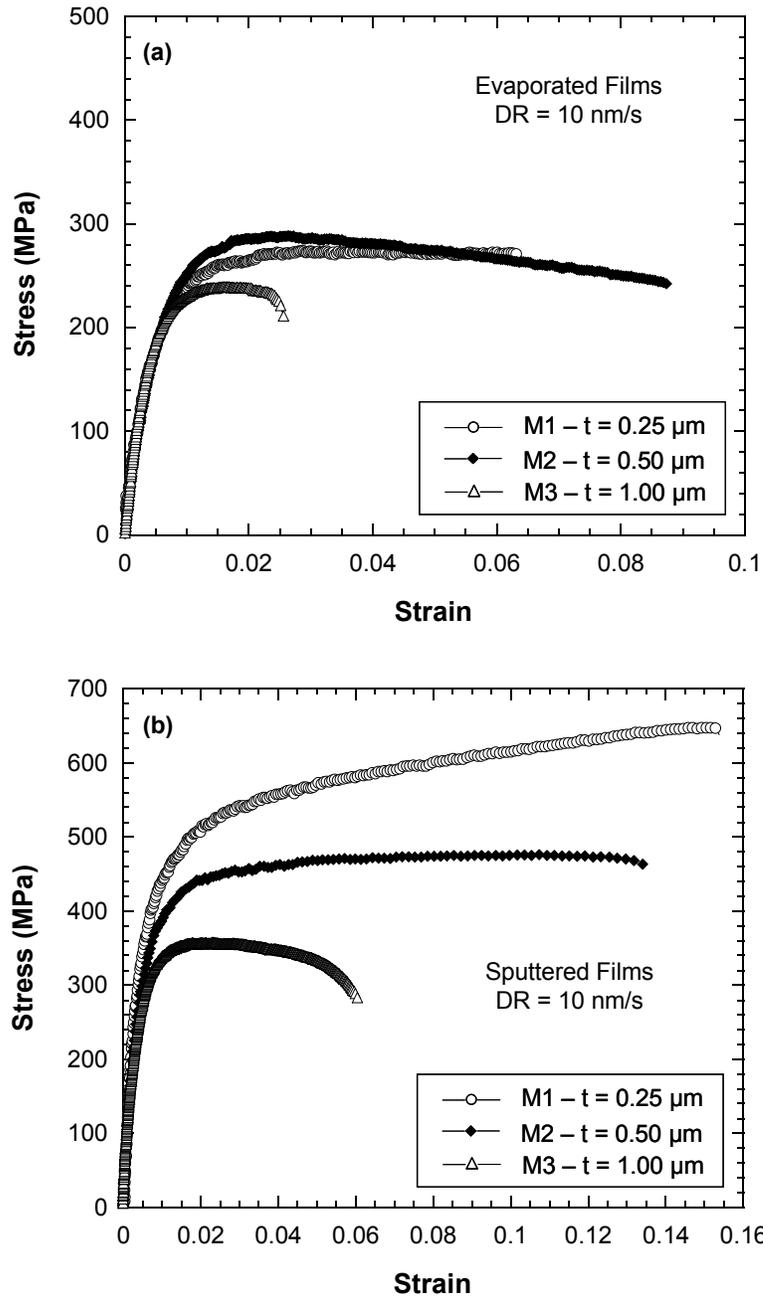
Figure 5-16 Stress-strain curves for the (a) evaporated films and (b) sputtered films with 3 thicknesses at a displacement rate of 10 nm/s applied.

146

CHAPTER 6

DISCUSSIONS

6.1 Elastic Behavior

6.1.1 Microstructure Effect on Young's Modulus

From the observation of the resulted stress-strain curves presented in the previous chapter, the Young's modulus was not found to be influenced greatly by any size effects. This is completely true for sputtered films while the evaporated films shows a slightly disagreement by exhibiting a vague dependence on the film thickness. Figure 6-1 plots the Young's modulus versus the film thickness for both evaporated and sputtered films. The specimens used to compared here had the same dimensions of membrane half-length of 300 μm (± 3 μm), width of 10μm (± 0.05 μm), and variable thickness (0.25 μm, 0.50 μm and 1.00 μm).

The modulus was measured in the range of 68-72 GPa for the sputtered films with thickness changing from 0.25 μm to 1.00 μm; and the Young's modulus of the evaporated gold films was evaluated to range from 52 to 66 GPa for all the tested films. More specifically, 52 to 59 GPa for the 0.25 μm thick films; 51 to 55 GPa for the 0.50 μm thick films and 58 to 66 GPa for the 1.00 μm thick, which are all comparable to values reported by other researchers for evaporated gold thin films [1-7]. The apparent slight variation with film thickness is likely coupled to the film texture dependence on thickness. As the films were grown thicker, interfacial forces appear to have evolved in

favor of the (111) texture transforming to a (100) texture. From the EBSD texture analysis shown in Chapter 4, the 0.50 μm thick film differed from the other thicknesses films with less preferred texture. In contrast, even though the texture transited from a fair (111) direction to a more (100) favored direction while the film thickness increased from 0.25 μm to 1.00 μm, both of the films owned an identifiable (111) component that may have dominated behavior. This evolution in orientation appears to somewhat influence elastic behavior given the relatively small variation in measured values for each film thickness. It is interesting to note that for the sputtered films, as the texture evolved with film thickness the Young's modulus remained relatively constant. That is probably because although the texture is in the evolvement process, they both possessed an identifiable (111) component while the initial textures appeared mixed, which may have dominated the elastic behavior.
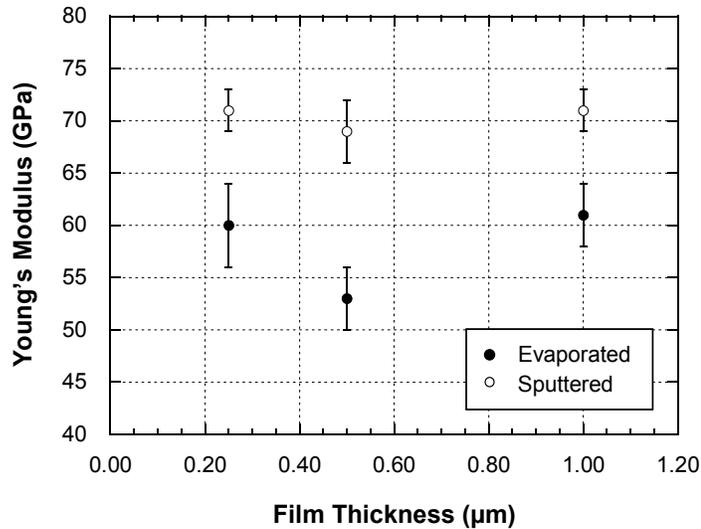
Figure 6-1 Comparison of measured Young's modulus of evaporated and sputtered films with various film thickness.

Moreover, as clearly shown in Figure 6-1, there is a difference between the two kind of films with sputtered films possessing a modulus approximately 10 GPa larger

than the E-Beam evaporated films, regardless of thickness. As discussed before, a relatively stronger (111) crystallographic texture was observed for the sputtered films while the evaporated films exhibited a more mixed orientation with (001) showing a stronger intensity. The sputtered films were subjected to increased thermal and kinetic energy during deposition, which imparted additional energy to the atoms to arrange in more favorable positions. In contrast, the E-Beam deposited films possessed lower grain sizes and a less clear texture. The extra energy imparted to the atoms in the sputtered films is analogous to a low-temperature anneal and thus resulting in a larger grain size and a clear texture development. This further confirmed that the texture difference is more probably contributed to the difference in the values of Young's modulus since gold possesses a high degree of anisotropy in elasticity [8].

It is also worth mentioning that by examining the cross-section microstructure of both evaporated and sputtered films, there is a noticeable amount of twins presented in the evaporated films while much less in sputtered films. The stress-strain response of materials may include contributions from elastic, twinning and plastic deformation. It is difficult to distinguish between the different contributions. Therefore, it was suggested that twinning strains deformed at low stresses may result in a lower elastic modulus [9-11]. Furthermore, recent studies have shown some preliminary experimental evidence in this regard [12, 13]. To this end, the texture difference and twinning presented in evaporated films are likely the causes for the lower modulus for evaporated films.

6.1.2 Discussion on the Low Value of Young's Modulus

Although the measured modulus is in good agreement with values measured on continuum level polycrystalline gold, the low values for the evaporated films is likely due

149

to the lack of a well developed grain structure; whereby, grains are likely to be more disordered and poorly connected. Furthermore, the 0.50 μm thick films exhibited the lowest Young's modulus relative to the 0.25 μm and 1.00 μm thick films, and the rational cause of this might originated from the dissimilarity presented in their microstructure in terms of grain size and grain orientation. The aspect from the grain orientation has been considered in the former section. From the earlier microstructure characterization, both the thinner evaporated films were characterized to possess much smaller grains in the size regime of around 50 nm, where lower modulus were expected for many nanocrystalline metallic films [5, 14, 15]. Several mechanisms have been proposed since then, out of all the mechanisms, two of them are believed more suitable to explain the relatively smaller values found in our study. One was claimed to be their feasibility of anelastic relaxation for the nanocrystalline materials at low temperature, also referred as grain boundary sliding [14, 15]. The other explanation was based on the assumption that the grain boundary region might be elastically softer than grain interior advocated by Haque and Saif [5]. It is noticeable that both the 0.25 μm and 0.50 μm thick films shared the similar grain size, but the Young's modulus decreased slightly more for the 0.50 μm thick films than it does to the 0.25 μm films, which is more likely a consequence of the higher portion of grain boundary volume in the 0.50 μm thick films than in the 0.25 μm thick films.

Future TEM and annealing work will help to further clarify the microstructure effect on measured Young's modulus. All in all, it is clear that the varying mechanisms of the two deposition procedures greatly impact the grain crystallinity, structure and preferred texture [16], therefore, the elasticity of thin film materials.

6.2 Plastic Behavior

6.2.1 Sample Geometry Size Effect on Plasticity

From the observation of the mechanical behavior presented by the stress-strain curves for size effect study, a noticeable dependence of yield strength on both the membrane width and the film thickness was observed for both EBeam evaporated and sputtered films. Figure 6-2 and 6-3 plot the data of 0.50 μm thick films with various widths, 5, 7.5, 10 and 15 μm and 10 μm width films with various thicknesses, 0.25, 0.50 and 1.00 μm respectively to represent this general trend for all the other thickness and width effect, where yield strength decreases as thickness and width increases. An explanation of this behavior may come from considering that the number of grains across the width is more or less halved each time the dimension is decreased resulting in increased geometrical constraints on deformation processes as well as statistical effects due to the small number of grains across the width.

As we can also observed from these two figures, the sputtered films possessed larger yield strength for all the specimens, nearly 100 MPa more in some cases. This is likely related to the fore mentioned fact that sputtering imparts more thermal and kinetic energy to their atoms during deposition, whereby grain structures are better developed.

However, other possibility responsible for these variations may stems from the knowledge that yield stress of polycrystalline thin films can separately dependant on grain size, film thickness, and crystallographic texture. Since the grain size and film texture are all varied with the film thickness, the thickness effect is hard to extract and concluded at this point.

151
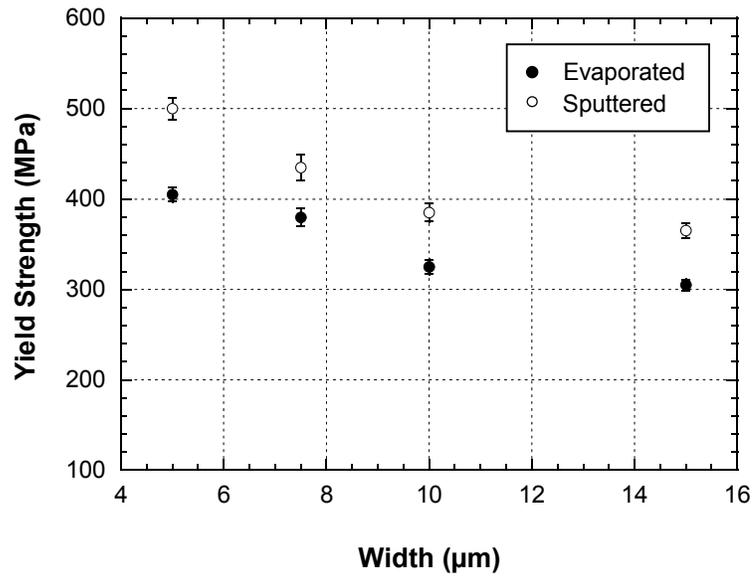
Figure 6-2 Comparison of measured yield strength of evaporated and sputtered films with various membrane widths.
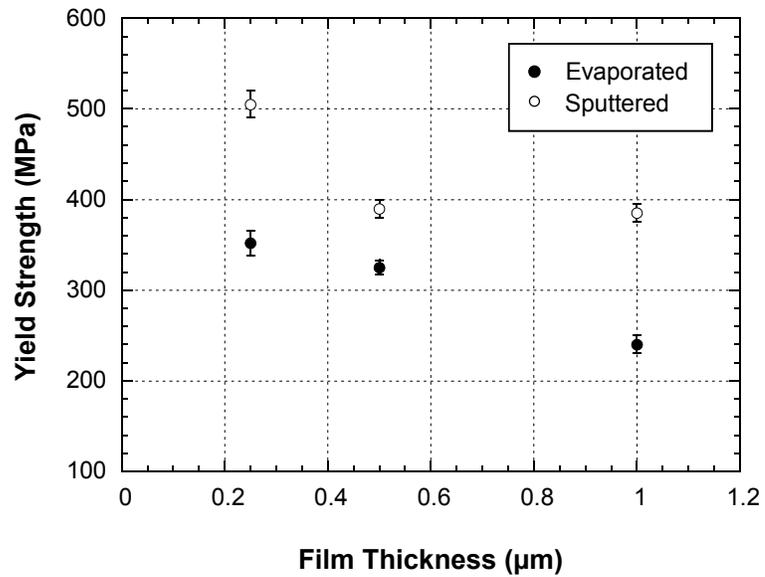
Figure 6-3 Comparison of measured yield strength of evaporated and sputtered films with various film thicknesses.

152

6.2.2 Grain Size Effect on Yield Strength (Hall-Petch Relation)

Since the grain size was varied with the film thickness as observed in microstructure characterization section, the dependence of yield strength on film thickness might be the result of Hall-Petch hardening [17-19]. The Hall-Petch relationship was expressed by the following equation:

$$\sigma_y = \sigma_0 + K_{H-P}d^{-1/2}$$ (6-1)

where σ_0 is the intrinsic stress caused by lattice friction, K_{H-P} is the Hall-Petch constant and σ_y and d are the yield strength and grain size respectively. By plotting the yield strength versus one over the square root of grain size, it was found that in both cases the yield strength increased with decreasing grain size in accordance with the Hall-Petch relation to some extent, which exhibits a linear relationship. The plot and values of σ_0 and K_{H-P} will be given in the following section as a part of the strain rate study.

6.2.3 Film Texture Effect on Yield Strength

It is known that the yield stress of polycrystalline metallic thin films strongly depends on their crystallographic texture [1, 20, 21]. In our study, the texture of the film varied with the film thicknesses, which also results in different grain size, therefore, it is difficult to separate the contribution from one another. However, some suggestive findings regarding with the texture effect can still be addressed with caution. By examining Figure 6-3, the dependence of the yield stress on the film thickness (grain size) for both evaporated and sputtered films agreed fairly well with the Hall-Petch strengthening relationship. However, the grain sizes for the sputtered films are generally larger than the evaporated films, yet the sputtered film possessed higher yield strength in all thicknesses. Plausible explanation to this may relate to the texture effect since the

153

main distinction between the films deposited by two different processes is the grain orientation and texture intensity.

As discussed earlier, the evaporated films experienced an evolvement from a favoring (111) texture to a (100) texture as the films were grown thicker while the sputtered films appear to form a gradually stronger (111) texture with the increased film thickness. All in all, because of the higher thermal and kinetic energy involved during sputtering deposition process compared to the evaporation. A clear texture development is believed to achieve for sputtered films while a more mixed orientation with less intensity for evaporated films.

6.3 Strain Rate Dependent Behavior

The stress-strain curves of all displacement rates applied; 10, 50, 200, 500 and 1000 nm/s for films of all thicknesses deposited by two different processes are shown in Chapter 5. For each film thickness and deposition method, the stress-strain curves exhibited notable differences in response to the variety of displacement rates applied. In general, plastic properties were found to be very sensitive to displacement rate while elastic properties remained relatively unchanged.

6.3.1 Strain Rate Effect on Elasticity

The elastic response of the films did not appear to be influenced by the applied displacement rate as Young's modulus remained relatively constant for each thickness as the displacement rate was varied. When considering the membrane deflection experiment, it is important to note that the relationship between the applied vertical displacement rate and the in-plane strain rate is parabolic in nature. A constant vertical

displacement rate then results in a variable in-plane strain rate that increases with vertical deflection. The applied in-plane strain rate in the linearly elastic region of the curves of each thickness varied from approximately 1×10^{-6} to 5×10^{-4} s^{-1} for vertical displacement rates of 10 through 1000 nm/s respectively. However, within each displacement rate the strain rate varied by only a factor of two in the elastic region. In other words for a displacement rate of 10 nm/s the strain rate varied from approximately 1×10^{-6} to 2×10^{-6} up through a displacement rate of 1000 nm/s varying from 2.5×10^{-4} to 5×10^{-4}. In all cases, the modulus did not vary more than a few percent within each film thickness and did not exhibit any sensitivity to strain rate. Other researchers however have observed the Young's modulus of thin gold films to be significantly influenced by strain rate, namely Emery and Povirk [3, 22] and Chasiotis et al. [7]. In both of these studies uniaxial tension was applied and the strain rate was held constant during the entire test. In comparison, the strain rates in the linear elastic region achieved by the MDE test are in the same range as those applied by the two references. The major difference between the tests was that the grain size in this work was somewhat smaller, 40 nm to 100 nm for evaporated films and 60 nm to 220 nm for sputtered films compare to the 200 nm to 500 nm in Emery's study and 100 nm to 200 nm in Chasiotis's study. Another variation was that the specimen width in this work was considerably smaller, 10 µm versus 200 to 1000 µm. The source of this discrepancy is unclear at this time.

6.3.2 Strain Rate Effect on Plasticity

The plastic properties of the films were significantly influenced by the applied displacement rate as shown in the result section.

The yield strength of all films was observed to increase as displacement increase. In this regard, both evaporated films and sputtered films exhibited similar trends, the thinner evaporated films exhibited the largest variability in the dependence of yield strength to the displacement rate. The larger displacement rates, which of course produce larger in-plane strain rates, clearly have a significant influence on the film's dislocation-glide based plastic flow mechanisms that is attributed to the less time available for these processes to occur.

The influence of displacement rate on yield strength was also observed to vary with film thickness. As illustrated in Figure 5-12 to 5-16 by plotting data from specimens of the same displacement rate but different thickness, one can clearly see that the separation between plastic yielding of the thinner films and the 1.00 μm film increased with displacement rate for evaporated films. Moreover, the thinner films exhibited considerably larger ultimate strain values, especially for small displacement rates. Given that the thinner films are more nanocrystalline, the increased grain boundary volume normally attributed to this grain size regime [23] may force a change in the dominant plastic flow mechanism [24-26], which is intensified in the lower strain rate regime and likely related to the influence of diffusion controlled plastic flow mechanisms. Furthermore it is clear that the 0.50 μm film exhibits more ductility than the 0.25 μm film at the lower displacement rates. Considering that the film thickness is doubled between the 0.25 and 0.50 μm films and yet the average grain size only increased from 40 to 50 nm, one can state that the 0.50 μm film possesses a larger portion of grain boundary volume. The morphology of the thicker film would then enhance the influence of diffusion controlled plastic flow mechanisms and result in enhanced ductility. Further

156

discussion on this matter is given in the following *Possible Creep Mechanism* section as to why the 1.00 μm film does not exhibit enhanced ductility even though it possesses a comparable ratio of grain boundary volume to film volume as the 0.50 μm film. The sputtered films, on the other hand, exhibited distinctly different behavior regarding this issue. As stated earlier, the separation between each film thickness was presented in a more uniform fashion and there is no apparent variation with the displacement rate. This is believed to be attributed to the grain size difference between evaporated and sputtered films. The sputtered films possessed larger grain size than evaporated films, furthermore, instead of sharing similar grain size (40 to 50 nm) for the thinner evaporated films, the grain size of the sputtered films changed with film thickness in a more proportional fashion, i.e. 60 nm for 0.25 μm, 120 nm for 0.50 μm and 220 nm for 1.00 μm thick.

Another matter to consider is that since grain size varied as a function of film thickness, the films may have also experienced Hall-Petch hardening. Figure 6-4 (a) and Figure 6-4 (b) are the Hall-Petch plots illustrating the yield strength vs. $d^{-1/2}$ relationship for the 5 applied displacement rates. The slope of each curve, or the so-called Hall-Petch constant k_{H-P}, was obtained by liner regression fitting and listed along with the average strain rate at each displacement rate in Table 6.1 and 6.2. In examining the slope of each curve, or the so-called Hall-Petch constant K_{H-P}, one can see a gradual decrease as displacement/strain rate decreased. Physically, the Hall-Petch constant quantifies the strength of the microstructural barriers in resisting plastic flow. In this case, the strength of the microstructural barriers is not changing with strain rate. The actual change in slope reflects the influence of diffusion-based mechanisms, which become more prominent and dominate the onset of plastic flow as rate decreases.
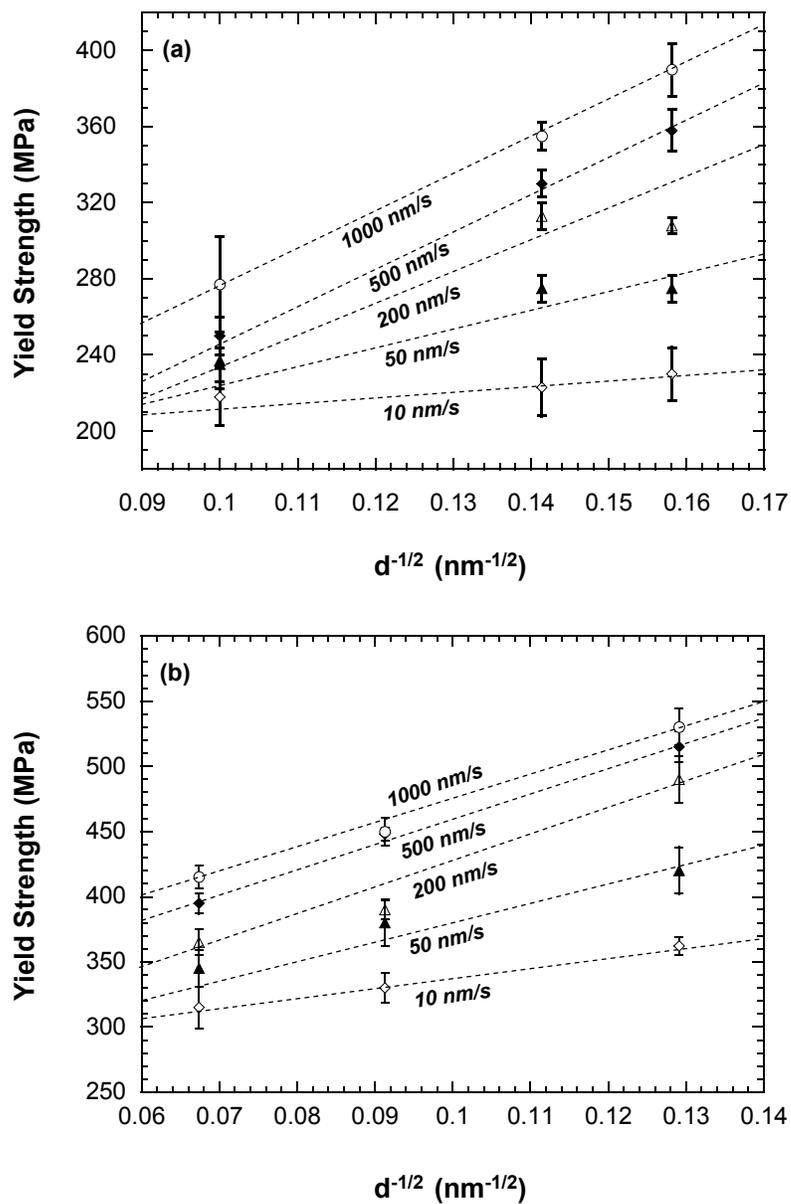
Figure 6-4 A Hall-Petch plot illustrating the relationship of grain boundary hardening on plastic flow of (a) evaporated nanocrystalline gold films and (b) sputtered gold films as a function of the various applied displacement/strain rates, the displacement rate is listed under each curve.

Table 6.1: Hall-Petch Constants of EBeam evaporated gold films subjected to various applied displacement rates.

Displacement Rate Hall-Petch Parameters	1000 nm/s	500 nm/s	200 nm/s	50 nm/s	10 nm/s
$\dot{E}(s^{-1})$ Ave. strain rate	3.0×10^{-4}	1.5×10^{-4}	5.5×10^{-5}	1.5×10^{-5}	5.0×10^{-6}
$K_{H\text{-}P}$ (MPa nm$^{1/2}$)	1932.8	1872.3	1375.7	704.1	190.1
R^2	0.9994	0.9991	0.8888	0.9222	0.8908

Table 6.2: Hall-Petch Constants of sputtered gold films subjected to various applied displacement rates.

Displacement Rate Hall-Petch Parameters	1000 nm/s	500 nm/s	200 nm/s	50 nm/s	10 nm/s
$\dot{E}(s^{-1})$ Ave. strain rate	4.0×10^{-4}	1.3×10^{-4}	6.0×10^{-5}	2.0×10^{-5}	3.0×10^{-6}
$K_{H\text{-}P}$ (MPa nm$^{1/2}$)	1887.3	1929.8	2082.8	1201.6	769.6
R^2	0.9915	0.9961	0.9591	0.9917	0.9942

One can generate a plot of the Hall-Petch slope versus strain rate, which enables a direct observation of the degree to which the contribution of dislocation-based processed to plastic flow is diminished in favor of diffusion-based processes as strain rate decreases, see Figure 6-5 (a) and 6-5 (b). A clear trend is seen whereby at small displacement rates there is little contribution from the dislocations, while at larger rates their affect increases and appears to saturate at a value of approximately 2×10^3 MPa·nm$^{1/2}$ near a strain rate of approximately 1.5×10^{-4} s^{-1} (displacement rate of 500 nm/s). This suggests that at room

temperature, dislocation-based processes dominate plastic flow in gold thin films when displacement rate is on the order of this value or greater. In contrast, below $1.5 \times 10^{-4} \text{ s}^{-1}$, diffusion controlled deformation mechanisms activate and begin to influence plastic flow in an increasing manner as displacement rate decreases. These results may, in part, shed some light on the wide variability of yield strengths and Hall-Petch relationships of nanocrystalline gold reported by many researchers [3, 7, 14, 27-29]. It may also be applicable to aid in the characterization of many other nanocrystalline metals and thin film materials.
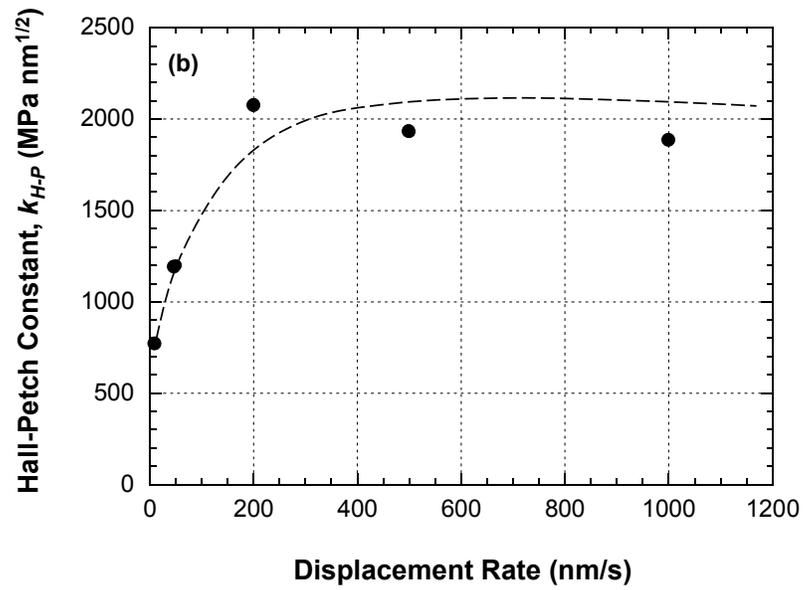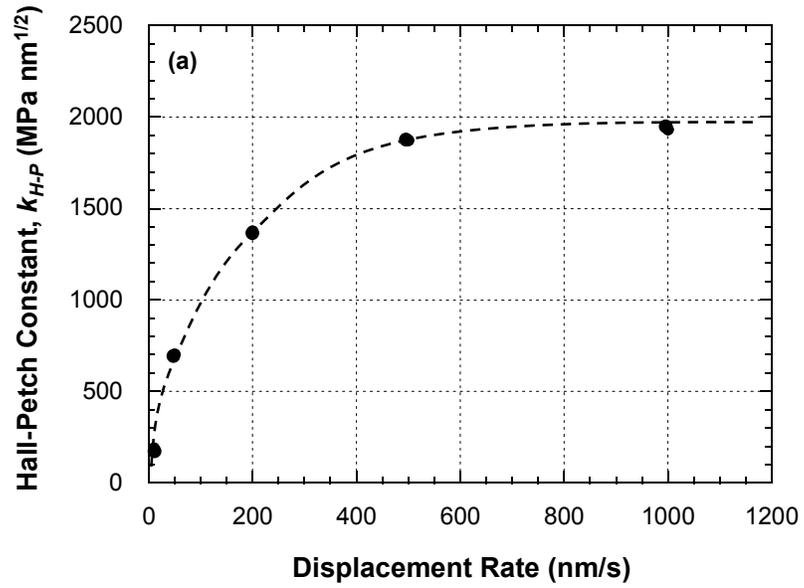
Figure 6-5 A plot of the Hall-Petch slope versus strain rate for (a) evaporated films and (b) sputtered films illustrating the competition between dislocation-based and grain boundary diffusion deformation mechanisms.

In light of the dominance of dislocation-based and diffusion based processes at either end of the applied strain rate range, one can reinterpret the Hall-Petch plot. Since diffusion-based mechanisms begin to assert an appreciable amount of influence on the overall plastic flow at strain rates of 5.5×10^{-5} s^{-1} and lower, the three lowest strain rates can then be re-interpolated by considering the trends in the data rather than performing linear regression, see Figure 6-6. The re-assessment indicated possible evidence that inverse Hall-Petch behavior may be occurring at the lower strain rates in a grain size range of 40 to 50 nm. Furthermore, it also suggests that the critical grain size for this phenomenon may increase as strain rate decreases in view of the fact that there will be extra time for diffusion to occur. These observations correlate well with predictions of the Phase Mixture model for nanocrystalline metals proposed by Kim and Estrin [30]. In their model, the authors generated a deformation mechanism map for nanocrystalline copper based upon the competition of dislocation-based processes and grain boundary diffusion processes as a function of grain size and applied strain rate. An important prediction of the model was that the critical grain size for the onset of inverse Hall-Petch behavior was sensitive to the applied strain rate. Figure 6-7 shows the grain size dependence of the flow stress of nanocrystalline copper at various strain rates.
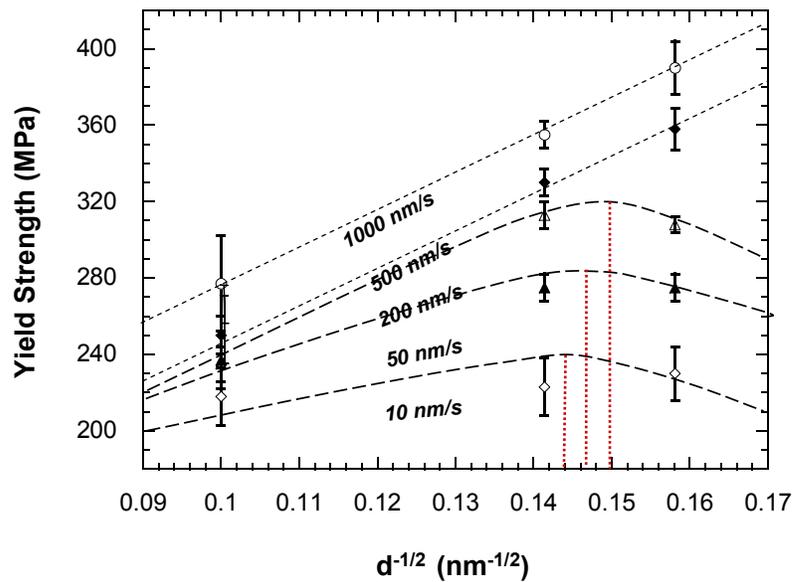
Figure 6-6 A re-examination of the Hall-Petch plot to illustrate the influence that grain boundary diffusion mechanisms have on the onset of plastic flow. Here the curves of the three lower strain rates are re-interpolated. Trends in the data suggest that inverse Hall-Petch behavior may be occurring in the thinner films.
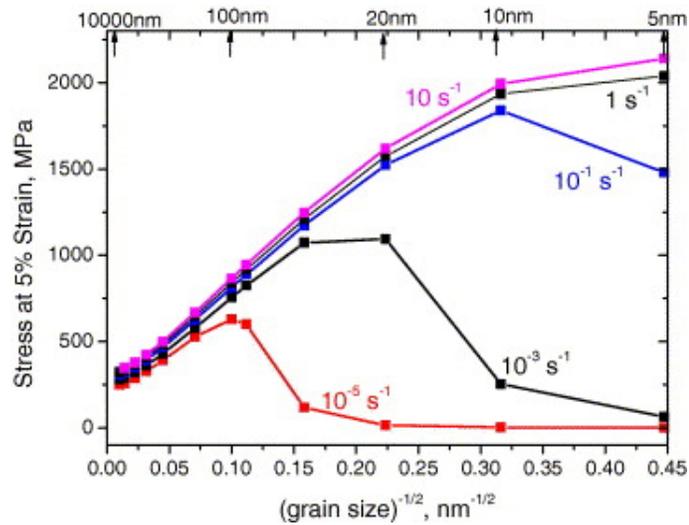

Figure 6-7 Grain size dependence of the flow stress of Cu at various strain rates [30].

6.3.3 Possible Creep Mechanisms

As similar trend is shared by both evaporated and sputtered films, and since the evaporated films exhibited a more distinctive behavior, this section will discussed mainly based on the data summarized from evaporated films.

The diffusion controlled deformation processes that arose at the lower strain rates in the thin film specimens at room temperature were likely creep-based processes that depend on the applied stress level, time scale, temperature, grain size and film thickness [31-34]. In this study, all tests were conducted at room temperature with a stress level of 200 MPa or higher, a film thickness less than 1 μm and a grain size less than 100 nm. In order to determine which creep mechanism was more likely responsible for this strain rate sensitive behavior, creep parameters including stress exponent and creep strain rate were estimated and considered.

In general there are two types of creep mechanisms applicable in these processes, control by dislocation climb and glide motion (power-law creep) [35, 36] and control by the diffusion and sliding along grain boundaries (Coble creep) [37]. Power-law creep is characterized by a universal power-law relationship between stress and strain rate depicting the strain rate-dependence in most polycrystalline materials:

$$\dot{\varepsilon} = A\sigma^n \tag{6-2}$$

where $\dot{\varepsilon}$ is the strain rate, σ is the tensile stress, and A and n are material constants. Constant n is often referred to as the stress exponent and can be given by,

$$n = \left. \frac{\partial \ln \dot{\varepsilon}}{\partial \ln \sigma} \right|_{T,\varepsilon,\dots} \tag{6-3}$$
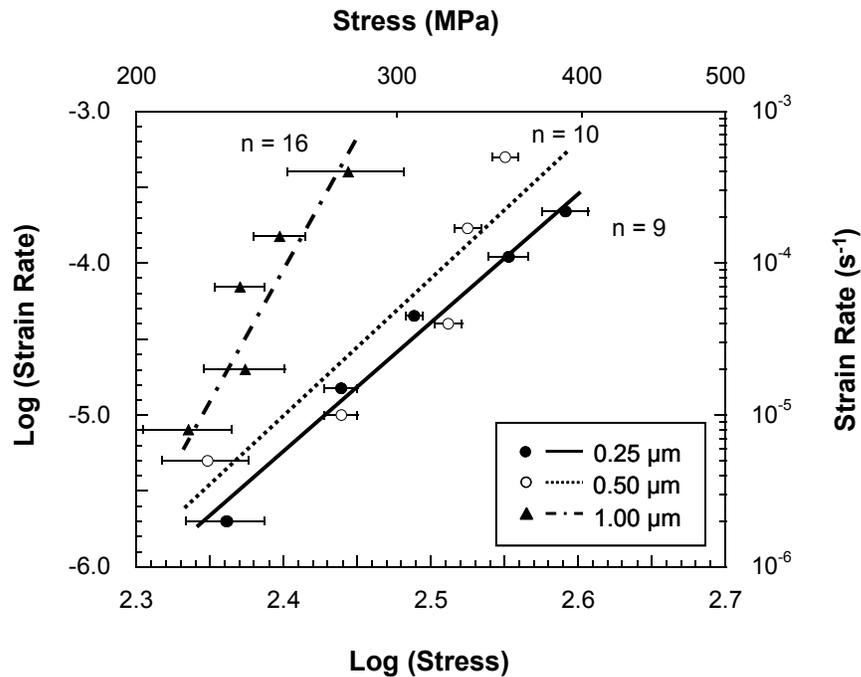
Figure 6-8 A plot of strain rate versus stress for applying power-law analysis. The slope *n* is the stress component used in evaluating plastic flow mechanisms.

Physically, *n* characterizes the sensitivity to deformation rate and is mostly found in the range of 3 to 10 for metals experiencing climb-glide controlled creep [38, 39]. By plotting the strain rate versus stress, one can estimate the magnitude of the stress exponent for each film thickness (grain size), see Figure 6-8. From linear regression in the plot, the stress exponent was found to be 8.7, 9.3 and 15.9 for a film thickness of 0.25, 0.50 and 1.00 μm respectively. These values indicated that the thinner films could have experienced climb-and-glide dislocation creep, which agrees with results found in other experimental studies [3, 7] possessing larger grain size. In climb and glide creep, the diffusion mechanism centers on either lattice diffusion, which operates at high temp and low stress fields, or core diffusion, which operates at low temp and high stress fields [40,

41]. At this point, core diffusion is the more probable power-law mechanism since its characteristics are consistent with the experimental conditions, i.e. room temperature and high stress levels.

However, there are a few issues to contemplate before this conclusion can be considered sound. Since the applied strain rates or stress levels were not held constant, which is a requirement in quantifying creep data, our results are likely more qualitative in nature. As a consequence, the data in Figure 6-8 possesses a noticeable scatter and although the linear regression suggests favorable values for the stress exponent for power-law creep, it is difficult to make any strong conclusions in this regard. Furthermore, our results indicate that creep behavior of the tested films is highly sensitive to grain size. Given that other creep processes, which operate on grain boundary diffusion mechanisms, exhibit a strong dependence on grain size it is prudent to examine attributes associated with this type of deformation.

There are three major themes for creep processes based on grain boundary diffusion: (1) Coble creep, which involves vacancy flow along the grain boundaries [37]; (2) Ashby modified Coble creep, which includes grain boundary sliding [42], and (3) a modified diffusion creep mechanism that accounts for diffusion along triple lines [43], which displays the greatest grain size dependence of the three [44]. Considering that the films tested in this study possess grain sizes of 40 nm or larger and obvious crystalline textures, diffusion along triple line can be discounted since this type of deformation is most pronounced when the grain size is less than 20 nm and no texture exists [43]. Recent experimental observations have found evidence that grain boundary diffusional creep does contribute significantly to deformation in materials stressed at room

166

temperature. Harris and King [45] performed pioneering transmission electron microscopy on freestanding nanocrystalline gold films and found evidence that the diffusion of atoms along grain boundaries and surfaces controlled creep. Yagi et al. [46, 47] reported nanocrystalline gold exhibiting grain boundary sliding and associated grain rotations during deformation at low strain rates in their work on bulk scale specimens. In nanocrystalline copper, Cai and Kong [48] suggested that their observed tensile creep behavior at room temperature can be attributed to interface controlled Coble diffusional creep, similar grain boundary diffusional creep was also observed by others [49-51]. Given that the thinner films in this work possess a grain size on the order of the aforementioned nanocrystalline studies, we expect the similar process would influence plastic flow.

To assess whether the dominant diffusional creep mechanism is centered on grain boundary diffusion we firstly employed the Coble Model [37],

$$\dot{\varepsilon} = \frac{148 D_g \delta \Omega \sigma}{\pi d^3 kT} = \frac{148 D_{g0} \delta \Omega \sigma}{\pi d^3 kT} \exp\left(-\frac{Q_g}{kT}\right) \qquad (6\text{-}4)$$

where $\dot{\varepsilon}$ is the strain rate, σ is the applied stress, D_g is the grain boundary diffusion coefficient, D_{g0} is the diffusivity constant, Q_g is the activation energy, δ is the thickness of grain boundaries, Ω is the atomic volume, d is the grain size, k is Boltzmann's constant, and T is temperature. For the calculation of creep rate as predicted by the Coble model, numerical values of the following parameters were employed: $T = 298$ K, $\Omega = b^3 = 23.89 \times 10^{-30}$ m^3 (b is the Burger's vector of Au, b = 2.88 Å) [52], $D_{g0} = 6.2 \times 10^{-7}$ [53], $Q_g = 85$ kJ/mol [52] and assuming an effective $\delta = 5 \times 10^{-10}$ m [54]. Using these values a creep rate for the 0.25 μm film, with an applied stress of 220 MPa and $d = 4 \times 10^{-8}$ m, was

found to be 3.5×10^{-7} s^{-1}. Similarly, a creep rate of 1.8×10^{-7} s^{-1} was calculated for 0.50 μm film. Both values are comparable in magnitude with the slower applied strain rates employed in this work. A creep rate of 2.3×10^{-8} s^{-1} was calculated for the 1.00 μm film, which was significantly lower than the smallest applied strain rate in this study. This agrees well with the experimental observations, in that, this film did not exhibit appreciable enhancements in ductility at any displacement rate.

Given that the applied strain rates for the thinner films were somewhat higher than the Coble model predicted, the Ashby modified model, which is only a slight modification to the Coble model that includes grain boundary sliding attributes, may provide a better fit to the results. The modified Ashby model [42] is given as,

$$\dot{\varepsilon} = \frac{330 D_{g0} \delta \Omega}{d^3 kT} \left(\sigma - \frac{0.72\Gamma}{d} \right) \exp\left(-\frac{Q_g}{kT} \right) \tag{6-5}$$

where Γ is the grain boundary free energy. Using a value of $\Gamma = 0.2 \ (\pm 0.1)$ J/m^2, reported for nanocrystalline gold by Sakai et al.,[55] the calculated strain rates were found to be 2.3×10^{-6} s^{-1}, 1.2×10^{-6} s^{-1} and 1.5×10^{-7} s^{-1} for 0.25, 0.50 and 1.00 μm thick films respectively. These results are summarized in Table 6.3.

Table 6.3: Calculated values of creep rate for Coble and Ashby modified Coble models as compared to the experimental strain rates.

Film Thickness \ Creep Rate	Coble Model	Ashby Modified	Experimental
0.25 μm	3.5×10^{-7} s^{-1}	2.3×10^{-6} s^{-1}	2.0×10^{-6} s^{-1}
0.50 μm	1.8×10^{-7} s^{-1}	1.2×10^{-6} s^{-1}	5.0×10^{-6} s^{-1}
1.00 μm	2.3×10^{-8} s^{-1}	1.5×10^{-7} s^{-1}	8.0×10^{-6} s^{-1}

The threshold rate calculated for the 0.25 μm film was somewhat larger than the experimental value, while thicker films were significantly smaller. This indicated there was a potential for grain boundary sliding and diffusion mechanisms to occur only in the thinnest film.

For the most part, the rate dependence of the films appeared to indicate power-law creep as a significant contributor to the strain rate sensitivity. An analysis of grain boundary diffusion and sliding mechanisms indicated that localized grain boundary sliding may significantly contribute to deformation in the thinnest film, 0.25 μm, it should be mentioned that this mechanism was observed by electron microscopy in the work of Sakai et al. [14] in the grain size regime of 20 nm. Considering that deformation of the 0.25 μm film closely mirrored that of the 0.50 μm film at all of the applied strain rates, and given that their grain sizes are very similar, this mechanism may play a role in both films. Furthermore, work by Wang and Ma [56, 57] identified dislocation-grain boundary interaction-mediated mechanisms that may also play a role in these nanocrystalline materials. Finally, the film microstructure was columnar, textured and under a state of plane stress during tensile deformation, this situation likely limits grain boundary processes to be two-dimensional in the plane of the film. Nonetheless, the strain rate dependence was strongly correlated with grain size, indicating that these and other mechanisms may be playing a role.

In summary, the strain rate dependence observed in this work was likely a mixture of power-law creep and grain boundary mechanisms. In order to obtain a clearer understanding of the creep mechanisms in gold thin films, more specifically designed

creep experiments are needed that include characterization with transmission electron microscopy.

6.4 References

[1]   W. D. Nix, "Mechanical-Properties of Thin-Films," *Metallurgical Transactions A: Physical Metallurgy and Materials Science*, vol. 20, pp. 2217-2245, 1989.

[2]   B. C. Prorok and H. D. Espinosa, "Effects of nanometer-thick passivation layers on the mechanical response of thin gold films," *Journal of Nanoscience and Nanotechnology*, vol. 2, pp. 427-433, 2002.

[3]   R. D. Emery and G. L. Povirk, "Tensile behavior of free-standing gold films. Part II. Fine-grained films," *Acta Materialia*, vol. 51, pp. 2079-2087, 2003.

[4]   H. D. Espinosa, B. C. Prorok, and M. Fischer, "A methodology for determining mechanical properties of freestanding thin films and MEMS materials," *Journal of the Mechanics and Physics of Solids*, vol. 51, pp. 47-67, 2003.

[5]   M. A. Haque and M. T. A. Saif, "Deformation mechanisms in free-standing nanoscale thin films: A quantitative in situ transmission electron microscope study," *PNAS*, vol. 101, pp. 6335- 6340, 2004.

[6]   C. W. Baek, Y. K. Kim, Y. Ahn, and Y. H. Kim, "Measurement of the mechanical properties of electroplated gold thin films using micromachined beam structures," *Sensors And Actuators A-Physical*, vol. 117, pp. 17, 2005.

[7]   I. Chasiotis, C. Bateson, K. Timpano, A. S. McCarty, N. S. Barker, and J. R. Stanec, "Strain rate effects on the mechanical behavior of nanocrystalline Au films," *Thin Solid Films*, vol. 515, pp. 3183, 2007.

[8]   T. H. Coutrney, *Mechanical Behavior of Materials*. New York: McGraw Hill, 1990.

[9]   C. P. Frick, A. M. Ortega, J. Tyber, K. Gall, and H. J. Maier, "Multiscale structure and properties of cast and deformation processed polycrystalline NiTi shape-memory alloys," *Metallurgical And Materials Transactions A-Physical Metallurgy And Materials Science*, vol. 35A, pp. 2013, 2004.

[10]   Y. Liu and H. Xiang, "Apparent modulus of elasticity of near-equiatomic NiTi," *Journal Of Alloys And Compounds*, vol. 270, pp. 154, 1998.

[11]   K. N. Melton and O. Mercier, "Deformation-Behavior Of Niti-Based Alloys," *Metallurgical Transactions A-Physical Metallurgy And Materials Science*, vol. 9, pp. 1487, 1978.

[12] H. Petrova, J. Perez-Juste, Z. Y. Zhang, J. Zhang, T. Kosel, and G. V. Hartland, "Crystal structure dependence of the elastic constants of gold nanorods," *Journal Of Materials Chemistry*, vol. 16, pp. 3957, 2006.

[13] S. Rajagopalan, A. L. Little, M. A. M. Bourke, and R. Vaidyanathan, "Elastic modulus of shape-memory NiTi from in situ neutron diffraction during macroscopic loading, instrumented indentation, and extensometryl," *Applied Physics Letters*, vol. 86, 2005.

[14] S. Sakai, H. Tanimoto, and H. Mizubayashi, "Mechanical behavior of high-density nanocrystalline gold prepared by gas deposition method," *Acta Materialia*, vol. 47, pp. 211-217, 1998.

[15] A. J. Kalkman, A. H. Verbruggen, and G. C. A. M. Janssen, "Young's modulus measurements and grain boundary sliding in free-standing thin metal films," *Applied Physics Letters*, vol. 78, pp. 2673-2675, 2001.

[16] C. A. Neugebauer, J. B. Newkirk, and D. A. Vermilyea, "Structure and Properties of Thin Films." New York, New York: John Wiley and Sons, 1959.

[17] E. O. Hall, "The Deformation And Ageing Of Mild Steel.3. Discussion Of Results," *Proceedings Of The Physical Society Of London Section B*, vol. 64, pp. 747, 1951.

[18] N. J. Petch, "The Cleavage Strength Of Polycrystals," *Journal Of The Iron And Steel Institute*, vol. 174, pp. 25, 1953.

[19] M. F. Ashby, "Deformation of Plastically Non-Homogeneous Materials," *Philosophical Magazine*, vol. 21, pp. 399-&, 1970.

[20] C. V. Thompson, "The Yield Stress Of Polycrystalline Thin-Films," *Journal Of Materials Research*, vol. 8, pp. 237, 1993.

[21] C. V. Thompson and R. Carel, "Stress and grain growth in thin films," *Journal Of The Mechanics And Physics Of Solids*, vol. 44, pp. 657, 1996.

[22] R. D. Emery and G. L. Povirk, "Tensile behavior of free-standing gold films. Part I. Coarse-grained films," *Acta Materialia*, vol. 51, pp. 2067-2078, 2003.

[23] H. Gleiter, "Nanocrystalline Materials," *Progress In Materials Science*, vol. 33, pp. 223, 1989.

[24] H. VanSwygenhoven and A. Caro, "Plastic behavior of nanophase Ni: A molecular dynamics computer simulation," *Applied Physics Letters*, vol. 71, pp. 1652-1654, 1997.

[25]   J. Schiotz, F. D. Di Tolla, and K. W. Jacobsen, "Softening of nanocrystalline metals at very small grain sizes," *Nature*, vol. 391, pp. 561-563, 1998.

[26]   L. Lu, S. X. Li, and K. Lu, "An abnormal strain rate effect on tensile behavior in nanocrystalline copper," *Scripta Materialia*, vol. 45, pp. 1163-1169, 2001.

[27]   D. T. Read, Y. W. Cheng, R. R. Keller, and J. D. McColskey, "Tensile properties of free-standing aluminum thin films," *Scripta Materialia*, vol. 45, pp. 583, 2001.

[28]   P. A. El-Deiry and R. P. Vinci, "Strain Rate Dependent Behavior of Pure Aluminum and Copper Micro-Wires," *Mater. Res. Soc. Sym. Proc.*, vol. 695, pp. L4.2.1, 2002.

[29]   H. Conrad and K. Jung, "Effect of grain size from mm to nm on the flow stress and plastic deformation kinetics of Au at low homologous temperatures," *Materials Science & Engineering, A: Structural Materials: Properties, Microstructure and Processing*, vol. 406, pp. 78, 2005.

[30]   H. S. Kim and Y. Estrin, "Phase mixture modeling of the strain rate dependent behavior of nanostructured materials," *Acta Mater.*, vol. 53, pp. 765-772, 2005.

[31]   H. Van Swygenhoven and J. R. Weertman, "Deformation in nanocrystalline metals," *Materials Today*, vol. 9, pp. 24-31, 2006.

[32]   F. Wang and K. Xu, "An investigation of nanoindentation creep in polycrystalline Cu thin film," *Materials Letters*, vol. 58, pp. 2345-2349, 2004.

[33]   K. Gall, N. West, K. Spark, M. L. Dunn, and D. S. Finch, "Creep of thin film Au on bimaterial Au/Si microcantilevers," *Acta Materialia*, vol. 52, pp. 2133-2146, 2004.

[34]   F. R. N. Nabarro, "Creep at very low rates," *Metallurgical and Materials Transactions A: Physical Metallurgy and Materials Science*, vol. 33, pp. 213-218, 2002.

[35]   J. Weertman, "Creep of polycrystalline aluminium as determined from strain rate tests," *Journal of the Mechanics and Physics of Solids*, vol. 4, pp. 230, 1956.

[36]   A. M. Brown and M. F. Ashby, "On the power-law creep equation," *Scripta Metallurgica*, vol. 14, pp. 1297, 1980.

[37]   R. L. Coble, "A Model for Boundary Diffusion Controlled Creep in Polycrystalline Materials," *Journal of Applied Physics*, vol. 34, pp. 1679-1682, 1963.

[38] A. K. Mukherjee, J. E. Bird, and J. E. Dorn, "Experimental Correlations for High-temperature creep," *Trans. ASM*, vol. 62, pp. 155, 1969.

[39] R. L. Stocker and M. F. Ashby, "On the empirical constants in the Dorn equation (dislocation creep)," *Scripta Metallurgica*, vol. 7, pp. 115-120, 1973.

[40] J. P. Hirth and J. Lothe, *Theory of Dislocations*. New York: McGraw Hill, 1968.

[41] S. L. Robinson and O. D. Sherby, "Mechanical behavior of polycrystalline tungsten at elevated temperature," *Acta Metallurgica*, vol. 17, pp. 109, 1969.

[42] M. F. Ashby and R. A. Verrall, "Diffusion-Accommodated Flow And Superplasticity," *Acta Metallurgica*, vol. 21, pp. 149, 1973.

[43] G. Palumbo, S. J. Thorpe, and K. T. Aust, "On The Contribution Of Triple Junctions To The Structure And Properties Of Nanocrystalline Materials," *Scripta Metallurgica Et Materialia*, vol. 24, pp. 1347, 1990.

[44] N. Wang, Z. Wang, K. T. Aust, and U. Erb, "Effect of grain size on mechanical properties of nanocrystalline materials," *Acta Metallurgica et Materialia*, vol. 43, pp. 519, 1995.

[45] K. E. Harris and A. H. King, "Direct observation of diffusional creep via TEM in polycrystalline thin films of gold," *Acta Materialia*, vol. 46, pp. 6195-6203, 1998.

[46] N. Yagi, A. Rikukawa, H. Mizubayashi, and H. Tanimoto, "Deformation by grain rotations in nanocrystalline fcc-metals," *Materials Science & Engineering, A: Structural Materials: Properties, Microstructure and Processing*, vol. 442, pp. 323, 2006.

[47] N. Yagi, A. Rikukawa, H. Mizubayashi, and H. Tanimoto, "Experimental tests of the elementary mechanism responsible for creep deformation in nanocrystalline gold," *Physical Review B*, vol. 74, 2006.

[48] B. Cai, Q. P. Kong, L. Lu, and K. Lu, "Interface controlled diffusional creep of nanocrystalline pure copper," *Scripta Materialia*, vol. 41, pp. 755-759, 1999.

[49] D. L. Wang, Q. P. Kong, and J. P. Shui, "Creep Of Nanocrystalline Ni-P Alloy," *Scripta Metallurgica Et Materialia*, vol. 31, pp. 47, 1994.

[50] J. Deng, D. L. Wang, Q. P. Kong, and J. P. Shui, "Stress dependence of creep in nanocrystalline Ni-P alloy," *Scripta Metallurgica et Materialia*, vol. 32, pp. 349, 1995.

[51]   P. G. Sanders, M. Rittner, E. Kiedaisch, J. R. Weertman, H. Kung, and Y. C. Lu, "Creep of nanocrystalline Cu, Pd, and Al-Zr," *Nanostructured Materials*, vol. 9, pp. 433-440, 1997.

[52]   W. F. Gale and T. C. Totemeier, "Smithells Metals Reference Book," 8th ed: Elsevier, 2004.

[53]   H. J. Frost and M. F. Ashby, *Deformation mechanism maps*. New York: Pergamon Press, 1982.

[54]   J. Horvath, R. Birringer, and H. Gleiter, "Diffusion In Nanocrystalline Material," *Solid State Communications*, vol. 62, pp. 319, 1987.

[55]   S. Sakai, H. Tanimoto, E. Kita, and H. Mizubayashi, "Characteristic creep behavior of nanocrystalline metals found for high-density gold," *Physical Review B*, vol. 66, 2002.

[56]   Y. M. Wang and E. Ma, "Strain hardening, strain rate sensitivity, and ductility of nanostructured metals," *Materials Science And Engineering A-Structural Materials Properties Microstructure And Processing*, vol. 375-77, pp. 46, 2004.

[57]   Y. M. Wang and E. Ma, "Temperature and strain rate effects on the strength and ductility of nanostructured copper," *Applied Physics Letters*, vol. 83, pp. 3165, 2003.

CHAPTER 7

CONCLUDING REMARKS AND FUTURE WORKS

7.1 Summary of Results and Conclusions

Thin gold films with varying thickness of 0.25 μm, 0.50 μm and 1.00 μm deposited by both E-Beam evaporation and sputtering techniques were comparatively studied by employing the Membrane Deflection Experiment technique. High-resolution scanning electron microscopy, including electron-backscattered diffraction, was employed to reveal the differences in microstructure generated by two deposition methods in terms of morphology and crystallography. A difference of approximately 10 to 15 GPa in Young's modulus was measured for evaporated and sputtered films and indicated the strong relationship between the deformation mechanics and the microstructure each film possessed. The texture difference and twinning presented in evaporated films are likely the causes for the lower modulus. Moreover, sputtering appeared to yield stronger films due to the extra thermal and kinetic energy imparted to the atoms during deposition.

Strain rate dependence behaviors for gold films were evaluated by the MDE technique with applied strain rates on the order of 10^{-4} s^{-1} to 10^{-6} s^{-1}. The plastic properties were found to be particularly sensitive to strain rate and film thickness while the elastic property remained relatively unchanged. In terms of film thickness, each

thickness possessed a different grain size and corresponding Hall-Petch boundary hardening was observed. The thinner films exhibited significant strain rate sensitivity while the thicker films exhibited only marginal changes. Hall-Petch boundary hardening was observed and dominated plastic flow at larger strain rates while diffusion controlled deformation mechanisms appeared to be activated with increasing influence as strain rate decreased. The strain rate dependency of the thin gold films was attributed to the activation of creep-based mechanisms. Analysis of dislocation-based and grain boundary diffusion related creep suggested that the films were likely experiencing a mixture of power-law creep and grain boundary mechanisms. Furthermore, the data of evaporated nanocrystalline films suggested that the critical grain size for inverse behavior was sensitive to strain rate. These results represent an important experimental confirmation of how nanostructured materials behave at very low strain rates.

7.2 Future Work

The possible future work relevant to this study can be categorized into two parts: improvements on the current techniques and continuing work, as explained below. Improvements on the techniques include both the testing technique and characterization technique. Continuing work is work that should have been done, but was not undertaken due to limitations in time or resources.

7.2.1 Improvement Work

The membrane deflection experiment (MDE) was well-established for microtensile testing and has been shown to be capable of obtaining precise mechanical data for freestanding thin films. However, the applied strain rates or stress levels were not

held constant in our strain rate effect study, which is a requirement in quantifying creep data, thus our results are likely more qualitative in nature. As a consequence, the data used to access the values of the stress exponent possesses a noticeable scatter and although the linear regression suggests favorable values for the stress exponent for power-law creep, it is difficult to make any strong conclusions in this regard. In order to better define and clarify the dominant or combination of creep mechanisms responsible, improvements on a true creep testing scheme based on the MDE technique is required. Specifically, developing a setup in which stress or strain rate could be held constant may allow for a better identification of the creep mechanisms.

Furthermore, with regard to the microstructure characterization, in addition to the high resolution scanning electron microscope and electron-backscattered diffraction used to reveal the differences in microstructure in terms of morphology and crystallography, TEM characterization is highly desired and would be ideal to access internal grain structures, such as dislocation density and twin identification for supporting the thin film mechanics.

7.2.2 Continuing Work

This work has provided and complemented the knowledge base of mechanical behavior of gold thin films, which allowed a more thorough understanding of the mechanical behavior of polycrystalline thin films. In addition, the data presented are obtained by systematically varying important material parameters and by using the easily-interpreted modality of tension. However, in this study, there was more than one material parameter (film thickness, grain size, film texture etc.) varied at the same time, which made distinguishing between the different contributions very difficult. It would be

178

desirable if the studied material parameters can be tailored in a more independent fashion. Annealing work and texture controlled by employing different substrates may help resolve this problem to some extent.

In this work, the data of evaporated nanocrystalline films suggested that the critical grain size for inverse behavior was sensitive to strain rate. These results represent a very important experimental confirmation of how nanostructured materials behave at very low strain rates. However, due to the limited time and resources, only three different film thicknesses/grain sizes have been studied in this regard. The conclusion would be more affirmative and specific if more data from a larger variance of grain size were available.